ISBN 978-82-326-1928-3 (printed ver.)
ISBN 978-82-326-1929-0 (electronic ver.)
ISSN 1503-8181

Arne Ilseng
Doctoral thesis

Doctoral theses at NTNU, 2016:295

Arne Ilseng

Mechanical behaviour of particle-filled elastomers at various temperatures

An experimental and numerical study

NTNU
Norwegian University of
Science and Technology

Doctoral theses at NTNU, 2016:295

NTNU
Norwegian University of
Science and Technology
Thesis for the Degree of
Philosophiae Doctor
Faculty of Engineering Science and Technology
Department of Structural Engineering

NTNU

NTNU
Norwegian University of
Science and Technology

Arne Ilseng

Mechanical behaviour of particle-filled elastomers at various temperatures

An experimental and numerical study

Thesis for the Degree of Philosophiae Doctor

Trondheim, November 2016

Norwegian University of Science and Technology
Faculty of Engineering Science and Technology
Department of Structural Engineering

NTNU
Norwegian University of
Science and Technology

NTNU
Norwegian University of Science and Technology

Thesis for the Degree of Philosophiae Doctor

Faculty of Engineering Science and Technology
Department of Structural Engineering

ISBN 978-82-326-1928-3 (printed ver.)
ISBN 978-82-326-1929-0 (electronic ver.)
ISSN 1503-8181

Doctoral theses at NTNU, 2016:295

Printed by NTNU Grafisk senter

Preface

This thesis is submitted in partial fulfilment of the requirements for the degree *Philosophiae Doctor* (PhD) at the Norwegian University of Science and Technology (NTNU). The doctoral work was carried out at the Structural Impact Laboratory (SIMLab) at the Department of Structural Engineering at NTNU. The work was fully financed by the oil service company Aker Solutions AS, which employed the candidate during the project period.

The supervisors of the work have been Professor Arild Holm Clausen (NTNU) and Professor Bjørn Helge Skallerud (NTNU). The thesis consists of three journal articles, referred to as Paper I to Paper III, and a synopsis defining the background for the work and the connection between the three papers. Two conference papers are included in the appendix. The PhD-study started in August 2013 and was completed for submission in August 2016.

Declaration of the authors' contribution: Ilseng initiated and performed the experiments, did the extraction and interpretation of the experimental data, developed the new constitutive model, produced all figures, coded all Python and Fortran scripts, and wrote the manuscript of the appended papers. The co-authors, Skallerud and Clausen, contributed with supervision of the work, discussion of ideas, and reviewed the appended papers. All experiments were conducted in collaboration with a technician.

The author declares that this thesis is the result of original research that has not previously been submitted for a degree at any university or institution.

Arne Ilseng

Trondheim, August 2016

Abstract

This work consist of an experimental and numerical study of the mechanical behaviour of particle-filled HNBR and FKM elastomers subjected to various loading modes at a range of temperatures. The thesis is organized as a synopsis, providing the motivation, the objectives, the theoretical background, and a summary of the work, while the main body is a collection of three journal articles providing the scientific contribution. In the appendix, two conference papers are included.

Paper I deals with the tension behaviour of three different commercial elastomeric materials, being two HNBR and one FKM compound, at temperatures ranging from −20 to 150 ^{o}C. A cyclic deformation history was applied to quantify viscoelastic and history dependent effects, and optical techniques were used to measure the local deformations of the samples. The level of viscous behaviour was seen to increase as the temperature was lowered. A dip of the stress-strain behaviour was seen for one of the HNBR compounds tested at low temperatures, and a theory of matrix-particle debonding was proposed to explain this dip. Unit cell simulations suggested that the observed stress dip might be caused by a reduction of the fracture energy of matrix-particle cohesive zones at low temperatures. For the test at higher temperatures, the samples were found to display premature material failure during the deformation cycles.

Paper II illuminates the difference in volumetric behaviour obtained in uniaxial tension and confined axial compression experiments on HNBR and FKM elastomers. While a stiff and fully elastic volumetric response was obtained for both materials in confined axial compression, with a volume reduction of about 6 % for a hydrostatic stress level of 140 MPa, a relatively compliant and viscous volume behaviour was found in uniaxial tension, with nearly 20 % volume increase at a hydrostatic stress of about 6 MPa found for the FKM compound. This difference has severe implications for the constitutive modelling of elastomeric materials. To increase the understanding of the micromechanical mechanisms causing the large difference in volume behaviour between the loading modes, an in situ scanning electron microscopy study was performed to examine if matrix-particle decohesion can occur during uniaxial tension. It was found that ZnO particles tend to debond from the matrix material during tension. Using finite element simulations of a unit cell configuration it was shown that such debonding could explain the volume response in uniaxial tension and confined axial compression in a qualitative manner.

Paper III pays attention to the volume growth accompanying uniaxial tension at temperatures from 23 to −18 ºC. A new experimental set-up, building on the experience made in Paper I, is outlined to measure volume growth accompanying uniaxial tension at low temperatures. A significant increase in the volume growth accompanying tension was found for all materials as the testing temperature was reduced. To incorporate the large volume changes in finite element simulations, a new constitutive model outlined in the framework of finite strains continuum mechanics is presented. The model alters the well-known visco-hyperelastic Bergström-Boyce model by use of a Gurson viscous flow potential to account for the matrix-particle decohesion observed in Paper II. The temperature dependence of the material parameters is included thorough the use of a simple mathematical relation and the model is shown to yield a good prediction of the experimental results.

Acknowledgements

I would first like to thank my supervisors, Professor Arild Holm Clausen and Professor Bjørn Helge Skallerud, for their support, guidance, and encouragement throughout this PhD project.

Aker Solutions are acknowledged for their financial support and giving me the opportunity to immerse myself in a long-term academic project. Especially, I would like to express my gratitude to Dr Ulf Skytte af Sätra at Aker Solutions for the educative and encouraging discussions during the initial phase of this project.

The contribution from Mr Tore Wisth and Mr Trond Auestad, both at the Department of Structural Engineering, on the preparation of test samples and the realization of the experimental work is highly appreciated. Mr Christian Oen Paulsen is acknowledged for his assistance with obtaining SEM images of the material samples. Dr Torodd Berstad and Dr David Morin at the SIMLab research group are acknowledged for their support related to the finite element implementation of the new constitutive model. The contribution of the suppliers who delivered test samples to the project free of charge is appreciated.

I would also like to thank my colleagues at the Department of Structural Engineering, and the SIMLab research group especially, for providing an inspiring and friendly working environment. You have made these three years a real pleasure.

Finally, I would like to thank my family and friends for the encouragement and support over the years.

CONTENTS

Appended papers

Appendix

1 INTRODUCTION

Particle-filled elastomeric compounds are widely used in engineering applications, examples being pneumatic tyres, seals, and vibration dampers. While such components often are relatively cheap to produce, the design process to obtain the optimal combination of geometry and material properties can be a costly affair. An example of such is the use of elastomeric seals in subsea trees.

Subsea trees are placed on top of seabed wellheads and used to control the flow of oil and gas from an oil well. To avoid leakages in a subsea tree, sealing technology is of crucial importance, with sealing solutions made of both metallic and polymeric materials being used. An illustration of such a tree, indicating some of its seals, can be seen in Figure 1. For the use of elastomeric materials for sealing applications, a new sealing design must pass strict qualification testing prior to installation [1]. These testing routines include variations in both temperature, between −20 and 150 ^{o}C, and pressure, from ambient to 140 MPa. Since post-testing inspection of seal designs failing the qualification routine seldom discloses any obvious reason for the leakage, a large portion of trial and error is included in the design of new sealing solutions. This search for a combination of sealing material and geometry that satisfies the qualification standard can thereby be very expensive, both in the sense of lead-time and man-hours. An alternative approach would be to introduce computer-aided design in the process, where numerical methods like finite element analyses can be used to predict the performance of a vast number of different designs. However, for such methods to be predictive of the sealing performance and thereby reducing the cost of qualification testing, they require constitutive models that capture the essential physics of the materials, in addition to representative input data. Today, the accuracy of such models are not sufficient to predict the performance of new sealing designs, therefore, increased knowledge on the behaviour and modelling of elastomeric materials exposed to a wide range of pressures and temperatures is needed.

Seals are exposed to multiple loading conditions, with tension, shear, and compression deformation dominating the installation process, while volumetric compression deformation govern when pressurized. In addition, thermal loadings can introduce volumetric expansion. A simple case study for a sealing application, see Appendix A.1, showed that the deviatoric behaviour of the sealing material was dominant for the response of the seal during

installation, while the hydrostatic compression response was the most important to predict the behaviour of a fully pressurized seal. Thereby, knowledge on the mechanical behaviour of elastomeric materials in various loading situations is needed to predict sealing behaviour.

In the oil and gas industry, the Hydrogenated Nitrile Butadiene Rubber (HNBR) material is known as the workhorse for sealing applications. The advantage of HNBR is its chemical and thermal stability, making it rather resistant to the severe subsea environment. An alternative for the more challenging service conditions is fluoroelastomer (FKM) materials. These compounds are generally more expensive than HNBR compounds, but are known to have increased temperature capabilities and improved compatibility with certain fluids. This study will focus on the behaviour and modelling of commercial HNBR and FKM compounds commonly applied for sealing applications in the oil and gas industry.

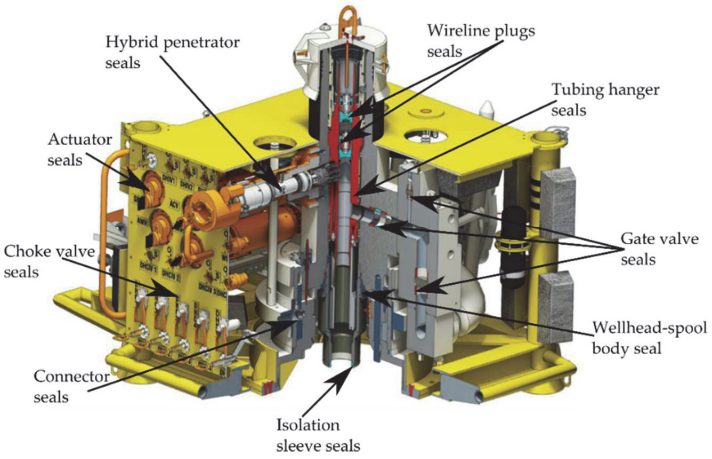

Figure 1: Example of sealing in a subsea tree.

This thesis consists of two main parts; in the first part, a synopsis containing the objectives and scope of the work, the theoretical background for the thesis, the materials tested and the research methods, a summary of the scientific contributions, and some suggestions for further work is given. Thereafter, the three articles providing the scientific contributions are presented in the second part. In the appendix, two conference contributions are included.

2 OBJECTIVES AND SCOPE

2.1 Objectives

The objective of this work is to improve the predictive capabilities of constitutive models for commercial elastomeric materials deformed at various temperatures. This is done through experimental tests, micromechanical investigations, and the proposal of a new constitutive model. A special focus is on the volumetric response of particle-filled materials. The objective of the thesis can be summarized as:

- To define and carry out experimental tests that examine the behaviour of commercial elastomers under different temperatures and loading modes
- To identify and investigate micromechanical mechanisms relevant for the mechanical response of commercial elastomer compounds
- To explore the capabilities and limitations of existing constitutive models
- To obtain a new constitutive model for elastomers, capturing the response observed in the experimental tests

2.2 Scope

The experimental part of the project is limited to two distinct types of elastomeric particle-filled polymers, being HNBR and FKM, while multiple compounds within each category is tested. Testing is performed on commercial materials; putting deep analysis of the materials chemical composition out of scope, as such knowledge could interfere with the suppliers' intellectual property. The temperature level of interest is aligned with the standard for qualification testing of elastomeric seals, being −20 to 150 ^{o}C [1]. The tests were performed at a low deformation rate such that isothermal conditions could be assumed, putting deformation induced temperature increase out of scope; the validity of this assumption is verified in Paper III.

The focus of the study is put on the behaviour of the materials in their first deformation cycle, although some effects of cyclic loading is included in Paper I. In addition, limited attention is payed to the strain rate dependence of the materials, yet viscous effects are discussed due to their presence in loading – unloading deformation cycles. Due to limited availability of specimen geometries and testing facilities specific for sealing applications, the thesis aims its

attention on generic research on the mechanical behaviour of elastomeric materials typically used in sealing applications, and is not limited to topics relevant for sealing applications only. Frankly, topics like swelling, chemical ageing, fatigue, and rapid gas decompression are considered outside the scope of this thesis, although highly relevant for sealing applications.

3 THEORETICAL BACKGROUND AND PREVIOUS WORK

This section presents a theoretical background for the scientific work in the appended papers. It gives a brief introduction on particle-filled elastomeric compounds, the mechanical properties of elastomers, and the continuum mechanical constitutive modelling of elastomeric materials.

3.1 Elastomeric compounds

The attractive mechanical properties of elastomeric materials are caused by their particular microstructural composition. Elastomers are polymeric materials, meaning that their basic molecule consists of a large number of repeated units, where the simplest repeated structure is called a monomer. As an example of a monomer, the chemical structure of HNBR is illustrated in Figure 2. In a blend of elastomeric polymer chains, only weak inter-molecular forces are initially present between the chains, and elastomers would have been soft and plastically deforming without the vulcanization technology. During vulcanization, a process that involves high temperatures and pressures, the elastomer chains become interconnected at multiple locations through the formation of new covalent bonds. These strong bonds ensure that the polymer chains are fixed relative to each other at the cross-linked sites, and thereby restrict permanent relative deformation between the chains. The difference between an unvulcanized and a vulcanized elastomer blend is illustrated in Figure 3, where the four cross linking sites are used to transform four separate polymer chains (a) into one large molecule (b). Traditionally, sulphur is added to the material for the vulcanization process, while for modern HNBR and FKM elastomers peroxide curing is normally used [2].

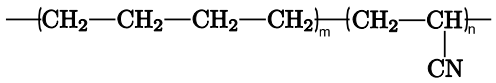

Figure 2: HNBR chemical composition

In addition to the vulcanized elastomer gum, different ingredients like carbon-black fillers, co-agents, desiccants and so on, are added to the blend to create an industrially applicable elastomer compound [3]. It should be noted that in modern synthetic elastomer materials, these additives could take up a considerable amount of the total volume compared with the vulcanized polymer chains [2]. Some of these ingredients can act as stiff inclusions in the elastomer matrix, as illustrated by the scanning electron microscope (SEM) image of an HNBR compound shown in Figure 4, where multiple high-contrast particles can be seen.

These observed particles, constituting of ZnO, will act as relatively stiff inclusions in the elastomer matrix, altering the mechanical behaviour compared with a pure elastomer gum.

a) Unvulcanized elastomer gum b) Vulcanized elastomer gum

Figure 3: Unvulcanized vs vulcanized elastomergum

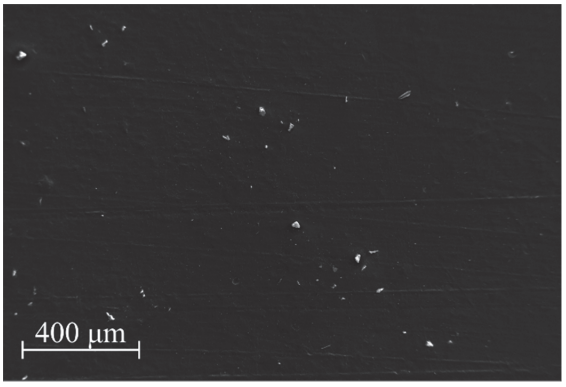

Figure 4: SEM image showing high-contrast particles in an HNBR elastomer compound

3.2 Mechanical behaviour of elastomers

3.2.1 Elasticity

Due to the cross-links between the polymer chains, elastomeric materials will return to its original configuration after the removal of a deforming load, even after large deformations. This large deformation elasticity is normally the desired feature when elastomers are used in industrial applications, and is in contrast to other engineering materials like metals and plastics, which would experience permanent deformations after small to moderate strains. In addition, the mechanism of the elasticity itself is different in elastomers compared with metallic materials. While the elastic deformation in metals is caused by inter-atomic displacements increasing the internal energy of the material, i.e. energetic elasticity, the elastic deformation of an elastomer gum is caused by rotation and stretching of the polymer chains between the cross-linking locations, reducing the entropy of the chain, i.e. entropic

elasticity. Unloading a stretched elastomer, the deformed chains would contract and reduced their end-to-end distances due to Brownian motions, increasing their entropy in the process.

3.2.2 Rate-dependence

The mechanical behaviour of elastomeric compounds is not purely elastic, as their mechanical response is also dependent on the loading rate, putting them in a class of viscoelastic materials. This time-dependence is important to include in constitutive models for elastomeric materials since it causes effects like stress relaxation, deformation creep, strain-rate dependency, and hysteresis loops in cyclic deformation. Although there is no consensus for the physical explanation of the viscous effects in elastomers, multiple theories based on micromechanical assumptions have been proposed.

The reptation-type tube theory by De Gennes [4] and Doi and Edwards [5] suggests that the micro-mechanical explanation of the viscous effects is Brownian motion of dangling chains. Figure 5 yields an illustration of this mechanism. In Figure 5a), three dangling chains can be seen in an unloaded cross-linked polymer network, while in Figure 5b) the same network is seen after being deformed to a stretched configuration. The dangling chains, first being deformed more or less affine with the rest of the network due to the entanglement of the chains, would gradually relax by the their Brownian motions. Due to the constraint of the chains in the compound being perpendicular to the shown cross-section of the network structure (indicated by dots in Figure 5), the configuration of the dangling chains is confined by a tube-like region. In the illustration of the loaded configuration, two chains are still entangled to the network and would contribute to the stiffness of the compound; for the third chain on the other hand, one end has disentangled from the network, removing the chain's contribution to the total stress-state. This mechanism could explain the strain-rate dependence, as a higher strain rate would allow for less Brownian motion in the chains during deformation and thereby a higher force level. In addition, a network deformed to a given strain level would experience stress relaxation as the dangling chains would relax and eventually slip out of the entanglement with the cross-linked network. However, Santagelo and Roland [6] showed that elastomers prepared to minimize the number of dangling chains still showed significant stress relaxation, and this theory is therefore unlikely to be the full explanation for the observed rate-dependent effects.

An alternative micromechanical explanation for the viscous effects is the transient network theory proposed by Green and Tobolsky [7]. The fundamental concept of the theory is that

chains are steadily breaking and reforming. As an example, the failure of short chains and the reforming of longer chains could give rise to stress relaxation effects in a tensioned network.

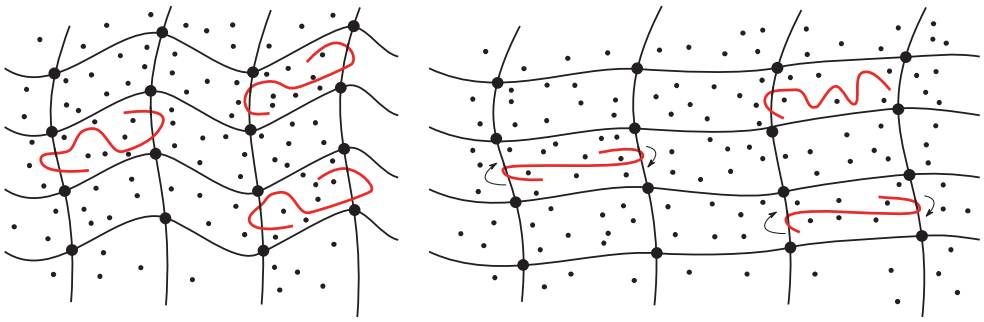

a) Unloaded network with dangling chains b) Tensioned network with dangling chains

Figure 5: Micromechanical reasoning behind the reptation-type tube theory for viscous effects in elastomers, dots indicate chains perpendicular to the illustrated cross section of the network

3.2.3 Volumetric behaviour

Compared with the number of studies dealing with the elastic and time-dependent behaviour of elastomeric materials, the volumetric response has gained limited attention. Frankly, the volumetric deformation of elastomeric materials is normally neglected, assuming the materials to behave isochoric, i.e. without any volume change during deformation. This classical assumption is based on comparisons between the typical shear modulus of elastomers [8] and their bulk modulus [9–11], showing that the bulk modulus found from hydrostatic compression tests are multiple orders of magnitude larger than the shear modulus found from simple shear or uniaxial tension tests. During loading of a material, the deformation mode will conform to that of the lowest possible strain energy. Due to the large ratio between bulk and shear modulus, an elastomeric material would therefore be expected to deform nearly isochoric during unconfined deformation.

However, these theories are based on observations of raw gum elastomers, which have limited industrial application. For all industrially applied materials, filler particles are added to the blend [3]. These fillers can improve mechanical properties like stiffness and strength, but may also alter the volumetric behaviour of the compound. Gent and Park [12] and Cho et al. [13] studied the effect of stiff particles in elastomers by adding glass inclusions with spherical or cylindrical shapes in a transparent matrix and testing samples in uniaxial tension. In both studies, matrix-particle decohesion was observed, leading to a volume increase of the test samples. They differentiated between two failure mechanisms; cavitation, i.e. the occurrence

of voids in the material due to stress concentrations near the stiff inclusions; and decohesion, i.e. rupture of the cohesive zone between the inclusion and the matrix material. The failure process was initiated by the occurrence of small voids close to the stiff inclusion, which during deformation grew and coalesced to form larger cavities. As these cavities increased in size, they eventually led to decohesion between the filler particle and the surrounding elastomer matrix. The process is illustrated in Figure 6. For deformation modes involving large hydrostatic tension stresses, Gent and Lindley [14] also found cavitation to occur in the interior of inclusion-free samples. For an industrial compound, it is reasonable to expect that the stress/deformation level at which cavitation and/or decohesion would occur is strongly dependent on properties like the fracture strength of the matrix material, the size and shape of the filler particles, and the cohesive strength between the matrix and the particles.

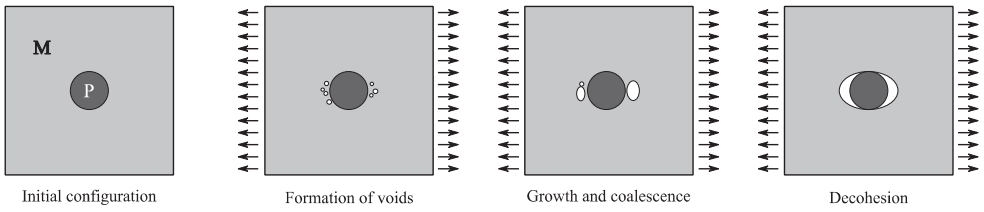

Figure 6: Illustration of void formation and decohesion in an elastomer matrix (M) with one embedded particle (P)

Previously, the most accessible method for measuring global volume change accompanying tension of elastomeric materials was through dilatometry studies [15–18]. However, technological advances such as SEM and Digital Image Correlation (DIC) techniques have paved the way for new studies on matrix-particle decohesion and the macroscopic volumetric response of elastomers. In recent studies, DIC has been used to measure the volume growth accompanying tension of different elastomeric compounds [19–21], generally finding significant global volume increase at large strains. A number of different studies have looked at matrix-particle decohesion in elastomeric samples using post-deformation and in situ SEM for the purpose of studying the fatigue properties of the materials [22–26], and although not the focus of these studies, the matrix-particle debonding that was found can be assumed to have caused a macroscopic volume growth. From the SEM studies, it was generally observed that ZnO particles were especially prone to decohesion, due to their weak cohesive strength with the surrounding elastomer matrix. The effect of this matrix-particle decohesion induced volume growth for the mechanical behaviour and constitutive modelling of elastomers has gained limited attention in the literature; this is discussed further in Paper II of this thesis.

3.2.4 Temperature effects

The effect that temperature has on the mechanical behaviour of elastomeric materials is widely studied. The general findings in the available literature are that the elastic stiffness and the viscous effects are enhanced as the temperature is reduced [27–35]. Below a certain temperature, elastomers turn into a hard and brittle material. The temperature for which this happens is called the glass transition temperature, and is distinct for each elastomer compound. Strictly speaking, the glass transition does not happen at a given temperature, but rather over a temperature range in which the behaviour gradually changes from soft and elastic to hard and brittle. For engineering purposes, the desired properties of an elastomer would normally be its soft and elastic response, and it is therefore important that the glass transition temperature is well below the service temperature of the product. It can also be noted that the glass transition temperature is pressure dependent, with a rule of thumb being a 1 ^{o}C increase in the transition temperature for each 5 MPa of external pressure [36]. The general temperature dependent behaviour of HNBR and FKM materials is studied in Paper I.

The volumetric response at different temperature levels has gained limited attention in the literature. Wood and Martin [10] studied the compressibility of an elastomer for temperatures ranging between 0 and 25 ^{o}C, indicating that the bulk modulus is reduced with temperature. However, no published studies addressing the volume growth accompanying tension of elastomers at various temperature levels could be found. However, this is studied in Paper III of this thesis, where it is shown that the volume growth accompanying tension due to matrix-particle decohesion is strongly temperature dependent, with the volume growth obtained at a given deformation increasing as the temperature is reduced.

3.3 Constitutive modelling of elastomers

3.3.1 Preliminaries

3.3.1.1 Stress and strain measures

Different stress and strain measures can be obtained from experimental mechanical testing. The most used of these measures are briefly discussed here by considering the uniaxial tension deformation of a cube with initial dimensions L_0 for all edges. The cube is subjected to a force F in the 1 direction, as illustrated in Figure 7.

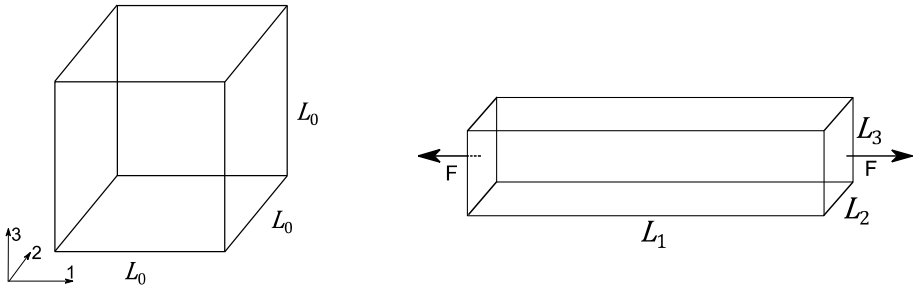

a) Undeformed configuration b) Deformed configuration

Figure 7: Illustration of uniaxial tension deformation

The strain measure often referred to as *engineering strain*, e, is defined as the relative deformation in a given direction

$$e_i = \frac{L_i - L_0}{L_0} \tag{1}$$

where $i = 1,2,3$. The *stretch* on the other hand is defined by the relative length of the sides of the cube

$$\lambda_i = \frac{L_i}{L_0} = 1 + e_i \tag{2}$$

For large deformations the *logarithmic strain*, ϵ, is the most used, being defined from the strain increments

$$d\epsilon = \frac{dL}{L} \rightarrow \epsilon_i = \int_{L_0}^{L_i} \frac{dL}{L} = \ln \frac{L_i}{L_o} = \ln \lambda_i \tag{3}$$

From the three stretch values, the *volume ratio* of the cube, J, can be found

$$J = \frac{V}{V_0} = \frac{L_1 L_2 L_3}{(L_0)^3} = \frac{\lambda_1 L_0 \lambda_2 L_0 \lambda_3 L_0}{(L_0)^3} = \lambda_1 \lambda_2 \lambda_3 \tag{4}$$

The longitudinal normal stress in the cube can be defined by the *engineering stress*, S_1

$$S_1 = \frac{F}{A_0} \tag{5}$$

where $A_0 = (L_0)^2$. However, a more precise stress measure, taking the actual area of the cube into account, is the longitudinal *Cauchy stress*, σ_1

$$\sigma_1 = \frac{F}{A} \tag{6}$$

where the current area can be found from $A = L_2 L_3 = \lambda_2 \lambda_3 A_0$.

3.3.1.2 Kinematics in continuum models

A brief summary of continuum mechanics is included here to introduce notation for the coming sections. For a more thorough discussion of the concepts, the reader is referred to the textbooks by Belytschko et al. [37], Holzapfel [38], and Bergström [39].

Considering a deformable solid, the deformation gradient tensor $\mathbf{F}$ defines the relation between every material point $\boldsymbol{X}$ in the reference configuration with the location of the same points in the current configuration $\boldsymbol{x}$

$$\mathbf{F} = \frac{\partial \boldsymbol{x}}{\partial \boldsymbol{X}} \tag{7}$$

From the deformation gradient, the right and left Cauchy-Green deformation tensors can be defined, $\mathbf{C} = \mathbf{F}^{\mathrm{T}}\mathbf{F}$ and $\mathbf{b} = \mathbf{F}\mathbf{F}^{\mathrm{T}}$ respectively. Important for the modelling of elastomers are the three principal invariants of the Cauchy-Green deformation tensors (being the same values for both tensors)

$$\begin{aligned} I_1 &= \mathrm{tr}(\mathbf{C}) = \lambda_1^2 + \lambda_2^2 + \lambda_3^2 \\ I_2 &= \frac{1}{2}[\mathrm{tr}(\mathbf{C})^2 - \mathrm{tr}(\mathbf{C}^2)] = \lambda_1^2\lambda_2^2 + \lambda_1^2\lambda_3^2 + \lambda_2^2\lambda_3^2 \\ I_3 &= \det(\mathbf{C}) = \lambda_1^2\lambda_2^2\lambda_3^2 \end{aligned} \tag{8}$$

where $\mathrm{tr}(\circ)$ denotes the trace of the tensor, $\det(\circ)$ is the determinant of the tensor, and λ_i the principal strain in direction i. The volume ratio of the material can be found as the determinant of the deformation gradient and, following Equation (4), is related to I_3 as

$$J = \det(\mathbf{F}) = \sqrt{I_3} \tag{9}$$

Using the volume ratio, the deformation gradient can be split multiplicatively in purely distortional and volumetric parts, denoted $\mathbf{F}^*$ and $\bar{\mathbf{F}}$ respectively

$$\mathbf{F} = \mathbf{F}^*\bar{\mathbf{F}} \tag{10}$$

where $\mathbf{F}^* = J^{-1/3}\,\mathbf{F}$ and $\bar{\mathbf{F}} = J^{1/3}\,\mathbf{I}$ where $\mathbf{I}$ is the second order unit tensor. Thereby, purely distortional right and left Cauchy-Green deformation tensors can also be defined

$$\mathbf{C}^* = \mathbf{F}^{*\mathrm{T}}\mathbf{F}^*, \quad \mathbf{b}^* = \mathbf{F}^*\mathbf{F}^{*\mathrm{T}} \tag{11}$$

and the invariants of the distortional tensors read $I_1^* = \mathrm{tr}(\mathbf{C}^*)$, $I_2^* = \frac{1}{2}\left[\mathrm{tr}(\mathbf{C}^*)^2 - \mathrm{tr}\left(\mathbf{C}^{*2}\right)\right]$, and $I_3^* = 1$. It can be noted that an assumption of isochoric material behaviour would imply a constant volume ratio of $J = 1$, and thereby $\mathbf{F}^* = \mathbf{F}$.

3.3.2 Hyperelastic modelling

The most fundamental constitutive relations for elastomeric material behaviour are the hyperelastic material models. Such models capture the large strain elasticity observed in elastomers, while the time-dependence is omitted. The idea of a hyperelastic model is to assume that the strain energy of the material can be represented by a mathematical potential function W. Assuming isotropic material behaviour, the Cauchy stress tensor can then be found from the strain energy potential function through [38]

$$\boldsymbol{\sigma} = \frac{2}{J}\mathbf{F}\frac{\partial W(\mathbf{C})}{\partial \mathbf{C}}\mathbf{F}^{\mathrm{T}} = \frac{2}{J}\left(\frac{\partial W}{\partial I_1} + I_1\frac{\partial W}{\partial I_2}\right)\mathbf{b} - \frac{2}{J}\frac{\partial W}{\partial I_2}\mathbf{b}^2 + \frac{\partial W}{\partial J}\mathbf{I} \tag{12}$$

It is a common approach to split the strain energy potential additively in an isochoric and a volumetric part

$$W = W_{iso}(I_1^*, I_2^*) + W_{vol}(J) \tag{13}$$

Penn [18] argued that such a split was incapable of reproducing experimental data from both uniaxial tension and hydrostatic compression. However, the material that Penn did his experimental work on was a pure gum natural rubber, potentially not representative for modern particle filled synthetic elastomers. Ehlers and Eipper [40] echoed Penn's criticism of the additive split by showing that such a split could lead to an unphysical response at large uniaxial deformations. On the other hand, Sansour [41] argued that the isochoric-volumetric split is both mathematically and physically appropriate. Some models which do not make use of the additive split have been proposed for compressible elastomeric materials, like Simo and Pister [42] for a compressible neo-Hookean model and Bischoff et al. [43] for a compressible eight-chain model, but the majority of the models presented in the literature takes advantage of the simplifications that the split offers.

3.3.2.1 Isochoric part

A review of different hyperelastic models for the isochoric behaviour has been given by Treloar [8], Boyce and Arruda [44], and in the recently published textbook by Bergström [39]. Generally, strain energy potential functions for the isochoric part can be divided in to two groups; phenomenological or micromechanically based models. Most phenomenological

strain energy potentials gaining widespread application can be obtained as special cases of the general Mooney-Rivlin polynomial function [45]

$$W_{iso} = \sum_{i=0}^{n}\sum_{j=0}^{m} C_{ij}(I_1^* - 3)^i (I_2^* - 3)^j, \quad C_{00} = 0 \tag{14}$$

Well known truncations of the expression is the neo-Hookean model [46] $(n = 1, m = 0)$, the Mooney-Rivlin potential [47] $(n = 1, m = 1)$, and the Yeoh model [48] $(n = 3, m = 0)$. Another phenomenological potential function that should be mentioned in this context is the one proposed by Ogden [49] and expressed in terms of the principal stretch ratios.

Physically based models are generally derived from a statistical consideration of single chains interacting in a multiple-chain network. The entropic properties of a single chain can be derived in a simple Gaussian framework assuming only moderate deformations, or in a more complex non-Gaussian framework based on the Langevin chain statistics developed by Kuhn and Grün [50]. Using a non-Gaussian chain consideration, numerous network models have been proposed, like the three-chain model [51] , the four-chain model [52], and the widely applied eight-chain model by Arruda and Boyce [53]. Here, the eight-chain model will be considered, as it is used in Paper II and III. An illustration of the micromechanical foundation for the model is shown in Figure 8, with a cube consisting of eight chains connected together in the centre. The connection between the chains is assumed to remain in the centre of the cube during deformation, and the following strain-energy potential can thereby be obtained

$$W_{iso} = \mu\lambda_L \left(\lambda_c \beta + \lambda_L \ln\left(\frac{\beta}{\sinh \beta}\right)\right) \tag{15}$$

where μ and λ_L are material parameters, β is defined as $\beta = \mathcal{L}^{-1}\left(\frac{\lambda_c}{\lambda_L}\right)$, and $\lambda_c = \sqrt{I_1^*/3}$. The inverse Langevin function $\mathcal{L}^{-1}(\circ)$ is defined from $\mathcal{L}(x) = \coth x - 1/x$. An exact closed-form solution to the inverse Langevin function has not yet been found, however, a range of approximate solutions have been proposed [54]. The equation for the isochoric part of the Cauchy stress tensor can, by use of Equation (12), be obtained as

$$\boldsymbol{\sigma}_{iso} = \frac{\mu\lambda_L}{3J\lambda_c}\mathcal{L}^{-1}\left(\frac{\lambda_c}{\lambda_L}\right)(\mathbf{b}^*)' \tag{16}$$

where the deviator of a tensor $\mathbf{A}$ is defined as $\mathbf{A}' = \mathbf{A} - \left(\frac{1}{3}\mathrm{tr}\mathbf{A}\right)\mathbf{I}$

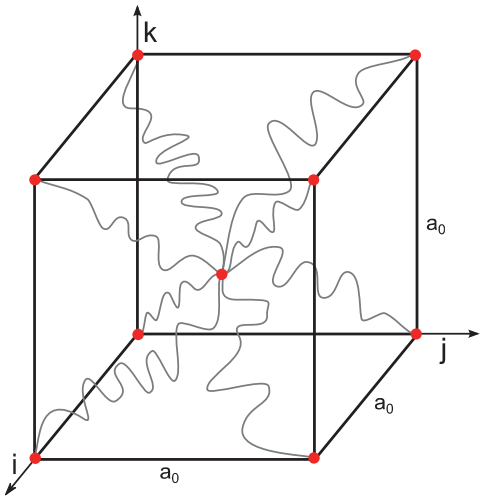

Figure 8: Micromechanical representation of the eight-chain model

3.3.2.2 Volumetric part

Strain energy potential functions for the volumetric part $W_{vol}(J)$ of hyperelastic relations have not gained the same widespread research attention as the isochoric response, due to the volume preserving material behaviour so often assumed for elastomers. However, different potential functions have been proposed and a discussion of those is included in the review by Boyce and Arruda [44], and in the works of Bischoff et al. [43], Doll and Schweizerhof [55], and Horgan and Murphy [56]. Generally, the proposed models for the volumetric response are purely phenomenological, being mathematical expressions satisfying the physical limitations of a potential function (e.g. the strain energy going to infinity as the volume goes to zero) and showing a decent consistency with available experimental data. Some of the volumetric strain energy functions proposed in the literature are given in Equation (17).

$$
\begin{aligned}
W_{vol}^{a} &= \frac{\kappa}{2}(J-1)^2 \Rightarrow \boldsymbol{\sigma}_{vol}^{a} = \kappa(J-1)\mathbf{I} \\
W_{vol}^{b} &= \frac{\kappa}{2}\left(\frac{J^2-1}{2} - \ln J\right) \Rightarrow \boldsymbol{\sigma}_{vol}^{b} = \frac{\kappa}{2}\left(J - \frac{1}{J}\right)\mathbf{I} \\
W_{vol}^{c} &= \frac{\kappa}{2}(\ln J)^2 \Rightarrow \boldsymbol{\sigma}_{vol}^{c} = \kappa\frac{\ln J}{J}\mathbf{I}
\end{aligned}
\tag{17}
$$

The simplest function is to assume a linear pressure – volume ratio relation as in W_{vol}^{a} [57,58]. The slightly more complex function in W_{vol}^{b} is used for the Abaqus implementation of the eight-chain model [59] (Abaqus Theory Guide Section 4.6.1), and also applied in [60,61]. Alternatively, a logarithmic potential as in W_{vol}^{c} has been widely applied in the literature [62–

65]. The three different functions are compared in Figure 9 for a volume ratio ranging from 0.8 to 1.2. A κ value of 1 GPa is used, as often applied to impose nearly isochoric response in elastomer modelling. Going from expression a) to c), an increase in non-linearity can be observed, with the difference from the linear relation getting more pronounced as the volume change increases. While both the non-linear terms are seen to yield a slightly softer volumetric response in tension compared with compression, they are not able to incorporate the large difference in volumetric behaviour caused by matrix-particle decohesion, as discussed in Paper II. The term W_{vol}^{b} is used for the volumetric part of the stress tensor in the new constitutive model in Paper III.

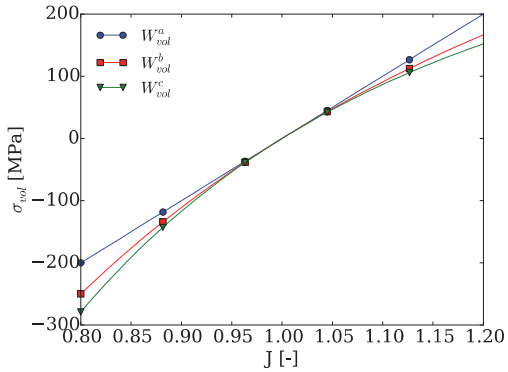

Figure 9: Illustration of volumetric response resulting from the three strain energy functions proposed in the literature, see Equation (17) ($\kappa = 1$ GPa)

3.3.3 Viscoelastic modelling

Due the inhibited viscous effects of modern elastomeric materials, as discussed in Section 3.2.2, purely hyperelastic material models fall short in accurate numerical predictions of the general material behaviour. To include the time-dependency in a modelling framework, both phenomenological models [66,67], and micromechanically motivated models building on the reptation-type tube theory [68–70] and the transient network theory [71–73] have been proposed.

The model based on the reptation-type tube theory put forward by Bergström and Boyce [68] has gained widespread application and is implemented as a built-in material model in commercial finite element codes like Abaqus [59] and LS-DYNA [74]. This model is utilized in this thesis for both the unit cell modelling in Paper II, and as a point of departure for the new constitutive model proposed in Paper III. A 1D rheological illustration of the model is shown in Figure 10. The model consists of two parallel branches, one containing a

hyperelastic spring exclusively, and one consisting of a hyperelastic spring in series with a non-linear dashpot. Any strain-energy potential function can be used for the two springs, with the eight-chain model given in Equation (15) combined with one of the volume terms in Equation (17) the most commonly applied, as also used in the original derivation of the model. The deformation of the two parallel parts is equal and the total stress is the sum of the stresses in the two springs, mathematically given as $\mathbf{F} = \mathbf{F}_\mathrm{A} = \mathbf{F}_\mathrm{B}$ and $\boldsymbol{\sigma} = \boldsymbol{\sigma}_\mathrm{A} + \boldsymbol{\sigma}_\mathrm{B}$. The deformation gradient of Part B is multiplicatively split between the elastic spring and the viscous non-linear dashpot, i.e. $\mathbf{F}_\mathrm{B} = \mathbf{F}_\mathrm{B}^e \mathbf{F}_\mathrm{B}^v$. The behaviour of the dashpot is given by a non-linear constitutive equation

$$\dot{\gamma} = \dot{\gamma}_0 \, (\lambda_v - 1 + \zeta \,)^c \left(\frac{\sqrt{\boldsymbol{\sigma}'_\mathrm{B} : \boldsymbol{\sigma}'_\mathrm{B}}}{\tilde{\tau}} \right)^m \tag{18}$$

where $\dot{\gamma}$ is the effective viscous strain rate, $\dot{\gamma}_0$ is a parameter introduced for dimensional consistency, $\lambda_v = \sqrt{\frac{1}{3}\mathrm{tr}\mathbf{b}^{*v}_\mathrm{B}}$, ζ is a small valued scalar to ensure numerical stability in the reference configuration (i.e. for $\lambda_v = 1$), c is a material parameter in the range $[-1,0]$, the symbol : denotes the contraction of the two tensors, and m and $\tilde{\tau}$ are material parameters. The full derivation of the model and its modifications to include the effects of matrix-particle decohesion are included in Paper III.

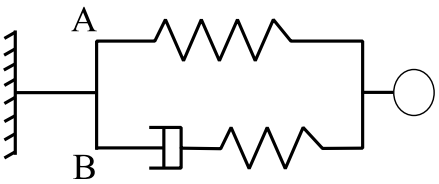

Figure 10: Rheological representation of the Bergström-Boyce model

3.3.4 Thermomechanical modelling

To include thermal effects in the constitutive modelling of elastomeric materials it is common to split the deformation gradient multiplicatively in a thermal and a mechanical part [28,75–77]

$$\mathbf{F} = \mathbf{F}_\mathrm{M} \mathbf{F}_\theta \tag{19}$$

where $\mathbf{F}_\theta$ defines the thermal deformation gradient representing the mapping from the reference configuration Ω_0 to a stress-free thermally deformed configuration Ω_θ, while $\mathbf{F}_\mathrm{M}$ is the mechanical deformation gradient representing the isothermal mapping from Ω_θ to the

current configuration Ω. An illustration of this split is included in Figure 11. The thermal deformation gradient is defined as [75]

$$\mathbf{F}_\theta = \exp\left[\int_{\theta_0}^{\theta} \alpha(\theta) d\theta\right] \mathbf{I} \tag{20}$$

where $\alpha(\theta)$ is the temperature dependent coefficient of thermal expansion. For the elastomers tested in this thesis, an introductory study found that this expansion factor was in the range $[1.0 - 3.5]\times 10^{-4}\mathrm{K}^{-1}$, decreasing as the temperature was increased from 50 to 125 ºC.

For simulations involving large temperature variations, the effect of thermal deformation can be important to take into account. However, when modelling elastomers deformed under constant external conditions, only the deformation induced heating would give a contribution to the temperature change of the material. For low strain rates, this heating might be negligible, resulting in isothermal simulations where the temperature dependence of the model is limited to the material parameters [75]. Bergström and Hilbert [78] modelled the isothermal behaviour of fluoropolymers in this manner, defining the temperature dependent shear modulus by

$$a(\theta) = a_0 \exp\left[\frac{\theta_0 - \theta}{\theta_{base}}\right] \tag{21}$$

where $a(\theta)$ is the material parameter as a function of the temperature θ, a_0 is the parameter value at the reference temperature θ_0, and θ_{base} is a scaling temperature. This temperature expression is used for a set of the material parameters in the constitutive model presented in Paper III. Using this approach limits the model to give predictions on the material behaviour during isothermal deformations at different temperature levels.

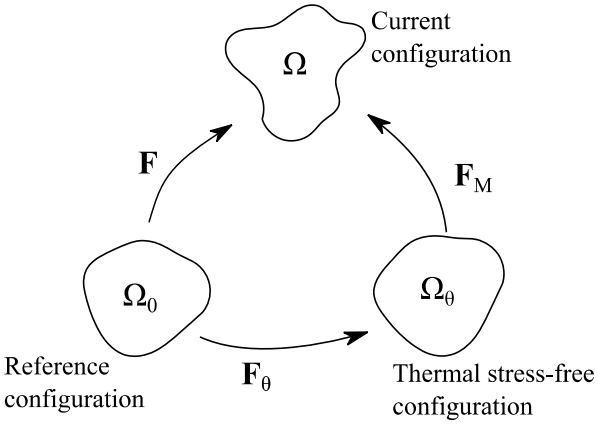

Figure 11: Illustration of the multiplicative split of the deformation gradient in thermal and mechanical contributions

4 MATERIALS AND METHODS

This section introduces the different materials tested in the appended papers, and discusses some of the research methods used to obtain the scientific results.

4.1 Materials and specimen dimensions

Three different suppliers delivered test samples to this project. Since all tested materials are commercial compounds, suppliers and identifying trade names are anonymized, and the three suppliers are denoted A, B, and C. In addition, the exact chemical compositions of the materials were unknown to the authors to protect the intellectual property of the respective companies. An overview of the different materials tested, their measured density, and in which part of the work they figure are listed in Table 1. The different dumbbell tension sample geometries used in this research is illustrated in Figure 12. While the ISO geometry samples in Figure 12a) and Figure 12b) were prepared by the suppliers and used for the macroscopic tension tests in all three papers, the smaller samples with the geometry in Figure 12c) were cut from the ISO sized samples using water jet, and applied for the in situ SEM experiments in Paper II. The cylindrical samples used for the confined axial compression tests in Paper II (and A.2) had a height of 12.5 mm and a diameter of 29 mm in line with ISO 815-1 Type A [79]. While supplier A provided both dumbbell (ISO37 – type 1) and cylindrical specimens, supplier B provided dumbbell specimens exclusively (ISO37 – type 2), and supplier C only cylindrical specimens.

Table 1: Overview of tested materials

Supplier	Elastomer material	Density (g/cm^3)	Tested in paper
A	HNBR	1.29	I, II, III, A.2
B	HNBR	1.19	I, III
B	FKM	1.77	I, II, III
C	HNBR	1.23	A.2
C	HNBR	1.29	A.2
C	HNBR	1.16	A.2
C	FKM	2.33	II, A.2
C	FKM	1.84	II, A.2

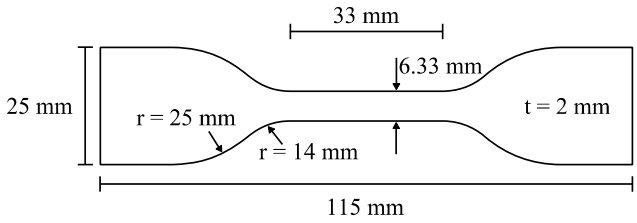

a) Dimension delivered by supplier A (ISO37 – type 1)

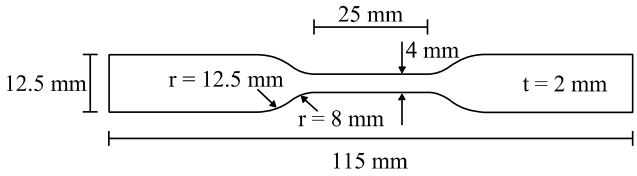

b) Dimension delivered by supplier B (ISO37 – type 2)

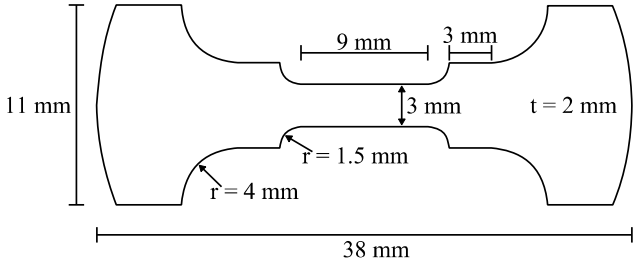

c) Dimension used for in situ SEM investigations

Figure 12: Dimensions of dumbbell samples used in Paper I, II, and III. Note the difference in scale.

4.2 Experimental methods

The main part of the mechanical testing carried out in this thesis was done using the testing facilities of the Department of Structural Engineering, NTNU. However, the laser flash study carried out in Paper I was performed by SINTEF Materials and Chemistry in Trondheim, while for the in situ SEM study carried out in Paper II, facilities at the Department of Materials Science and Engineering at NTNU were used.

4.2.1 Uniaxial tension vs uniaxial compression

At a first glance, uniaxial compression experiments might seem to be the natural type of test for elastomeric materials to be used in sealing applications. However, the main part of the experimental work performed in this thesis is uniaxial tension tests. After conducting both uniaxial tension and uniaxial compression tests in an introductory study, measuring local

deformations by the use of optical methods, uniaxial tension tests were preferred due to the ease of experimental execution and data interpretation.

The drawback of uniaxial compression tests stems from the frictional forces that arise between the specimen and the compression platens of the testing machine. These forces lead to a multiaxial stress field that causes a heterogeneous deformation, making for complex data interpretation. In addition, precise measurements of the volume change during uniaxial compression testing are an intricate affair. It should be emphasized that measures like Teflon tape or grease between the specimen and the compression platens reduce, but do not defer these challenges. On the other hand, uniaxial tension tests of elastomers give a nearly homogenous deformation field, a uniaxial stress state, and a simple way of measuring the volumetric deformations.

4.2.2 Confined axial compression

To obtain data on the materials response when subjected to negative hydrostatic stresses, confined axial compression experiments were performed in Paper II (the study being fully outlined in the conference paper in A.2). Due to the confinement, this experimental compression procedure is not biased by bulging and inhomogeneous deformations as in uniaxial compression tests. However, frictional forces arise between the specimen and the confinement, and to obtain simple interpretation of the test data it is important that these forces are so low that the stress situation is dominated by hydrostatic stresses. In the proposed experimental set-up, a load cell was included both above and below the sample, with the difference in the measured forces stemming from friction. Using a silicon grease between the specimen and the confinement, the frictional forces were found to be at an acceptable level.

4.2.3 Optical measurements

The use of optical measurement techniques, applying one or two digital cameras, is highly relevant for the study of polymeric materials. The advantages of optical methods over traditional contact-extensometers are many. As an example, a set of images of the surface of a sample during a test can give information on the deformations in multiple directions, like longitudinal and transverse directions in a uniaxial tension test, and at multiple locations. In addition, the use of optical methods is not affected by the test temperature, a feature utilized in Paper I and III. A drawback with these optical methods is the large data storage requirements, as an image, potentially containing thousands of pixels, must be stored for each data point to be obtained from the test. However, this drawback is of diminishing relevance as

the cost of data storage has plunged over the last decades. In this thesis, three different optical measurement techniques are used; point tracking, edge tracing, and full field DIC.

The simplest method was used for the confined axial compression tests in Paper II. Here, the rigid displacement of the piston that deforms the specimen was measured. A checkerboard pattern was applied to the piston prior to testing and a CCD camera was used to capture images of this pattern during the tests. In the post-processing of the experimental data, a corner detector routine [80] was used find the corners of the pattern in all images, and thereby to obtain the rigid deformation of the piston in pixels. The mm/pixel relation of the checkerboard pattern in the images must then be obtained to calculate the correct displacement relative to the initial height of the specimen. Clearly, the accuracy of the method is dependent on the resolution of the image, as the measurable deformation is limited by the pixel size.

To measure local deformations at the surface of the uniaxial tension samples, the DIC technique [81] was used in Paper II and III. In this method, a random greyscale speckle pattern is applied to the surface of the test samples prior to deformation, and the displacements of a virtual mesh related to this pattern is calculated through correlating the images taken during the test. For the DIC measurements performed in this thesis, the in-house software eCorr [82] was used in the post-processing of the images. Traditionally, the speckle pattern is applied to the specimens by the use of black and white spray paint, and this method was successfully used for introductory experiments conducted at room temperature. For the tension tests preformed at low temperatures, on the other hand, cracking of the paint became a significant problem, as illustrated for an HNBR specimen tested at −20 ^{o}C in Figure 13. Due to the relatively homogeneous deformation of elastomers at large strains, i.e. no localization of deformation as seen in most plastically deforming polymeric and metallic materials, an alternative procedure utilizing an edge tracing method was implemented, see Paper I. In this routine, edges in an image are found by searching for peaks in the grey level gradient value along a pixel line. An illustration of the routine is shown in Figure 14, where the specimen with the edge of the sample and the edge of the painted area marked in a), and the grey level gradient along a specific x-pixel line is shown in b).

Although the edge trace routine could be used to obtain both longitudinal and transverse strains during a uniaxial tension test, a greyscale speckle pattern that would sustain large deformations at low temperatures would be preferable. Therefore, an alternative method of

applying the speckle pattern was developed in which the gauge section of the sample was covered with a thin layer of a transparent grease, before a fine-grained contrast powder was sprinkling in the greased area. For the experiments performed in Paper III, icing sugar was used as the powder to obtain a white contrast to the black specimens. The grease and icing sugar combination was found to be unaffected by the low temperature testing conditions as shown in Paper III. A comparison of traditional spray-painting and grease-plus-powder speckle patterns was given by Johnsen et al. [83].

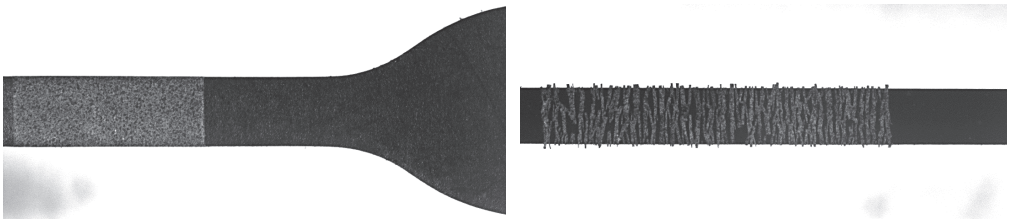

a) Specimen speckle pattern at initial configuration b) Specimen speckle pattern during deformation

Figure 13: Example of cracking in greyscale speckle pattern for an HNBR specimen tested at −20 ºC

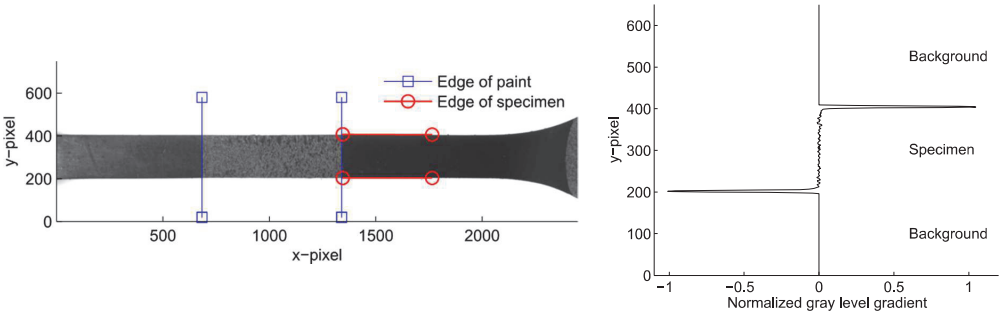

a) Example frame for edge tracing b) Grey level gradient for x-pixel line 1500

Figure 14: Example of edge tracing routine for HNBR1 material tested at −20 ºC

4.2.4 SEM study and image processing

To obtain images of the tested materials at a micrometre scale, a scanning electron microscope was used. Data on the particle size and distribution observed in the obtained micrographs were found by use of the Python image processing package scikit-image [84]. To differentiate between the matrix material and the particles in the micrographs, a process of image segmentation was applied. In such a process, each pixel is defined to be in either the matrix segment or the particle segment, depending if the greyscale value of the pixel is larger or smaller than a threshold level. The difficult part of this process is to define the threshold

level in a consistent manner. For the work in Paper II, Otsu's method [85] was used for this process. This method defines the threshold such that the combined variance in greyscale value of the two segments is minimized. An example of an original image and the binary image obtained after segmentation is shown in Figure 15. As illustrated, the segmentation process using Otsu's method to set the threshold value yields a reasonable result. When the binary image is found, clearly separating the particle phase from the matrix, the area fraction of the particle and matrix segments can easily be calculated. A labelling routine, defining the relation between neighbouring pixels, can then be utilized to define the size of each separate particle, and to count the total number of particles in the micrograph.

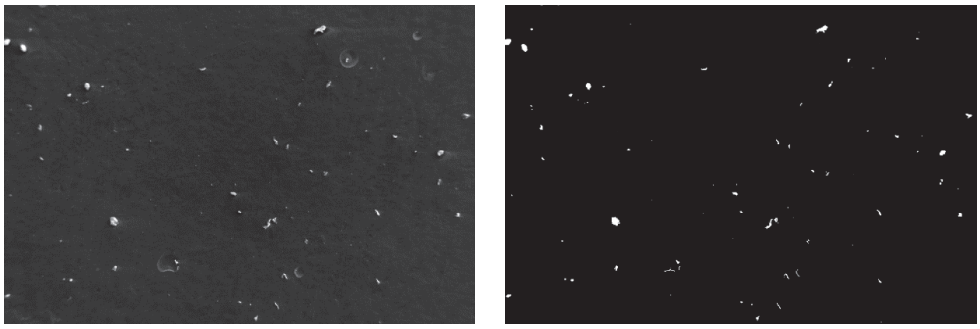

a) Original image b) Binary image

Figure 15: Example of SEM image segmentation

4.3 Numerical methods

Numerical calculations were employed in this thesis for two purposes. First, commercial finite element software and existing constitutive models were used in Paper I and II to model micromechanical effects at the mesoscale to gain increased understanding of the mechanisms underlying the macroscopic material behaviour. Second, a new constitutive model was developed and implemented as a user material model for commercial finite element software in Paper III.

While mesoscale models are useful for studies of the micromechanical phenomena that cause the material behaviour observed at the macroscale, they are not suitable for quantitative predictions of the macroscopic response, as this would require an extensive experimental database on the material constituents, their properties, and their interaction. In addition, imagining that such a database were available, predicting the material behaviour based on modelling the material at the level of its constituents for large parts exposed to large

deformations would require unreasonable amounts of computational power. However, a continuum-based framework (as briefly outlined in Section 3.3) where the compound is considered as a homogenous medium and the macroscopic behaviour is described by relatively simple mathematical formulations can be used for macroscale predictions. The experimental work needed to obtain the model parameters is then kept at a feasible amount, and the computation requirements are reduced to a level where large scale predictive simulations can be performed on personal computers or small computer clusters.

For the mesoscale simulations conducted in this thesis, the commercial finite element software Abaqus [86] was used for the simulations. The constitutive model developed in Paper III was implemented in Fortran as a user subroutine for the LS-DYNA finite element software [87]. This finite element code was chosen due to its neat integration with the optimization software LS-OPT [88], used to calibrate the model parameters to the experimental data.

5 SUMMARY OF WORK

The aim of this thesis is to increase the knowledge on the behaviour of elastomeric materials when subjected to different loading modes and a wide range of temperatures. The scientific contributions of the work are presented in the three articles listed in Table 2. While Paper I has been published in a peer-reviewed journal, Paper II is submitted for publication. Due to the close connection between Paper II and Paper III, the last article will be submitted to a journal after the publication of Paper II.

Prior to the writing of the journal articles, three conference contributions were prepared, as listed in Table 3. The articles published in the proceedings of two of these conferences are included in the appendix.

Table 2: Journal articles included in thesis

Paper	
I	A. Ilseng, B.H. Skallerud, A.H. Clausen *Tension behaviour of HNBR and FKM elastomers for a wide range of temperatures*. Polymer Testing 49 (2016), pp. 128-136
II	A. Ilseng, B.H. Skallerud, A.H. Clausen *An experimental and numerical study on the volume change of particle-filled elastomers in various loading modes.* Submitted for journal publication (August 2016)
III	A. Ilseng, B.H. Skallerud, A.H. Clausen *Volume growth during uniaxial tension of particle-filled elastomers at ambient to low temperatures – Experiments and modelling.* To be submitted for journal publication

Table 3: Conference contributions during PhD study

Appended in	Conference contribution
——	A. Ilseng, B.H. Skallerud, A.H. Clausen *Experimental study of the compressibility of an HNBR and an FKM elastomer.* 16th International Conference on Deformation, Yield and Fracture of Polymers, Kerkrade, the Netherlands, 2015
A.1	A. Ilseng, B.H. Skallerud, A.H. Clausen *Case study of elastomer seals using FEM.* Eighth national conference on Computational Mechanics, 2015, pp. 203-218 ISBN: 978-84-944244-9-6
A.2	A. Ilseng, B.H. Skallerud, A.H. Clausen *Volumetric compression of HNBR and FKM elastomers.* Constitutive Models for Rubber IX - Proceedings of the 9th European Conference on Constitutive Models for Rubbers, 2015, pp. 235-241 ISBN: 978-1-138-02873-9

Paper I:

This article presents uniaxial tension tests of two HNBR compounds and one FKM compound commonly applied as sealing materials in the oil and gas industry. The tests were performed at five different temperatures, ranging from −20 to 150 ^{o}C. Optical measurements were used to ensure high quality stress-strain data. However, due to the use of a commercial temperature chamber with only a single window for optical inspection of the test, the deformation state could only be measured at one surface of the specimens, and the volume change accompanying tension could not be calculated. The material samples were exposed to a cyclic deformation history, including a 30 minutes relaxation period. A considerable effect of temperature changes was found, with a pronounced increase of stiffness and viscosity for the lowest temperatures. A dip of the stress-strain behaviour was seen for one of the HNBR compounds tested at low temperatures; see Figure 16a). A theory of matrix-particle debonding was proposed to explain this dip, and unit cell simulations suggested that it might be caused by a reduction of the fracture energy of the matrix-particle cohesive zone at low temperatures; see Figure 16b) and c). For the tests performed at the highest temperatures, a considerable number of premature material fracture was encountered. Although FKM materials generally are stated to be particularly heat resistant compared with HNBR materials, the FKM material tested in Paper I experienced the largest number of material failures at high temperatures.

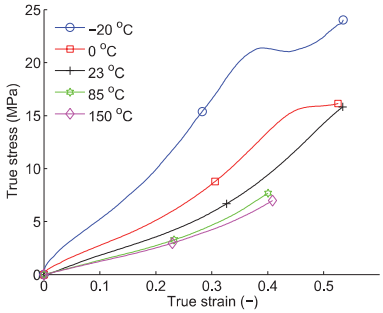

a) Experimental results for first loading of HNBR1 at all temperature levels

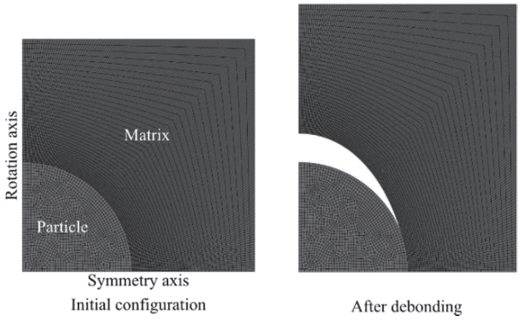

b) FEM model of matrix-particle debonding

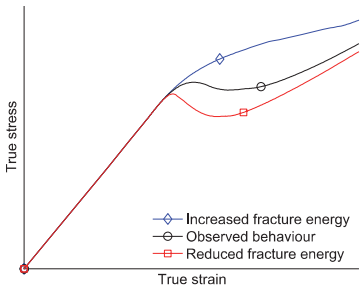

c) Simulation results from unit cell simulations for different fracture energies of the cohesive zone

Figure 16: Partial results from Paper I

Paper II:

In this work, the theory of matrix-particle debonding, as proposed in Paper I, is investigated further. From macroscopic tests on an HNBR and a FKM compound, the volumetric behaviour obtained in uniaxial tension and confined axial compression is compared; see Figure 17a) and b). Form the tests in the two deformation modes, significantly different volumetric responses are obtained, with a compliant and viscous response seen in tension, and a stiff and elastic behaviour found in confined axial compression. It is shown that this loading mode dependence of the volumetric response of the materials is not captured by constitutive models commonly used for elastomers. An increased understanding of the micromechanical mechanisms causing the macroscopic response is therefore needed. Although the volume behaviour in the tests align to the expectations from a matrix-particle debonding theory, it is not clear from the macroscopic experiments that such debonding actually takes place during tension. Therefore, in situ SEM experiments for tensioned specimens were carried out. Using the images captured in these experiments, data on the number and size of the ZnO filler particles is obtained at multiple locations of the samples. It was found that the FKM material, displaying a larger volume growth in uniaxial tension compared with the HNBR material, had both a larger total number of distinguishable particles and a larger particle fraction in the surface of the samples. During uniaxial tension, decohesion between the matrix material and ZnO particles could be found at multiple locations in the HNBR sample; see Figure 17c). For the FKM material, the reduced conductivity of the material during tension significantly reduced the image quality at large deformations, however, matrix-particle decohesion was also indicated to happen in this compound. To examine if the observed matrix-particle decohesion mechanism can explain the volumetric response obtained for the materials in the macroscopic experiments, a unit cell study was performed using an axisymmetric model resembling a cylinder of matrix material containing a spherical particle in its centre. A cohesive zone was applied at the interface between the matrix and the particle. The simulation results showed that the mechanical behaviour observed in the macroscopic experiments could be captured in a qualitative manner by the simple model. It was also indicated that the difference in volumetric behaviour in the tension tests between the HNBR and FKM material could be caused by differences in the cohesive zone properties.

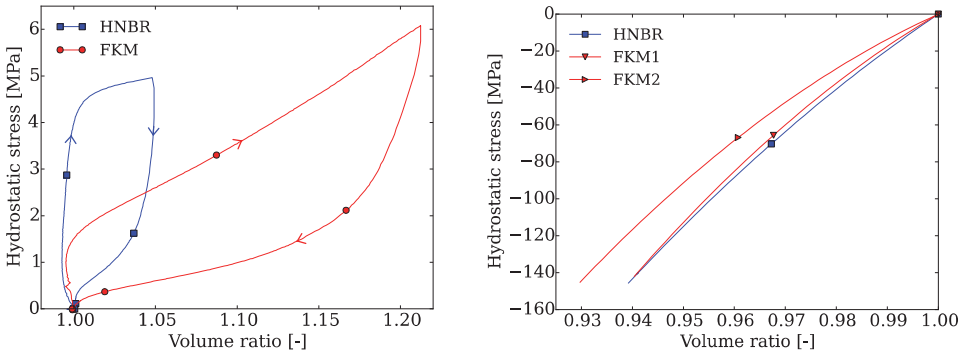

a) Uniaxial tension results

b) Confined axial compression

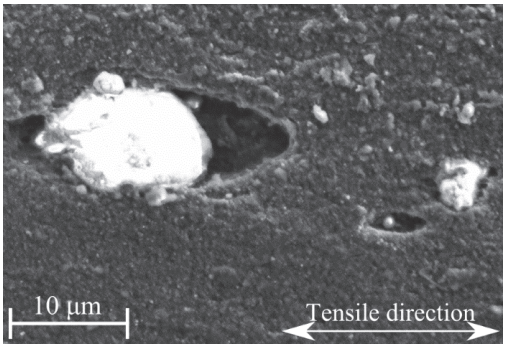

c) Particles debonding from the matrix in the HNBR material during in situ tension

Figure 17: Partial results from Paper II, showing the experimentally obtained volumetric behaviour in uniaxial tension and confined axial compression and matrix-particle decohesion obtained from the in situ SEM

Paper III:

In this part, the materials dealt with in Paper I are re-tested in tension at low temperatures with an experimental set-up utilizing 2×2D DIC, obtaining the full deformation field. With this set-up, novel data on the volumetric change accompanying tension at low temperatures are obtained. A significant increase of volume growth is obtained as the temperature is reduced; see Figure 18a). Based on the findings in Paper II, the volume growth is assumed to be caused by matrix-particle decohesion, with the temperature level effecting the properties of the cohesive zone between the matrix and the filler particles. To enable the observed behaviour to be predicted by finite element simulations, a novel continuum mechanical constitutive model is proposed. The point of departure for the model is the well-known visco-hyperelastic Bergström-Boyce model. Then, the large volume growth accompanying tension is included in the model by using the Gurson yield criterion as the flow potential function of the viscous dashpot. In addition, the rate equation for the viscous multiplier is changed to be governed by the full stress tensor rather than only the deviatoric part of the stress, such that a compliant volume response would be obtained also in hydrostatic tension. A simple mathematical relation was used to define the dependence on the testing temperature for a set of the model parameters. The novel constitutive model is shown to yield a good resemblance of the observed experimental behaviour, see Figure 18b). In addition to the temperature dependent tension behaviour, the model is shown to predict the stiff and elastic volumetric response of the materials under hydrostatic compression loading.

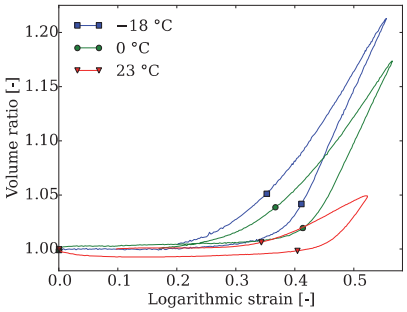

a) Temperature dependent volume growth for HNBR1

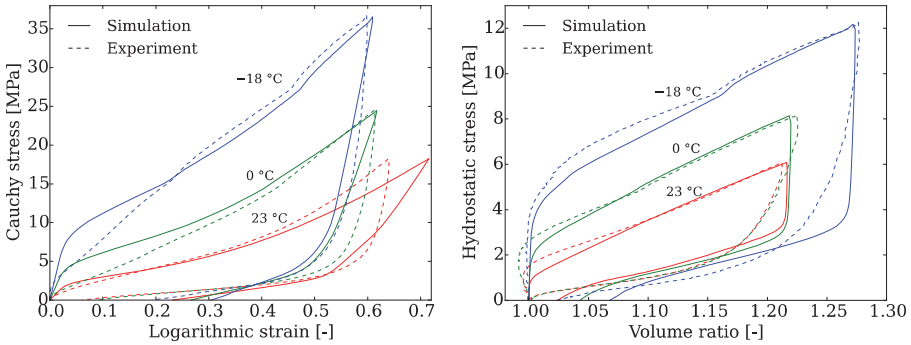

b) Comparison of simulation results and experimental data for the FKM compound

Figure 18: Partial results from Paper III showing the increased volume growth occurring at low temperatures in the HNBR1 material and simulation results using the novel constitutive model

6 CONCLUDING REMARKS

The work in this thesis investigates the behaviour and modelling of commercial particle-filled elastomeric materials for a wide range of temperatures. The main scientific contributions are:

- An experimental database on the tension behaviour of HNBR and FKM materials for a temperature range from −20 to 150 ^{o}C (Paper I)
- New insight into the considerable difference in volumetric response between uniaxial tension and confined axial compression for particle-filled elastomers (Paper II)
- In situ SEM studies proving that significant matrix-particle decohesion occurs in the elastomer materials during tension (Paper II)
- A new experimental procedure to measure volumetric growth accompanying tension of HNBR and FKM elastomers at low temperatures, utilizing 2×2D DIC (Paper III)
- An experimental database on the volume growth accompanying tension of elastomers at low temperatures, showing a significant increase in volume growth as the temperature was reduced (Paper III)
- A novel constitutive model to include the temperature dependent volume growth in tension, implemented as a user defined material model for commercial finite element software (Paper III)

An accurate description of the volumetric response of elastomeric materials can be of great importance to capture the large deformation behaviour of such materials in finite element simulations. From the experimental database, it is clear that the traditional procedure of defining the volumetric response of particle-filled elastomer materials from experimental tests dominated by compressive hydrostatic stresses is insufficient for general constitutive modelling, due to the possibility of matrix-particle decohesion in other deformation modes. The effect, and hence the importance, of such decohesion is seen to increase significantly as the temperature is reduced for all tested materials.

7 SUGGESTIONS FOR FURTHER WORK

The research performed within this project gives some ideas for further work, presented in the following bullet-points:

- The reduced failure strain at elevated temperatures observed in Paper I should be studied further to understand its origin and to include it in numerical simulations.

- The confined axial compression tests should be conducted at a range of temperatures to obtain a database on the volumetric response for compressive hydrostatic stresses for different temperature levels. However, this is a challenging task since the thermal expansion of both test sample and experimental apparatus must be accounted for in an accurate manner to meet the tight tolerances of the set-up.

- The in situ SEM investigation should also be performed at a variety of sample temperatures. This could give an increased understanding of the low temperature volumetric behaviour in uniaxial tension found in Paper III. The sample temperature could be altered in similar manners as done for in situ SEM of metallic materials by Karlsen et. al [89].

- Cyclic in situ SEM, studying the samples continuously during deformation could provide an increased understanding of the matrix-particle decohesion behaviour and gain more insight into the observed hysteresis phenomenon. Possibly, image correlation techniques can be applied to a series of micrographs captured during deformation to get an indication of the local strain fields near particle inclusions.

- Other deformation modes than uniaxial tension and confined axial compression should be investigated experimentally to gain increased understanding of the behaviour of the tested materials. While uniaxial compression is experimentally difficult to perform for large deformations, biaxial and planar tension tests could potentially yield interesting results.

- Predictions from the constitutive model suggested in Paper III should be compared to experimental data for elastomeric materials in combined loading modes and at different strain rates to test its generality.

8 REFERENCES

[1] ISO, 10423:2009 Petroleum and natural gas industries – Drilling and production equipment – Wellhead and christmas tree equipment, 2009.

[2] Elastomer Engineering Guide, James Walker, Downloaded from: https://www.jameswalker.biz/de/pdf_docs/148-elastomer-engineering-guide on February 26, 2014.

[3] A. Ciesielski, An Introduction to Rubber Technology, Smithers Rapra Technology, 1999.

[4] P.G. de Gennes, Reptation of a Polymer Chain in the Presence of Fixed Obstacles, The Journal of Chemical Physics. 55 (1971) 572.

[5] M. Doi, S.F. Edwards, The Theory of Polymer Dynamics, Oxford university press, 1986.

[6] P.G. Santangelo, C.M. Roland, Chain Ends and the Mullins Effect in Rubber, Rubber Chemistry and Technology. 65 (1992) 965–972.

[7] M.S. Green, A. V Tobolsky, A New Approach to the Theory of Relaxing Polymeric Media, The Journal of Chemical Physics. 14 (1946).

[8] L.R.G. Treloar, The physics of rubber elasticity, Oxford university press, 1975.

[9] P.W. Bridgman, The Compression of Sixty-One Solid Substances to 25,000 kg/cm2 Determined by a New Rapid Method, Proceedings of the American Academy of Arts and Sciences. 76 (1945) 9–24.

[10] L.A. Wood, G.M. Martin, Compressibility of Natural Rubber at Pressures Below 500 KG/CM2, Rubber Chemistry and Technology. 37 (1964) 850–865.

[11] G.L. Bradley, P.C. Chang, G.B. McKenna, Rubber modeling using uniaxial test data, Journal of Applied Polymer Science. 81 (2001) 837–848.

[12] A.N. Gent, B. Park, Failure processes in elastomers at or near a rigid spherical inclusion, Journal of Materials Science. 19 (1984) 1947–1956.

[13] K. Cho, A.N. Gent, P.S. Lam, Internal fracture in an elastomer containing a rigid inclusion, Journal of Materials Science. 22 (1987) 2899–2905.

[14] A.. Gent, P.. Lindley, Internal Rupture of Bonded Rubber Cylinders in Tension, Proceedings of the Royal Society A: Mathematical, Physical and Engineering Sciences. 249 (1959) 195–205.

[15] W.L. Holt, A.T. McPherson, Change of volume of rubber on stretching : effets of time, elongation and temperature, Journal of Research for the National Bureau of Standards. 17 (1936) 657–687.

[16] H.C. Jones, H.A. Yiengst, Dilatometer Studies of Pigment-Rubber Systems, Rubber Chemistry and Technology. 14 (1941) 113–124.

[17] R. Shuttleworth, Volume change measurements in the study of rubber-filler interactions, European Polymer Journal. 4 (1968) 31–38.

[18] R.W. Penn, Volume Changes Accompanying the Extension of Rubber, Transactions of The Society of Rheology. 14 (1970) 509.

[19] J.B. Le Cam, E. Toussaint, Volume Variation in Stretched Natural Rubber: Competition between Cavitation and Stress-Induced Crystallization, Macromolecules. 41 (2008) 7579–7583.

[20] J. de Crevoisier, G. Besnard, Y. Merckel, H. Zhang, F. Vion-Loisel, J. Caillard, et al., Volume

changes in a filled elastomer studied via digital image correlation, Polymer Testing. 31 (2012) 663–670.

[21] S. Cantournet, K. Layouni, L. Laiarinandrasana, R. Piques, Experimental investigation and modelling of compressibility induced by damage in carbon black-reinforced natural rubber, Comptes Rendus Mécanique. 342 (2014) 299–310.

[22] S. V. Hainsworth, An environmental scanning electron microscopy investigation of fatigue crack initiation and propagation in elastomers, Polymer Testing. 26 (2007) 60–70.

[23] E. Bayraktar, N. Isac, K. Bessri, C. Bathias, Damage mechanisms in natural (NR) and synthetic rubber (SBR): Nucleation, growth and instability of the cavitation, Fatigue and Fracture of Engineering Materials and Structures. 31 (2008) 184–196.

[24] S. Beurrot, B. Huneau, E. Verron, In situ SEM study of fatigue crack growth mechanism in carbon black-filled natural rubber, Journal of Applied Polymer Science. 117 (2010) 1260–1269.

[25] J.-B. Le Cam, B. Huneau, E. Verron, Fatigue damage in carbon black filled natural rubber under uni- and multiaxial loading conditions, International Journal of Fatigue. 52 (2013) 82–94.

[26] B. Huneau, I. Masquelier, Y. Marco, V. Le Saux, S. Noizet, C. Schiel, et al., Initiation mechanisms of fatigue cracks in carbon black filled natural rubber, Constitutive Models for Rubber IX. (2015) 395–401.

[27] A.D.D. Drozdov, J. Christiansen, Thermo-viscoplasticity of carbon black-reinforced thermoplastic elastomers, International Journal of Solids and Structures. 46 (2009) 2298–2308.

[28] A. Lion, On the large deformation behaviour of reinforced rubber at different temperatures, Journal of the Mechanics and Physics of Solids. 45 (1997) 1805–1834.

[29] A.F.M.S. Amin, A. Lion, P. Höfer, Effect of temperature history on the mechanical behaviour of a filler-reinforced NR/BR blend: Literature review and critical experiments, ZAMM Zeitschrift Fur Angewandte Mathematik Und Mechanik. 90 (2010) 347–369.

[30] J.M. Martinez, A. Boukamel, S. Méo, S. Lejeunes, Statistical approach for a hyper-visco-plastic model for filled rubber: Experimental characterization and numerical modeling, European Journal of Mechanics - A/Solids. 30 (2011) 1028–1039.

[31] J.A. Shaw, A.S. Jones, A.S. Wineman, Chemorheological response of elastomers at elevated temperatures: Experiments and simulations, Journal of the Mechanics and Physics of Solids. 53 (2005) 2758–2793.

[32] T. Rey, G. Chagnon, J.-B. Le Cam, D. Favier, Influence of the temperature on the mechanical behaviour of filled and unfilled silicone rubbers, Polymer Testing. 32 (2013) 492–501.

[33] F. Rouillard, P. Heuillet, B. Omnes, Viscoelastic characterization at low temperature on an HNBR compound for sealing applications, in: Constitutive Models for Rubber VIII - Proceedings of the 8th European Conference on Constitutive Models for Rubbers, ECCMR 2013, 2013: pp. 591–594.

[34] A.S. Khan, M. Baig, S. Hamid, H. Zhang, Thermo-mechanical large deformation responses of Hydrogenated Nitrile Butadiene Rubber (HNBR): Experimental results, International Journal of Solids and Structures. 47 (2010) 2653–2659.

[35] H. Laurent, G. Rio, A. Vandenbroucke, N. Aït Hocine, H.L.G. Rio, A.V.N. Aït, Experimental and numerical study on the temperature-dependent behavior of a fluoro-elastomer, Mechanics of Time-Dependent Materials. 18 (2014) 721–742.

[36] S.K. Kurlyand, Low-Temperature Behaviour of Elastomers, CRC Press, 2007.

[37] T. Belytschko, W.K. Liu, B. Moran, K. Elkhodary, Nonlinear Finite Elements for Continua and Structures, Wiley, 2014.

[38] G.A. Holzapfel, Nonlinear Solid Mechanics: A Continuum Approach for Engineering, John Wiley & Sons, 2000.

[39] J. Bergström, Mechanics of Solid Polymers, Elsevier, 2015.

[40] W. Ehlers, G. Eipper, The simple tension problem at large volumetric strains computed from finite hyperelastic material laws, Acta Mechanica. 130 (1998) 17–27.

[41] C. Sansour, On the physical assumptions underlying the volumetric-isochoric split and the case of anisotropy, European Journal of Mechanics, A/Solids. 27 (2008) 28–39.

[42] J.C. Simo, K.S. Pister, Remarks on rate constitutive equations for finite deformation problems: computational implications, Computer Methods in Applied Mechanics and Engineering. 46 (1984) 201–215.

[43] J.E. Bischoff, E.M. Arruda, K. Grosh, A new constitutive model for the compressibility of elastomers at finite deformations, Rubber Chemistry and Technology. 74 (2001) 541–559.

[44] M.C. Boyce, E.M. Arruda, Constitutive Models of Rubber Elasticity: A Review, Rubber Chemistry and Technology. 73 (2000) 504–523.

[45] R.S. Rivlin, D.W. Saunders, Large Elastic Deformations of Isotropic Materials. VII. Experiments on the Deformation of Rubber, Philosophical Transactions of the Royal Society of London. Series A, Mathematical and Physical Sciences. 243 (1951) 251–288.

[46] R.S. Rivlin, Large Elastic Deformations of Isotropic Materials. I. Fundamental Concepts, Philosophical Transactions of the Royal Society A: Mathematical, Physical and Engineering Sciences. 240 (1948) 459–490.

[47] M. Mooney, A theory of large elastic deformation, Journal of Applied Physics. 11 (1940) 582–592.

[48] O.H. Yeoh, Characterization of Elastic Properties of Carbon-Black-Filled Rubber Vulcanizates, Rubber Chemistry and Technology. 63 (1990) 792–805.

[49] R.W. Ogden, Large Deformation Isotropic Elasticity—On the Correlation of Theory and Experiment for Incompressible Rubberlike Solids, Rubber Chemistry and Technology. 46 (1973) 398–416.

[50] W. Kuhn, F. Grün, Beziehungen zwischen elastischen Konstanten und Dehnungsdoppelbrechung hochelastischer Stoffe, Kolloid-Zeitschrift. 101 (1942) 248–271.

[51] M.C. Wang, E. Guth, Statistical theory of networks of non-gaussian flexible chains, The Journal of Chemical Physics. 20 (1952) 1144–1157.

[52] P.J. Flory, J. Rehner Jr, Statistical mechanics of cross-linked polymer networks I. Rubberlike elasticity, The Journal of Chemical Physics. 11 (1943) 512–520.

[53] E.M. Arruda, M.C. Boyce, A three-dimensional constitutive model for the large stretch behavior of rubber elastic materials, Journal of the Mechanics and Physics of Solids. 41 (1993) 389–412.

[54] R. Jedynak, Approximation of the inverse Langevin function revisited, Rheologica Acta. 54 (2015) 29–39.

[55] S. Doll, K. Schweizerhof, On the Development of Volumetric Strain Energy Functions, Journal of Applied Mechanics. 67 (1999) 17–21.

[56] C.O. Horgan, J.G. Murphy, On the volumetric part of strain-energy functions used in the

constitutive modeling of slightly compressible solid rubbers, International Journal of Solids and Structures. 46 (2009) 3078–3085.

[57] T. Sussman, K.-J. Bathe, A finite element formulation for nonlinear incompressible elastic and inelastic analysis, Computers and Structures. 26 (1987) 357–409.

[58] T.Y.P. Chang, A.F. Saleeb, G. Li, Large strain analysis of rubber-like materials based on a perturbed Lagrangian variational principle, Computational Mechanics. 8 (1991) 221–233.

[59] Abaqus Theory Guide 6.13, Dassault Systèmes, 2013.

[60] J.C. Simo, C. Miehe, Associative coupled thermoplasticity at finite strains: Formulation, numerical analysis and implementation, Computer Methods in Applied Mechanics and Engineering. 98 (1992) 41–104.

[61] M. Kaliske, H. Rothert, On the finite element implementation of rubber-like materials at finite strains, Engineering Computations. 14 (1997) 216–232.

[62] H. Hencky, The Elastic Behavior of Vulcanized Rubber, Rubber Chemistry and Technology. 6 (1933) 217–224.

[63] J.C. Simo, R.L. Taylor, K.S. Pister, Variational and projection methods for the volume constraint in finite deformation elasto-plasticity, Computer Methods in Applied Mechanics and Engineering. 51 (1985) 177–208.

[64] L. Anand, A constitutive model for compressible elastomeric solids, Computational Mechanics. 18 (1996) 339–355.

[65] M. Polanco-Loria, A.H. Clausen, T. Berstad, O.S. Hopperstad, Constitutive model for thermoplastics with structural applications, International Journal of Impact Engineering. 37 (2010) 1207–1219.

[66] G.A. Holzapfel, J.C. Simo, A new viscoelastic constitutive model for continuous media at finite thermomechanical changes, International Journal of Solids and Structures. 33 (1996) 3019–3034.

[67] A. Lion, A constitutive model for carbon black filled rubber: Experimental investigations and mathematical representation, Continuum Mechanics and Thermodynamics. 8 (1996) 153–169.

[68] J.S. Bergström, M.C. Boyce, Constitutive modeling of the large strain time-dependent behavior of elastomers, Journal of the Mechanics and Physics of Solids. 46 (1998) 931–954.

[69] C. Miehe, S. Göktepe, A micro–macro approach to rubber-like materials. Part II: The micro-sphere model of finite rubber viscoelasticity, Journal of the Mechanics and Physics of Solids. 53 (2005) 2231–2258.

[70] G. Ayoub, F. Zaïri, M. Naït-Abdelaziz, J.M. Gloaguen, G. Kridli, A visco-hyperelastic damage model for cyclic stress-softening, hysteresis and permanent set in rubber using the network alteration theory, International Journal of Plasticity. 54 (2014) 19–33.

[71] J. Lubliner, A model of rubber viscoelasticity, Mechanics Research Communications. 12 (1985) 93–99.

[72] A.D. Drozdov, A constitutive model for nonlinear viscoelastic media, International Journal of Solids and Structures. 34 (1997) 2685–2707.

[73] S. Reese, A micromechanically motivated material model for the thermo-viscoelastic material behaviour of rubber-like polymers, International Journal of Plasticity. 19 (2003) 909–940.

[74] Livermore Software Technology Corporation (LSTC), LS-DYNA keyword user's manual, version R8.0, vols 1 and 2, 2016.

[75] S.C.H. Lu, K.S. Pister, Decomposition of deformation and representation of the free energy function for isotropic thermoelastic solids, International Journal of Solids and Structures. 11 (1975) 927–934.

[76] G.A. Holzapfel, J.C. Simo, Entropy elasticity of isotropic rubber-like solids at finite strains, Computer Methods in Applied Mechanics and Engineering. 132 (1996) 17–44.

[77] C. Ovalle Rodas, F. Zaïri, M. Naït-Abdelaziz, P. Charrier, Temperature and filler effects on the relaxed response of filled rubbers: Experimental observations on a carbon-filled SBR and constitutive modeling, International Journal of Solids and Structures. 58 (2015) 309–321.

[78] J.S. Bergström, L.B. Hilbert, A constitutive model for predicting the large deformation thermomechanical behavior of fluoropolymers, Mechanics of Materials. 37 (2005) 899–913.

[79] ISO, 815-1:2014 Rubber, vulcanized or thermoplastic – Determination of compression set – Part 1: At ambient or elevated temperatures, 2014.

[80] C. Harris, M. Stephens, A combined corner and edge detector, in: Alvey Vision Conference, 1988: p. 50.

[81] B. Pan, K. Qian, H. Xie, A. Asundi, Two-dimensional digital image correlation for in-plane displacement and strain measurement: a review, Measurement Science and Technology. 20 (2009) 1–17.

[82] E. Fagerholt, T. Børvik, O.S. Hopperstad, Measuring discontinuous displacement fields in cracked specimens using digital image correlation with mesh adaptation and crack-path optimization, Optics and Lasers in Engineering. 51 (2013) 299–310.

[83] J. Johnsen, F. Grytten, O.S. Hopperstad, A.H. Clausen, Experimental set-up for determination of the large-strain tensile behaviour of polymers at low temperatures, Polymer Testing. 53 (2016) 305–313.

[84] S. van der Walt, J.L. Schönberger, J. Nunez-Iglesias, F. Boulogne, J.D. Warner, N. Yager, et al., scikit-image: image processing in Python., PeerJ. 2 (2014) e453.

[85] N. Otsu, Threshold selection method from gray-level histograms, IEEE Trans Syst Man Cybern. SMC-9 (1979) 62–66.

[86] Abaqus, 6.13-1, Dassault Systèmes, 2013.

[87] LS-DYNA, R8.0, Livermore Software Technology Corporation (LSTC), 2015.

[88] LS-OPT, 5.2.1, Livermore Software Technology Corporation (LSTC), 2016.

[89] M. Karlsen, Ø. Grong, M. Søfferud, J. Hjelen, G. Rørvik, R. Chiron, Scanning electron microscopy/electron backscatter diffraction - Based observations of martensite variant selection and slip plane activity in supermartensitic stainless steels during plastic deformation at elevated, ambient, and subzero temperatures, Metallurgical and Materials Transactions A: Physical Metallurgy and Materials Science. 40 (2009) 310–320.

Part II

Appended papers

Paper I

Arne Ilseng, Bjørn H. Skallerud, Arild H. Clausen

Tension behaviour of HNBR and FKM elastomers for a wide range of temperatures

Polymer Testing 49 (2016), pp. 128-136

Paper I

Tension behaviour of HNBR and FKM elastomers for a wide range of temperatures

Arne Ilseng[a,b,*], Bjørn H. Skallerud[a], Arild H. Clausen[a]

[a] *Department of Structural Engineering, NTNU, Norwegian University of Science and Technology, 7491 Trondheim, Norway*
[b] *Aker Solutions AS, 3408 Tranby, Norway*

Abstract

This article presents uniaxial tension tests of three different elastomer compounds commonly applied as seal materials in the oil and gas industry. The tests were performed at five different temperatures, ranging from −20 to 150 °C. Optical measurements were used to ensure high quality stress-strain data. The material samples were exposed to a cyclic deformation history, enabling the viscoelastic behaviour to be explored. A considerable effect of temperature changes was found, with a pronounced increase of stiffness and viscosity for the lowest temperatures. A dip in the stress-strain curve was seen for one of the hydrogenated nitrile butadiene rubbers tested at low temperatures. Matrix-particle debonding simulations qualitatively described this stress dip. For the tests performed at the highest temperatures, a considerable number encountered material failure.

Keywords: Elastomers, uniaxial tension, temperature effects, relaxation, failure

1. Introduction

Failure of elastomer seals during qualification testing [1] is an expensive issue for the subsea oil and gas industry. An increased use of numerical calculations, like finite element simulations, during the design of such seals could possibly reduce the number of failed qualification tests and thereby lower costs. To enable predictive results from numerical simulations, constitutive models that capture the essential physics of the material at hand must be employed. The accuracy of the numerical predictions is also strongly dependent on the quality of the experimental tests providing input data to the material model.

Elastomer seals that are used in subsea equipment undergo severe service conditions including high pressures, exposure to production fluids, large deformations, and varying temperatures. In addition to the mechanical features, thermal characteristics like specific heat capacity, thermal conductivity, and thermal expansion are therefore important material properties. The scope of this work is to obtain low strain-rate viscoelastic material data for the large strain behaviour of elastomers at a wide spectre of temperatures, ranging between −20 and 150 °C. Two material

*arne.ilseng@ntnu.no

groups commonly used for sealing purposes in the oil and gas industry; hydrogenated nitrile butadiene rubber (HNBR) and fluoroelastomer (FKM), are addressed herein. HNBR is known as the workhorse in the oil and gas industry due to its good fluid resistance combined with appropriate mechanical properties. FKM compounds are generally more expensive, but inhabit enhanced temperature capabilities for the high temperature regime and an improved compatibility with certain fluids.

Over the years, numerous studies have dealt with different aspects of elastomeric behaviour relevant for sealing application modelling (e.g. [2–10]). However, the number of investigations concerned with the effects of temperature on elastomers mechanical behaviour is limited [11–19]. The general findings though, are that the elastic stiffness and the viscous effects are enhanced as temperature is reduced. A contrary to the latter aspect was shown by Shaw et al. [15] for a natural rubber above its chemorheological temperature, i.e. the temperature above which chain scission is accelerated, where chemical changes ensured a significantly enhanced stress relaxation as the temperature was increased.

For the temperature dependent mechanical behaviour of HNBR and FKM materials specifically, only a few studies could be found in the literature. Rouillard et al. [17] tested an HNBR compound in compression at temperatures between -34 and 80 °C to obtain data for numerical modelling of seals. Khan et al. [18] tested two HNBR compounds in compression at a variety of strain rates and for temperatures ranging from ambient temperature and up to 176 °C. In this temperature range, they found the strain-rate sensitivity to be more pronounced than the temperature effects. For an FKM compound, tension and compression tests at temperatures in the range from -8 to 100 °C were reported by Laurent et al. [19], for the purpose of finite element modelling. They used an optical extensometer to monitor the longitudinal deformation during the tension tests, but only nominal values were reported.

For constitutive modelling of the thermomechanical behaviour of elastomers at large deformations, true stress-strain data obtained by local deformation measurements are of outmost importance. To the best of the authors knowledge, no study presenting such data for HNBR or FKM materials is available in the literature. Nevertheless, Ilseng et al. [9, 10] have recently presented tension and volumetric compression data at room temperature for the HNBR and FKM materials addressed herein. Elastomeric materials are mainly tested in uniaxial tension or compression. In large deformation uniaxial compression tests, frictional forces cause non-homogeneous deformations, making it hard to obtain the correct material behaviour. Tension experiments on the other hand, are far easier to interpret.

The scope of this work is to provide experimental data to be used for constitutive modelling of HNBR and FKM compounds commonly used in sealing applications. True stress-strain data are obtained with local measurements of the deformation field. The study extends the HNBR data available in the literature to cyclic tension, and expands the data for FKM materials to include the

temperature range from −20 to 150 °C. For the high temperature tests, a summary of encountered material failure is presented. In addition, measured values for the heat capacity and thermal conductivity at different temperatures are included for one HNBR and one FKM compound.

The paper is organized as follows: in the subsequent section, the materials and methods used for the experimental work are presented. Next, the obtained experimental results are presented and discussed in Section 3, while some concluding remarks are given in Section 4.

2. Materials and methods

2.1. Materials

Dumbbell shaped specimens of commercially available compounds were ordered from companies supplying seals to the oil and gas industry. All specimens were die stamped from 2 mm thick sheets. One HNBR compound was delivered with a geometry according to ISO 37 type 1 [20], while another HNBR compound and one FKM compound had dimensions in line with ISO 37 type 2. The different materials, their dumbbell geometry, the measured pre-testing density, and the temperature range and hardness values provided by the suppliers are listed in Table 1. The lower end of the temperature range coincides with the temperature at which the material has fully transitioned into the glassy region. The density of the materials was measured both before and after testing; however, no significant density change could be observed. Based on the stated material properties, comparable results would be expected for the two HNBR compounds.

Table 1: Tested materials, their geometries and properties

Material	Geometry	Density	Temperature range	Hardness
HNBR1	ISO 37 - Type 1	1.29 g/cm^3	−35 to 150 °C	86 shore A
HNBR2	ISO 37 - Type 2	1.19 g/cm^3	−29 to 160 °C	89 IRHD
FKM	ISO 37 - Type 2	1.77 g/cm^3	−40 to 200 °C	89 IRHD

2.2. Deformation history

The experimental program was performed using a Zwick/Roell testing machine with a 30 kN load cell and a Zwick WT160 temperature chamber. Liquid nitrogen was connected to the chamber to allow testing below room temperature, while electrical resistance was used for heating. The three materials were tested at five different temperature levels: −20, 0, 23, 85, and 150 °C. Two consecutive tests were run for each combination of material and temperature, giving 30 tests in total.

Since elastomer seals in the subsea oil and gas industry are often exposed to loading cycles, either due to temperature variations, pressure variations, or due to dynamic sealing conditions, a cyclic deformation history was applied. All specimens were exposed to seven loading cycles in total, as illustrated for the HNBR1 material in Figure 1. In each cycle, the sample was stretched

40 mm from its initial length with a deformation rate of 1 mm/s, and unloaded at the same rate of deformation until zero force was obtained in the load cell. Due to the viscous effects in the materials, zero force was measured before the crosshead displacement was back to zero, leading to an effective deformation of less than 40 mm for all cycles but the first one. To get a quantitative measure of the viscous behaviour of the materials, deformation was kept constant at 40 mm for 30 minutes in the sixth cycle as a relaxation test. The maximum displacement was reduced to 30 mm in most high temperature tests, see Section 3.1

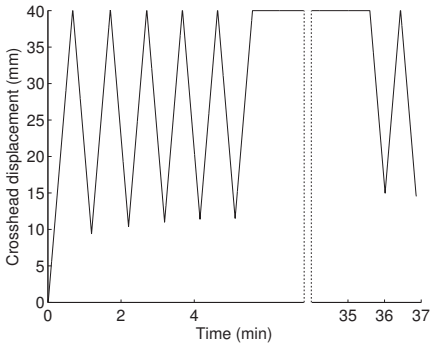

Figure 1: Crosshead displacement for test on HNBR1 at room temperature.

2.3. Determination of true stress-strain curves

The true stress σ obtained in the gauge section of a uniaxial tension test is defined as

$$\sigma = F/A \tag{1}$$

where F is the force applied to the specimen, and A is the current cross-sectional area. The area A can be found from the reference area A_0, being the area measured prior to testing, by the relation

$$A = \lambda_2 \lambda_3 A_0 \tag{2}$$

where λ_2 and λ_3 are the two transverse stretch ratios. When testing at artificial temperatures though, the use of a temperature chamber will often limit the possibility to measure both transverse stretch ratios during deformation. In such a case, an assumption of transverse isotropic material behaviour, i.e. $\lambda_2 = \lambda_3$, can be used to estimate the current cross-sectional area by

$$A = (\lambda_2)^2 A_0 \tag{3}$$

Alternatively, a presumption of material incompressibility can be applied, i.e. the product $\lambda_2\lambda_3$ is uniquely defined from the longitudinal stretch λ_1 through $\lambda_2\lambda_3 = 1/\lambda_1$. This assumption is commonly used for elastomer materials [2], and the current cross-sectional area can be found by the relation

$$A = A_0/\lambda_1 \tag{4}$$

The use of Equation (3) or (4) would significantly simplify the experimental protocol. To investigate how the assumptions of transverse isotropy and constant volume affect the estimate of the true stress-strain behaviour, a separate set of experiments on all three materials was performed at room temperature. In these tests, an Instron 5944 testing machine with a 2 kN load was used. The specimens were exposed to five deformation cycles in which they were loaded to 40 mm of crosshead displacement, and unloaded until zero force was measured by the load cell. A deformation rate of 1 mm/s was applied.

To enable the calculation of local deformations, a random grey scale speckle pattern was spray-painted in the gauge section of the specimens, and two independent cameras were used to capture frames of both the wide and the narrow surface of the samples. The frames obtained during the fifth cycle of the tests were post-processed with an in-house digital image correlation (DIC) software [21] to calculate all three stretch components, and subsequently the true longitudinal strain. The longitudinal stretch calculated from the two independent cameras differed with less than 0.3 %. The deformation in the gauge section of the specimens was also found to be nearly homogenous.

The different stress estimates were compared by calculating the mean stress response, i.e. an average of the loading and unloading curve, for the fifth cycle. A correct true stress-strain response, employing the current area found with Equation (2), was obtained by use of all three measured stretch components. In Figure 2, this correct true stress-strain response is compared with estimates based on information from one camera only. It can be seen that an assumption of constant volume, leading to Equation (4), gives a very good resemblance of the true stress level for both HNBR compounds, with the estimated stress deviating less than 1 % from the correct stress level. For the FKM compound, on the other hand, the estimated peak stress based on a constant volume assumption is more than 18 % above the correct level. Estimating the current area from a transverse isotropy presumption, as defined by Equation (3), the obtained true stress-strain curves are slightly underestimating the correct ones for all three materials.

In the following sections, the constant volume assumption was applied for the two HNBR compounds, while the FKM material was regarded as transverse isotropic. An exception was made for the first loading of HNBR1 at -20 and 0 °C, where the isotropy assumption was used; this is discussed further in Section 3.3.

2.4. Thermal conditioning

Polymeric materials are in general good thermal insulators, implying that it takes some time to heat or cool the entire sample to the desired test temperature. Finite element analyses were used to estimate the time needed to reach a homogeneous temperature throughout the specimens. Such simulations demand knowledge of the thermal properties of the HNBR and FKM compounds. The thermal conductivity and the specific heat capacity of the HNBR2 and the FKM materials were measured by a laser flash method [22]. Four samples of each material were tested at 25, 50, 100, and 150 °C. Measurements at temperatures lower than the ambient level could not be performed

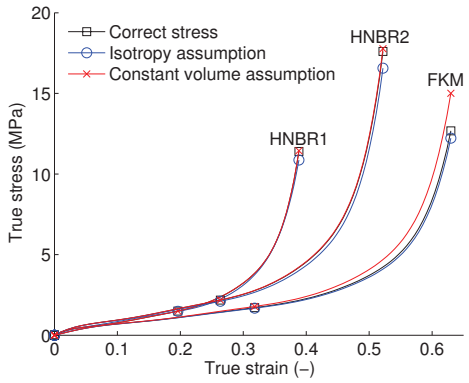

Figure 2: Comparison of true stress-strain curves obtained in three different ways. The mean behaviour of the fifth cycle is shown.

due to limitations in the experimental setup. The results are presented in Figure 3. It appears that the thermal conductivity is rather similar for the two materials, and not very sensitive to temperature. The specific heat capacity differs more, and increases with temperature.

To estimate the coefficient of heat convection between the elastomer compounds and air, a thin rectangular specimen of each material was heated in boiling water, and the temperature decay in room temperature was measured using an infrared thermometer. An air-to-elastomer heat convection parameter of around 15 $\mathrm{W/m^2K}$ was found for the two HNBR compounds, while a value of 23 $\mathrm{W/m^2K}$ was determined for the FKM material.

Table 2 shows the conservative thermal data that were used in the numerical simulations to obtain an upper bound estimate of the time needed to heat the specimens. The simulations were carried out using the commercial finite element software Abaqus [23], with a 3D model of the material sample meshed by 1200 elements. The thermal boundary condition was defined as a surface film on the exterior of the specimen. Starting with an initial sample temperature of 23 °C and a chamber temperature of 150 °C, the simulation showed that 15 minutes should be sufficient to heat the samples. For convenience during the experimental campaign, the specimen for test $n+1$ was inserted in the temperature chamber at the start of test n, leading to approximately 40 minutes of thermal conditioning before the specimens were mounted in the test machine.

An important aspect to keep in mind when studying the effect of temperature on inelastic materials is that self-heating might take place during deformation of the samples. By use of an infrared camera, the evolution of temperature during the deformation cycles at room temperature was measured. The peak temperature in the gauge section was found to occur at maximum deformation in the first cycle, with a temperature increase of approximately 4 °C for the HNBR2 material, and about 2 °C for the HNBR1 and the FKM materials. It is presumed that the level of self-heating is somewhat larger at low temperatures, since the plastic work would increase while the specific heat capacity shows a decreasing tendency with reduced temperatures. Nevertheless,

this is considered outside the scope of this work, and the effect of self-heating during deformation is neglected in the further discussion.

Table 2: Material data used for an upper bound estimate of the thermal conditioning.

Thermal conductivity	Specific heat capacity	Density	Air to elastomer convection
0.4 W/mK	2000 J/kgK	1000 kg/m^3	14 W/m^{2}K

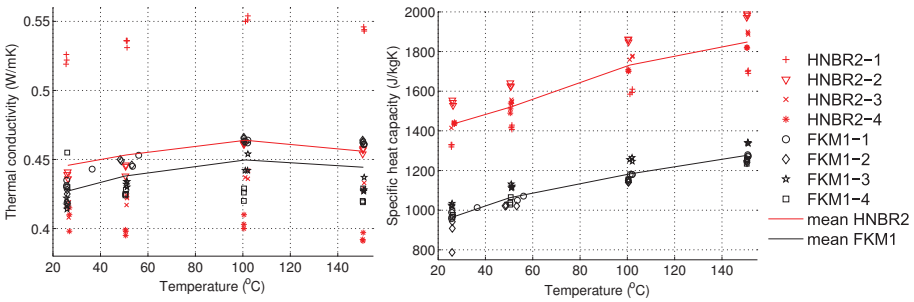

(a) (b)

Figure 3: Thermal properties of HNBR2 and FKM material, measured by a laser flash method (a) thermal conductivity and (b) specific heat capacity.

2.5. Instrumentation

Since there was a single window in the heating chamber, the deformation was measured in the wide surface of the specimens only, using a camera to capture pictures of the gauge section at a frame rate of 7 Hz. To enable optical measurements, a grey scale speckle pattern was spray-painted in the gauge section of the specimens. At low temperatures, cracks formed in the applied paint during deformation, causing difficulties for the DIC software. The pictures of all tests were therefore post-processed by use of an edge trace routine written in MATLAB [24]. In the edge trace routine, the gradient of the grey-scale level in each frame was used to determine both the edge of the specimen and the edge of the painted section. The transverse and longitudinal strains, respectively, were thereafter calculated by looping through all the frames. An example frame from a −20 °C test on an HNBR1 compound is shown in Figure 4a, while the grey level gradient for one vertical line of pixels in the frame is shown in Figure 4b. The edge trace routine was verified at room temperature by comparing the results with those obtained by an in-house DIC software [21]. A difference in the maximum longitudinal strain of less than 0.5 % was found between the two methods.

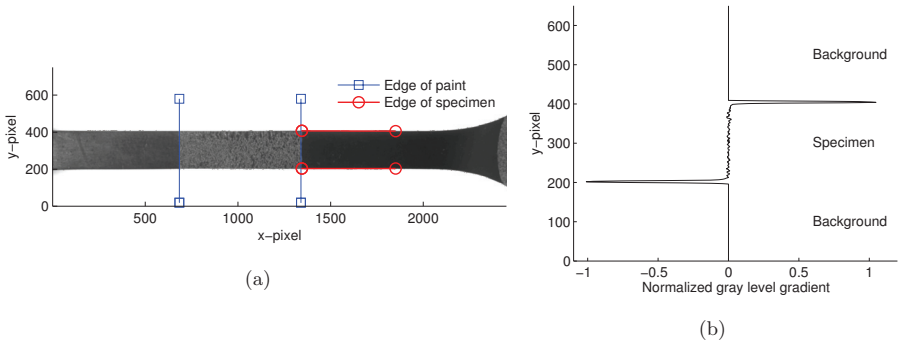

Figure 4: Example of edge tracing routine for HNBR1 material at −20 °C, (a) example frame and (b) grey level gradient for x-pixel line 1500.

3. Results and discussion

3.1. Preliminaries

In this section, the results obtained from the tension tests at different temperatures are presented and discussed. First, the entire test consisting of seven cycles is addressed in Section 3.2 for all materials and temperatures. Thereafter, a closer look is taken at the first and fifth cycle in Section 3.3 and 3.4, respectively. The sixth cycle, containing the relaxation process, follows in Section 3.5.

Due to material failure at high temperatures, fifth cycle and relaxation results could not be obtained for the FKM compound at 150 °C. In addition, the maximum deformation had to be reduced to 30 mm for the tests on HNBR1 and FKM at 85 °C, and for all materials at 150 °C. All the tests where material failure occurred are presented in Section 3.6.

The curves to be presented in this section were obtained from one of the two tests for each combination of temperature and material. Although not shown herein, the duplicate tests revealed consistency of the presented results.

3.2. Cyclic data

The force-displacement data as obtained from the test machine are presented in Figure 5 for each combination of material and temperature. In general, it can be seen that the main part of the first onloading curve is close to linear, while a more pronounced s-shape can be found in the loading part of the subsequent cycles. The unloading follows a completely different path, especially at low temperatures. The amount of global deformation at the onset of the second cycle is observed to increase significantly as the temperature is reduced. It can be noted that for the HNBR2 material tested at −20 °C, the cycle deformation is less than 10 mm in the fifth cycle, and only a few millimetres in the seventh cycle. In addition to the viscous effects observed through the hysteresis loop, some Mullins softening [25] can be seen for all tests. For the higher temperatures, nearly all

softening happens in the first few cycles, leading to a nearly converged behaviour in the fifth cycle. On the other hand, there is a distinguishable softening occurring also between the fourth and fifth deformation cycle at the lower temperatures. During the first loading of the HNBR1 material at -20 and 0 °C, the force level can be seen to level out and drop slightly after approximately 30 mm of crosshead displacement. This phenomenon is discussed further in the following subsection.

3.3. First loading

Applying the methodology established in Section 2.3, the true stress-strain response for the loading part of the first cycle is shown in Figure 6, where each of the three sub-figures addresses the five temperature levels for one material. The general impression is that the stiffness is reduced as the temperature is increased. In addition, it can be noted that the change of stiffness per degree is lower at elevated temperatures. Comparing the three materials, a pronounced difference in peak stress is observed, especially for the cold temperatures. The HNBR2 has clearly the highest peak stress at -20 °C being nearly 70 MPa, compared to hardly 40 MPa for the FKM material and less than 25 MPa for the HNBR1 material.

During the first loading of the HNBR1 material, a flattening and dip in the stress-strain response was observed for the 0 and -20 °C tests respectively. This low temperature behaviour has already been reported by Rouillard et al. [17], who tested an HNBR compound in uniaxial compression at -34 °C. They suggested that this dip occured due to an elastic-plastic material response. In the present tests however, there is no indication that the HNBR1 material behaves more plastically at low temperatures than the HNBR2 and the FKM compunds, although no stress dip can be seen for those materials. What could be found in the tests, though, was that the rate of transverse deformation, measured on the wide surface of the specimens, dropped to zero at the onset of the stress-dip. This indicates, assuming that the rate of deformation in the thickness direction does not increase correspondingly, that a significant volumetric expansion accompanies the stress-dip. The volume of an elastomer can change in two ways, either by a reconfiguration of the polymer chains, or by an introduction of cavities in the material. The latter, through a matrix-particle debonding process, is expected to be the explanation for the volume increase seen in these tests.

The commercial finite element software Abaqus [23] was used in a generic study of matrix-particle debonding during uniaxial tension. Filler particles in elastomers are known to cluster in grape-shaped structures [8], but for simplicity it was assumed that the global behaviour can be represented by a cylinder of matrix material with a spherical particle embedded in its centre. By use of this simplification, an efficient axisymmetric finite element model could be defined. The model is shown, both in its initial configuration and after debonding has taken place, in Figure 7a. The cell boundaries were constrained to remain straight throughout the deformation, and a Multi Point Constraint user subroutine was defined in Abaqus to ensure a deformation mode of generalized tension. The procedure used was first described by Faleskog et al. [26] for plane strain, and then formulated for axisymmetric models by Kim et al. [27]. Since the HNBR1 material is

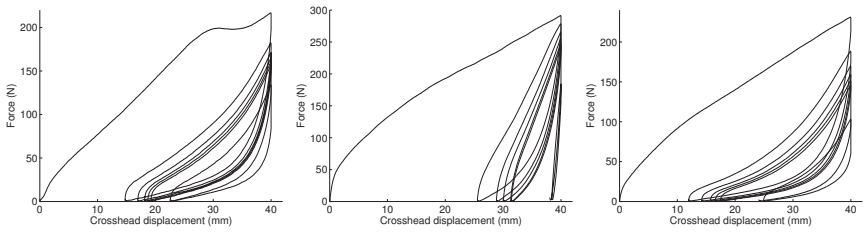

(a) HNBR1 at −20 °C (b) HNBR2 at −20 °C (c) FKM at −20 °C

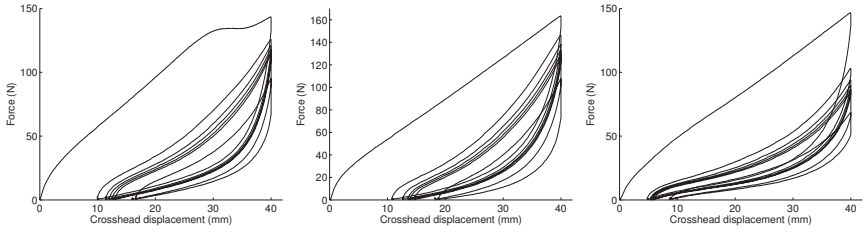

(d) HNBR1 at 0 °C (e) HNBR2 at 0 °C (f) FKM at 0 °C

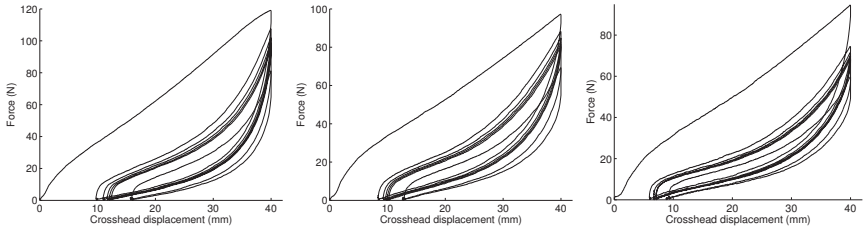

(g) HNBR1 at 23 °C (h) HNBR2 at 23 °C (i) FKM at 23 °C

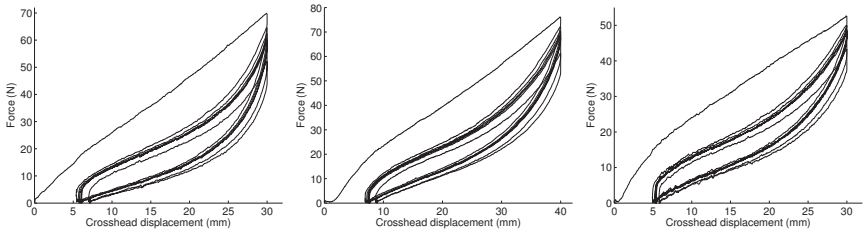

(j) HNBR1 at 85 °C (k) HNBR2 at 85 °C (l) FKM at 85 °C

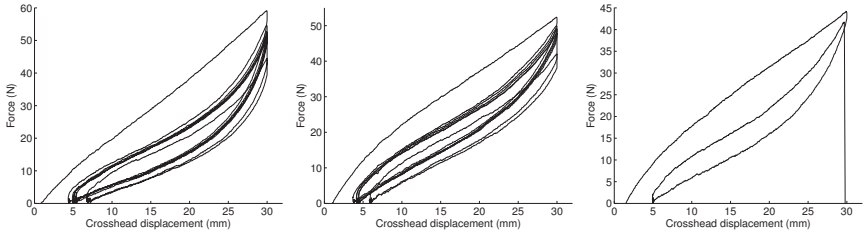

(m) HNBR1 at 150 °C (n) HNBR2 at 150 °C (o) FKM at 150 °C

Figure 5: Raw machine data for all combinations of material and temperature.

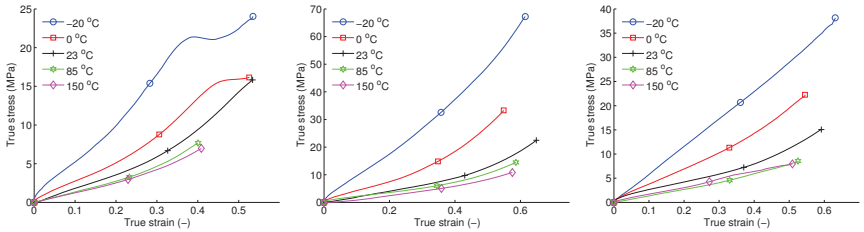

Figure 6: True stress-strain curves during first loading at different temperatures for the (a) HNBR1, (b) HNBR2, and (c) FKM materials.

a commercial product, the exact amount of filler particles was not known, and the centre sphere was simply assumed to take up 15 percent of the total volume. The matrix material was modelled as an incompressible hyperelastic neo-Hookean material with a shear modulus of 2 MPa, while the filler particle was modelled as linear elastic with a modulus a hundred times larger than the matrix material and a Poissons ratio of 0.3 [8]. Debonding between the matrix and the particle initiated at the pole of the particle, i.e. at the rotation axis, and propagated along the interface towards the symmetry axis of the model. A cohesive zone model was used to define the behaviour of the matrix-particle interface, with the damage initiation and evolution being controlled by a bilinear energy-based criterion.

The stress-strain response obtained from the simulations can be seen in Figure 7b. In addition to one curve representing the approximate qualitative behaviour in the −20 °C test, two curves indicating the effect of increased and reduced fracture energy of the cohesive zone are also included in the figure. A configuration with comparatively low fracture energy, corresponding to the red curve in Figure 7b, is likely to occur at low temperatures. It should be noted that the mechanism shown in Figure 7 might also explain the behaviour observed in compression by Rouillard et al. [17]. In that case, the debonding process would start at the symmetry axis and move towards the rotation axis during deformation.

3.4. Fifth cycle

Since the cyclic behaviour is close to converged after the first four cycles, the fifth cycle can be interpreted as the long-term cyclic behaviour. To obtain comparable data for the different materials, the strain of the fifth cycle was calculated using the configuration at the onset of the cycle as the reference state. An eight-order polynomial was then fit to the stress-strain hysteresis loop to get the mean behaviour of the loading unloading loop. The data obtained for all materials and temperatures are presented in Figure 8. All three materials are seen to exhibit a significantly stiffer behaviour at −20 °C compared to the other temperatures. For HNBR1, little difference can be seen in the cycle behaviour between 0 and 85 °C, while further softening is seen when increasing the temperature to 150 °C. The results for HNBR2 show a clear softening as the temperature is

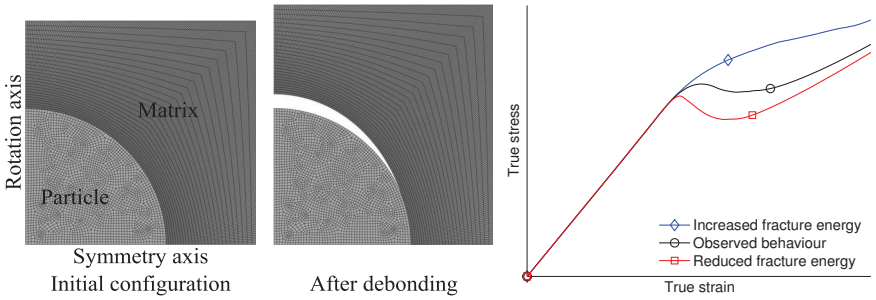

(a) (b)

Figure 7: Finite element results for matrix-particle debonding process. (a) Illustration of the debonding mechanism and (b) the obtained stress-strain data.

increased to 85 °C, but thereafter a slight stiffness increase at large strains for the test performed at 150 °C. In the FKM material, there is little difference between the behaviour at 0 and 23 °C, while the material is slightly stiffer at 85 °C. The 150 °C curve is absent for FKM because these samples fractured during the first or second cycle. The fact that the stiffness of the fifth cycle is increasing at the highest temperatures in the HNBR2 and FKM materials might be due to less cyclic softening occurring during these tests or due to thermal ageing of the materials.

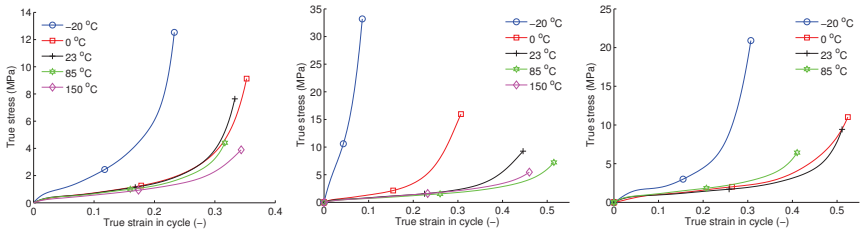

(a) (b) (c)

Figure 8: Fifth cycle mean true stress-strain curve for the (a) HNBR1, (b) HNBR2, and (c) FKM materials.

3.5. Relaxation test

As emphasised in Section 2.2, the specimens were kept at a constant deformation of 40 mm (30 mm for the high temperature tests, see Section 3.1) for 30 minutes during the sixth cycle. The stress relaxation can be defined through a normalized stress $\sigma_N(t) = \sigma(t)/\sigma(t_0)$, where $\sigma(t_0)$ is the stress at the start of the hold period. Figure 9 presents the normalized stress for all materials and temperatures. An exponential decay of the relative stress level with time, as normally found for viscous materials, was observed in all cases. Consistently, the rate of relaxation increased as the temperature was reduced. It is a particular strong relaxation effect at the lowest temperature for the FKM material. These results agree well with the comparatively large hysteresis loops at

low temperatures seen in Figure 5. For temperatures at 0 °C and above, the FKM material has a relative stress level slightly above that of the two HNBR materials, while at a temperature of −20 °C, the FKM material has a significantly lower relative stress. It should be noted that the considerable relaxation occurring in the FKM material at low temperatures would cause a large reduction of the sealing force obtained in a practical application. This could possibly lead to failure of the sealing system due to interfacial leakage.

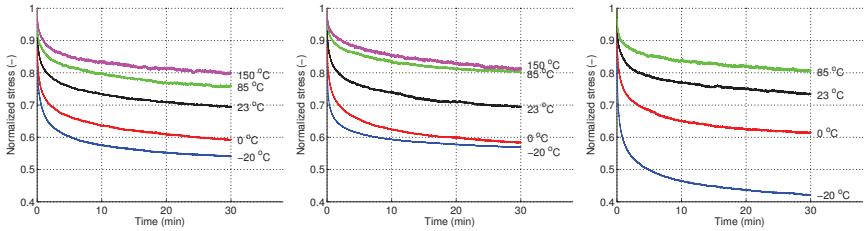

Figure 9: Normalized relaxation behaviour at different temperatures for the (a) HNBR1, (b) HNBR2, and (c) FKM materials.

3.6. Material failure at high temperatures

While no material failure occurred during the tests performed at the three lowest temperatures, this was a considerable challenge for the tests carried out at 85 and 150 °C. Elastomers are in general known to undergo significant chemical degradation, e.g. random chain scission, when exposed to high temperatures [28]. Zhu et al. [29] recently showed that a constant deformation during the high temperature aging process reduced the failure strain significantly for an HNBR compound. It is likely that the chemical degradation caused by the combination of high temperature and large deformation is the reason for the material failures obtained herein.

Table 3 presents an overview of all the tests where material failure was encountered. The table states which material that failed, the test temperature used, if the specimen failed at the clamping or in the gauge section, during which part of the test procedure the failure occurred, at what displacement during a cycle or how long into the relaxation period the failure occurred, and the maximum deformation used in the test procedure. It appears from the table that more than two tests were conducted for the temperatures where failure occurred.

At 85 °C, multiple HNBR1 and FKM samples failed during test series with 40 mm as maximum deformation. Most of these failures occurred by the clamping, and are assumed to be caused by the triaxial stress state that arises in this area. This problem was overcome by reducing the maximum deformation to 30 mm. At 150 °C, one sample of both HNBR compounds failed in the gauge section during the relaxation period, while four consecutive FKM samples failed at this temperature, two by the clamping, and two in the gauge section. FKM compounds are generally

Table 3: Overview of material failure during testing.

Material	Temperature	Failure location	Cycle	Displacement / Time	Max deformation
HNBR1	85 °C	Clamping	Relaxation	3 seconds	40 mm
HNBR1	85 °C	Clamping	First	37 mm	40 mm
HNBR1	85 °C	Clamping	Second	38 mm	40 mm
HNBR1	85 °C	Gauge	Relaxation	8 minutes	40 mm
FKM	85 °C	Clamping	First	33 mm	40 mm
FKM	85 °C	Clamping	Relaxation	23 seconds	40 mm
FKM	85 °C	Clamping	Fourth	36 mm	40 mm
FKM	85 °C	Clamping	Relaxation	13.5 minutes	40 mm
HNBR1	150 °C	Gauge	Relaxation	8.5 minutes	30 mm
HNBR2	150 °C	Gauge	Relaxation	9.5 minutes	30 mm
FKM	150 °C	Gauge	First	25.8 mm	30 mm
FKM	150 °C	Clamping	First	28.3 mm	30 mm
FKM	150 °C	Gauge	Second	29.6 mm	30 mm
FKM	150 °C	Clamping	First	28.3 mm	30 mm

stated to have enhanced high-temperature capabilities compared to HNBR compounds [30]. This capability though, is mainly regarding unstrained aging at high temperatures. When exposed to large tensile deformations combined with the high temperatures however, the results obtained herein indicate that the FKM compound tested is less suited for high-temperature use.

4. Concluding remarks

True stress-strain data was obtained for the cyclic tension behaviour of two HNBR compounds and one FKM compound at a wide range of temperatures. It was shown that HNBR compounds could be assumed to behave incompressible during deformation, while a transverse isotropic assumption had to be used for the FKM compound. In line with previously published results, both elastic stiffness and viscous effects were found to increase as the testing temperature was reduced. In addition, the effect per degree of temperature change was in both cases larger for the lower temperatures.

Comparing the two different HNBR materials, the relaxation behaviour and the elastic response at high temperatures were both found to be comparable. On the other hand, the HNBR2 material revealed a significantly stiffer behaviour than the HNBR1 at low temperatures. In addition, for first loading of the HNBR1 material at 0 and -20 °C, a dip of the stress level could be observed. A considerable volume increase was found to accompany this stress-dip. By use of a finite element model, it was shown that this macroscopic response could be caused by a reduction in the fracture energy for the interface between the matrix material and the filler particles at low temperatures.

Significant material failure was observed for the tests performed at the highest temperatures. For the HNBR1 and the FKM material, the maximum deformation had to be reduced to 30 mm for the tests at 85 °C. At 150 °C, using 30 mm as the maximum deformation, failure in the gauge section was seen for all three materials. For the FKM material, failure occurred during the first few cycles in four consecutive tests, and cyclic material data could not be obtained at this temperature.

In summary, it can be seen that the FKM compound can be challenging as a sealing material at the temperature boundaries. At high temperatures, the material was found to be prone to failure when exposed to tensile loading, while at low temperatures there is a high level of stress relaxation that would lead to a reduced sealing force, and thereby an increased leakage risk. The HNBR materials seem to be less susceptible to failure, and the viscoelastic properties are less sensitive to the temperature variations typically occurring in subsea sealing applications.

Acknowledgements

Aker Solutions are acknowledged for their financial support to this research. The authors would like to express their gratitude to Mr Trond Auestad for his assistance during the experimental work, Mr Lars Edvard Dhli for his guidance on matrix-particle modelling, and to the suppliers who delivered the tests samples for this work free of charge.

References

[1] ISO, 10423:2009 Petroleum and natural gas industries Drilling and production equipment Wellhead and christmas tree equipment, Tech. rep. (2009).

[2] L. R. G. Treloar, The physics of rubber elasticity, Oxford university press, 1975.

[3] J. de Crevoisier, G. Besnard, Y. Merckel, H. Zhang, F. Vion-Loisel, J. Caillard, D. Berghezan, C. Creton, J. Diani, M. Brieu, F. Hild, S. Roux, Volume changes in a filled elastomer studied via digital image correlation, Polymer Testing 31 (2012) 663–670.

[4] G. MacHado, G. Chagnon, D. Favier, Induced anisotropy by the Mullins effect in filled silicone rubber, Mechanics of Materials 50 (2012) 70–80.

[5] H. Bechir, L. Chevalier, M. Chaouche, K. Boufala, Hyperelastic constitutive model for rubber-like materials based on the first Seth strain measures invariant, European Journal of Mechanics, A/Solids 25 (2006) 110–124.

[6] L. A. Wood, G. M. Martin, Compressibility of Natural Rubber at Pressures Below 500 KG/CM2, Rubber Chemistry and Technology 37 (1964) 850–865.

[7] A. G. James, A. Green, Strain energy functions of rubber. II. The characterization of filled vulcanizates, Journal of Applied Polymer Science 19 (1975) 2319–2330.

[8] J. S. Bergström, M. C. Boyce, Mechanical Behavior of Particle Filled Elastomers, Rubber Chemistry and Technology 72 (1999) 633–656.

[9] A. Ilseng, B. H. Skallerud, A. H. Clausen, Volumetric compression of HNBR and FKM elastomers, Constitutive Models for Rubber IX - Proceedings of the 9th European Conference on Constitutive Models for Rubbers, 2015, pp. 235–241.

[10] A. Ilseng, B. H. Skallerud, A. H. Clausen, Case study of elastomer seals using FEM, MekIT'15 - Eighth national conference on Computational Mechanics, CIMNE, Barcelona, 2015, pp. 203–219.

[11] A. D. Drozdov, J. Christiansen, Thermo-viscoplasticity of carbon black-reinforced thermoplastic elastomers, International Journal of Solids and Structures 46 (2009) 2298–2308.

[12] A. Lion, On the large deformation behaviour of reinforced rubber at different temperatures, Journal of the Mechanics and Physics of Solids 45 (1997) 1805–1834.

[13] A. F. M. S. Amin, A. Lion, P. Höfer, Effect of temperature history on the mechanical behaviour of a filler-reinforced NR/BR blend: Literature review and critical experiments, ZAMM Zeitschrift fur Angewandte Mathematik und Mechanik 90 (2010) 347–369.

[14] J. Martinez, A. Boukamel, S. Méo, S. Lejeunes, Statistical approach for a hyper-visco-plastic model for filled rubber: Experimental characterization and numerical modeling, European Journal of Mechanics - A/Solids 30 (2011) 1028–1039.

[15] J. A. Shaw, A. S. Jones, A. S. Wineman, Chemorheological response of elastomers at elevated temperatures: Experiments and simulations, Journal of the Mechanics and Physics of Solids 53 (2005) 2758–2793.

[16] T. Rey, G. Chagnon, J.-B. Le Cam, D. Favier, Influence of the temperature on the mechanical behaviour of filled and unfilled silicone rubbers, Polymer Testing 32 (2013) 492–501.

[17] F. Rouillard, P. Heuillet, B. Omnes, Viscoelastic characterization at low temperature on an HNBR compound for sealing applications, in: Constitutive Models for Rubber VIII - Proceedings of the 8th European Conference on Constitutive Models for Rubbers, ECCMR 2013, 2013, pp. 591–594.

[18] A. S. Khan, M. Baig, S. Hamid, H. Zhang, Thermo-mechanical large deformation responses of Hydrogenated Nitrile Butadiene Rubber (HNBR): Experimental results, International Journal of Solids and Structures 47 (2010) 2653–2659.

[19] H. Laurent, G. Rio, A. Vandenbroucke, N. Aït Hocine, H. L. G. Rio, A. V. N. Aït, Experimental and numerical study on the temperature-dependent behavior of a fluoro-elastomer, Mechanics of Time-Dependent Materials 18 (2014) 721–742.

[20] ISO, 37:2011 Rubber, vulcanized or thermoplastic - Determination of tensile stress-strain properties, Tech. rep. (2011).

[21] E. Fagerholt, T. Børvik, O. Hopperstad, Measuring discontinuous displacement fields in cracked specimens using digital image correlation with mesh adaptation and crack-path optimization, Optics and Lasers in Engineering 51 (2013) 299–310.

[22] ISO, 22007-4:2008, Plastics - Determination of thermal conductivity and thermal diffusivity - Part4: Laser flash method, Tech. rep. (2008).

[23] Abaqus, 6.13-1, Dassault Systèmes, 2013.

[24] MATLAB, version 8.3.0.532 (R2014a), The MathWorks Inc., 2014.

[25] L. Mullins, Softening of rubber by deformation, Rubber chemistry and technology 42 (1969) 339–362.

[26] J. Faleskog, X. Gao, C. Fong Shih, Cell model for nonlinear fracture analysis - I. Micromechanics calibration, International Journal of Fracture 89 (1998) 355–373.

[27] J. Kim, X. Gao, T. S. Srivatsan, Modeling of void growth in ductile solids: effects of stress triaxiality and initial porosity, Engineering Fracture Mechanics 71 (2004) 379–400.

[28] P. Krzysztof, N. James, Thermal Degradation of Polymeric Materials, Rapra Technology, 2005.

[29] Z. Zhu, C. Jiang, Q. Cheng, J. Zhang, S. Guo, Y. Xiong, B. Fu, W. Yang, H. Jiang, Accelerated aging test of hydrogenated nitrile butadiene rubber using the time-temperature-strain superposition principle, RSC Adv. 5 (2015) 90178–90183.

[30] A. Ciesielski, An Introduction to Rubber Technology, Smithers Rapra Technology, 1999.

Paper II

Arne Ilseng, Bjørn H. Skallerud, Arild H. Clausen

An experimental and numerical study on the volume change of particle-filled elastomers in various loading modes

Submitted for journal publication

Paper II

An experimental and numerical study on the volume change of particle-filled elastomers in various loading modes

Arne Ilseng[a,b,*], Bjørn H. Skallerud[a], Arild H. Clausen[a]

[a] *Department of Structural Engineering, Norwegian University of Science and Technology, 7491 Trondheim, Norway*
[b] *Aker Solutions AS, 3408 Tranby, Norway*

Abstract

A pronounced difference in the volumetric response between uniaxial tension and confined axial compression loading was found for commercial HNBR and FKM particle-filled elastomeric compounds. In uniaxial tension (UT), a volume increase of 5 and 20 % for the HNBR and FKM respectively was found for a hydrostatic stress of less than 6 MPa , in addition, both compounds showed a clear hysteresis loop in the hydrostatic stress - volume ratio space. However, for confined axial compression (CAC) tests, the materials reached a 6-7 % volume change for a hydrostatic stress of 140 MPa, and an elastic behaviour was seen. This loading mode dependence of the volumetric response has severe implications for the constitutive representation of the materials, and it is demonstrated that existing elastomer models are unable to capture the behaviour in both loading modes. To gain an increased understanding of the macroscopically obtained results, a tension in situ scanning electron microscopy study was performed. Matrix-particle debonding was observed to occur at the external surface of the materials, rendering a possible explanation for the loading mode dependent volumetric behaviour. Finite element simulations of a unit cell, incorporating a cylinder of matrix material with a spherical particle in its centre, showed that the observed debonding can explain the experimental response of the materials in a qualitative manner.

Keywords: Particle-filled elastomers, Volume change, In situ SEM, Unit cell simulations

1. Introduction

Constitutive models commonly applied to predict the visco-hyperelastic response of elastomers in finite element simulations assume a nearly isochoric behaviour independent of loading mode [1, 2, 3]. Based on available experimental data in uniaxial tension (UT) [4] and confined axial compression (CAC) [5], there are clear indications that this approach can be inaccurate for certain elastomers. It appears that the materials can exhibit a considerable increase of volume in UT, while the response in CAC is much stiffer with respect to volume change. However, before embarking on the task of developing constitutive models with improved correspondence to experimental

*arne.ilseng@ntnu.no

observations, an enhanced understanding of the underlying mechanisms causing the loading mode dependent volume behaviour should be provided.

Early work on elastomers (e.g. [6, 7, 8]) mainly dealt with the behaviour of unfilled elastomer gums, for which the assumption of constant volume got accepted as the standard. However, raw gum elastomers have limited industrial application, and filler particles are normally added to the blend of industrial materials [9]. These fillers improve mechanical properties like stiffness and strength, but may also alter the volumetric behaviour of the compounds.

Gent and Park [10] and Cho et al. [11] illustrated the possible effect that stiff particles can have on the volumetric response of elastomers by testing samples of a transparent elastomer matrix with spherical or cylindrical glass inclusions in uniaxial tension. They differentiated the observed response between two failure mechanisms; cavitation, i.e. the occurrence of voids in the material due to stress concentrations near the stiff inclusions; and decohesion, i.e. rupture of the cohesive zone between the inclusion and the matrix material. The failure process was initiated by the occurrence of small voids close to the stiff inclusion, which during deformation grew and coalesced to form larger cavities. As these cavities increased in size, they eventually led to decohesion between the filler particle and the surrounding elastomer matrix. For experiments involving large hydrostatic stresses, Gent and Lindley [12] also found cavitation to occur in unfilled elastomers. This was attributed to pre-existing defects, experiencing unbounded growth when the hydrostatic tension stress exceeded a critical value. Such cavitation under high triaxiality stress states has later been studied further by different authors, e.g. [13, 14, 15]. It is clear that the stress/deformation level where voids would start to grow and the number of voids that would initiate prior to particle decohesion are strongly dependent on properties like the fracture strength of the matrix material, the size and shape of the particles, and the cohesive strength between the matrix and its filler particles. In any event, a process of cavitation and decohesion would lead to a macroscopic volume growth of the material.

For the early research on the volumetric behaviour of elastomers, the most accessible method for measuring global volume changes accompanying deformation was through dilatometry tests [16, 17, 18, 19]. However, the progress of modern measuring techniques has simplified the evaluation of volume changes accompanying deformation significantly through the development of optical methods, like digital image correlation (DIC). Using DIC, Le Cam and Toussaint [20] looked at the competition between volume increase due to void growth and volume decrease due to crystallization in natural rubber loaded in tension. They measured the volume change using DIC at one surface and assuming an isotropic material behaviour. The results showed significantly larger volume growth for particle-filled natural rubber than for unfilled natural rubber. Due to crystallization, they observed a larger volume during loading compared with unloading. Le Cam and Toussaint [21] also found a significant volume change in filled styrene-butadiene (SBR) dog-bone shaped specimens using a similar set-up. de Crevoisier et al. [22] measured volume growth during cyclic loading of

a filled SBR specimen using DIC at two perpendicular surfaces of a dog-bone-shaped specimen. They found the material to behave slightly anisotropic and to display a relatively small volume change. They also reported that the volume change in each deformation cycle started when the longitudinal deformation exceeded the previously obtained maximum deformation. Cantournet et al. [23] recently studied the volume increase of a particle-filled natural rubber under various loading conditions. They measured the volume change occurring under uniaxial tension by use of a video traction system at one surface and the assumption of isotropic material behaviour. The increase in volume was explained by cavitation and decohesion, and this phenomenon was studied using in situ scanning electron microscopy (SEM). They found that for loading at low stress triaxiality, volume growth occurred near ZnO particles, while no debonding could be observed between the elastomer matrix and carbon black particles.

Unit cell simulations are often used to explain globally observed results by studying mechanisms occurring at the scale of the material constituents. Such models have been extensively employed to study ductile fracture in metallic materials, e.g. [24, 25, 26, 27], and to some extent to study the behaviour of particle-filled polymeric materials [28, 29, 30, 31]. Steenbrink et al. [28] and Cheng and Guo [29] looked at the effect of empty voids in glassy polymers by use of axisymmetric cell analyses. Ognedal et al. [30] studied decohesion and volume growth in a mineral-filled PVC using a 3D model to resemble a polymer matrix with spherical particles. For the study of elastomers, Bergström and Boyce [31] looked at how shape, dimension, and stiffness of carbon black particles altered the resulting equilibrium behaviour on the macro scale.

Although the matrix-particle debonding effect in elastomers is experimentally documented in the literature, the implications this have for the macroscopic mechanical response has gained limited attention. This article will study HNBR and FKM materials in UT and CAC to investigate the difference in volumetric behaviour. To examine the source of the volume growth observed in the UT experiments, an in situ SEM study of tensioned specimens was performed. Unit cell simulations were then used to see if the behaviour observed in the macroscopic experiments could be captured in a qualitative manner. No study could be found in the literature neither dealing with the volumetric behaviour of HNBR and FKM elastomers nor debonding or cavitation around particles in such materials. In addition, to the best of the authors' knowledge, unit cell simulations have not yet been used to study the loading mode dependent volume behaviour of particle-filled elastomeric materials.

The article is organized as follows: The set-up and results for the UT and CAC macroscopic experiments are presented in the following section. Implications of the findings for constitutive modelling of particle-filled elastomers are discussed in Section 3. In Section 4, the set-up and results of the in situ SEM study on the materials are given, while Section 5 presents a unit cell study to explain the macroscopic experimental results in a qualitatively manner. In the final section, a summary and some concluding remarks are given.

2. Macroscopic experiments

2.1. Uniaxial tension

2.1.1. Set-up

For the UT tests, one HNBR and one FKM compound were delivered from two different suppliers as 2 mm thick dog-bone shaped tension specimens with dimensions in line with ISO37 Type–1 and Type–2 respectively [32]. The gauge length of the Type–1 specimens applied for HNBR is 33 mm, while the corresponding length of the Type–2 FKM samples is 25 mm. The specimens were tested using an Instron 5944 testing machine with a 2 kN load cell. One deformation cycle exposed the test samples to a maximum machine displacement of 40 mm and immediate unloading until zero force was measured by the load cell. A deformation rate of 1 mm/s was used during both loading and unloading.

While the force level F was measured by the load cell of the machine, optical means were used to determine the local deformations in the gauge section. For this purpose, a grey scale speckle pattern was applied to the specimens prior to testing, and two Prosilica GC2450 CCD cameras were used to capture frames of the wide and narrow surface of the specimen throughout the tests. The obtained images were post-processed using the in-house DIC software *eCorr* [33]. An illustration of the tension test sample and the boundaries monitored by the two cameras can be seen in Figure 1. Two repetitions were performed for each material, with the duplicate tests echoing the results presented here.

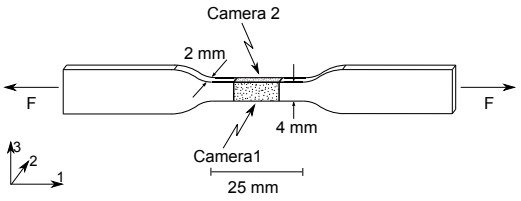

Figure 1: Illustration of the experimental set-up used in the UT experiments, geometrical measures in line with ISO 37 Type–2 used for the FKM samples.

Applying the two perpendicular cameras for the DIC measurements, all three stretch components λ_i, $i = 1, 2, 3$ with the directions being defined through the Cartesian coordinate system in Figure 1, were obtained throughout the test. Thereby, the volume ratio J was found without using the assumption of material isotropy ($\lambda_2 = \lambda_3$), with J being calculated from

$$J = \frac{V}{V_0} = \lambda_1 \lambda_2 \lambda_3 \tag{1}$$

where V is the current volume and V_0 the reference volume. In addition, the longitudinal Cauchy stress σ_1 was found in a correct manner, i.e. without using assumptions of isotropic or isochoric ($\lambda_2 = \lambda_3 = 1/\sqrt{\lambda_1}$) material behaviour, through

$$\sigma_1 = \frac{F}{\lambda_2 \lambda_3 A_0} \tag{2}$$

where A_0 is the initial cross sectional area of the specimen. For UT loading, where $\sigma_2 = \sigma_3 = 0$, the hydrostatic stress is defined as

$$\sigma_H = \frac{\sigma_1}{3} \tag{3}$$

The importance of the dual camera set-up is illustrated in Figure 2, showing the longitudinal (positive) and transverse (negative) logarithmic strains obtained by the two cameras for both materials. It is seen that the relative difference between the longitudinal strains measured from the two independent yet synchronized cameras is negligible throughout the tests. For the transverse strains on the other hand, there is a clear discrepancy caused by transverse anisotropic material behaviour. This transverse anisotropy is assumed to originate in the production process of the 2 mm thick sheets from which the specimens were cut. The implications of neglecting this transverse anisotropy when calculating the stress and volume growth during the test is discussed in Section 2.1.2.

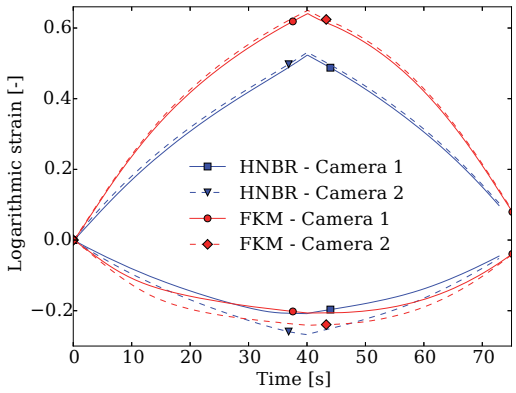

Figure 2: Longitudinal and transverse strains calculated by DIC for HNBR and FKM subjected to one deformation cycle in tension.

2.1.2. Results

The results obtained for the deformation cycle are presented in Figure 3. From the Cauchy stress - logarithmic strain curves displayed in Figure 3a, the initial tension behaviour is seen to be similar for the two materials, while the HNBR compound displays a higher stress level as the strain is increased. The FKM sample reaches a larger maximum strain level due to the difference in initial geometry. The volume ratio for the two materials with respect to longitudinal strain is addressed in Figure 3b. For both materials, the volume ratio is seen to stay close to unity during the initial deformation, until a critical strain level is reached at which a clear increase in volume ratio begins. The strain level at the onset of volume increase is clearly smaller for the FKM material compared with the HNBR compound. In addition, the maximum volume increase is more than 20 % for the FKM material, opposed to approximately 5 % for the HNBR compound. No study could be found

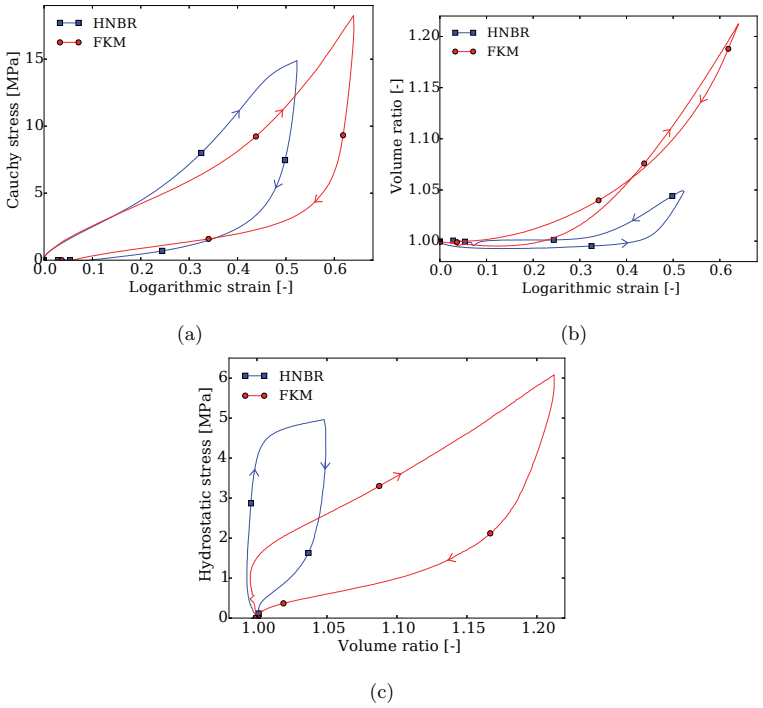

Figure 3: Results from UT experiments (a) stress-strain, (b) volume ratio - logarithmic strain, and (c) hydrostatic stress - volume ratio behaviour. Arrows indicate loading and unloading directions.

in the literature reporting such a large volume increase at the given strain level for an elastomer as the one found for the FKM material.

In Figure 3c, the hydrostatic stress level is plotted towards the volume ratio. A critical hydrostatic stress (corresponding to the critical strain level) is seen to be required before the volume increase sets on, with a clearly higher stress being needed in the HNBR material compared with the FKM compound.

It should be noted that due to the volume increase, using an assumption of isochoric material behaviour and calculating the stress-strain data using the longitudinal strains from Camera 1 would over-predict the stress level at maximum deformation with about 3 % for the HNBR material and more than 20 % for the FKM material. In addition, due to the transverse anisotropic behaviour of the materials, using data only from Camera 1 and assuming isotropic material behaviour would lead to an over-prediction of the maximum volume change for the HNBR material by 130 %, and a 20 % over-prediction of the volume increase in the FKM compound. The level of material anisotropy in elastomeric tension samples is seldom measured and reported in the literature, and experimental set-ups are often based on an assumption of transverse isotropic material behaviour, however, this brief discussion emphasize the bias a single camera set-up might cause for certain

materials.

2.2. Confined axial compression

2.2.1. Set-up

To evaluate the volumetric response of the samples in nearly hydrostatic compression, a CAC rig was built. A thorough presentation of the set-up was provided by Ilseng et al. [5], however, a brief discussion is included here for completeness. The specimens used for CAC were cylinders with a height of 12.5 mm and a diameter of 29.0 mm (in accordance with ISO 815-1 Type A [34]). While the same HNBR compound could be delivered as samples for both UT and CAC experiments, it was not possible for the supplier to provide a compression specimen of the FKM compound that was tested in tension. However, two other FKM compounds, named FKM1 and FKM2, were delivered with the geometries used for CAC. It is believed that the two other compounds would give an indication of the CAC behaviour of the FKM compound tested in tension.

An illustration of the CAC rig is presented in Figure 4. The rig was designed to be used with an Instron 5982 universal testing machine with a t-slot table, and involves two pistons with load cells and a 20 mm thick steel plate supported on four M16 bolts. The centre hole of the steel plate was produced with a diameter of 29.0 mm and with a tolerance of +0.05 mm −0.00 mm, while the two pistons were produced with a diameter of 29.0 mm and a tolerance of +0.00 mm −0.05 mm to ensure a tight fit. The plate was fixed to the t-slot table in the machine by the four steel bolts, while the two pistons were screwed onto the respective load cells. In addition to the 100 kN load cell in the testing machine, an HBM U2A 100 kN load cell was included below the specimen and fixed to the t-slot table with bolts. The purpose of the second load cell was to facilitate measurement of the frictional forces that arise during testing. To avoid dealing with the compliance of the testing machine, a checkerboard pattern was applied to the upper piston and a camera was used to log images of this pattern throughout the tests. By use of a point tracker routine [35], the displacement of the upper piston could be calculated. It was assumed that the test set-up, which was made of steel, was fully rigid and that all deformation therefore occurred in the specimen. Based on this assumption, the volume ratio can be defined as

$$J = \frac{H}{H_0} \tag{4}$$

where H is the current height of the specimen, while H_0 is the initial height. A silicon grease was applied to all surfaces of the specimens prior to testing, and this treatment was found to reduce the frictional forces between the specimen and the steel plate significantly. Using the grease, the frictional force was less than 1.3 % of the load in the upper load cell at maximum load for all tests.

All specimens were tested by a cyclic loading history, obtaining a force in the upper load cell of 95 kN by load control before returning to 0.1 kN and starting a new cycle. A deformation rate of 3 mm/min was applied during both loading and unloading. In the sixth cycle, the load level was kept constant at 95 kN for 30 minutes as a volumetric creep test. By denoting the measured force

level by F and the area of the circular cross section of the specimen as A_0, the hydrostatic stress applied to the specimen can be approximated by the relation

$$\sigma_H \approx \frac{F}{A_0} \tag{5}$$

The approximation in Equation 5 is only valid if the deformation is governed by volumetric rather than deviatoric stresses. The validity of this assumption for the presented experiments is discussed further in Section 2.2.2.

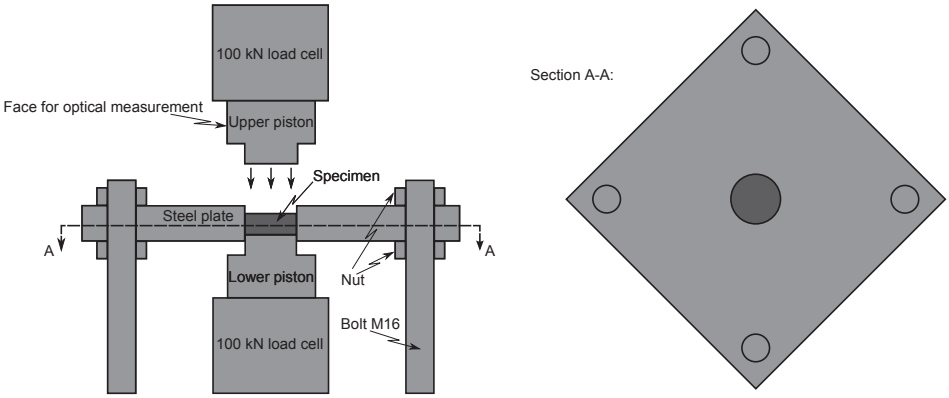

Figure 4: Illustration of the experimental set-up used for the confined axial compression experiments.

2.2.2. Results

The raw force-displacement data obtained for the six loading cycles on the HNBR material is presented in Figure 5a. Qualitatively, this response is also representative for the two FKM materials. It can be seen that the force level is nearly zero the first 0.4 mm of deformation. This is interpreted as the deformation needed to obtain full contact between the two pistons and the specimen. Thereafter, the stiffness is gradually increasing until a constant level is reached at approximately 0.6 mm of deformation. This stage is interpreted as mainly deviatoric deformation needed to obtain full contact between the specimen boundaries and the hole in the steel plate. For the rest of the loading and the following cycles, a nearly constant stiffness and no significant hysteresis or cycle dependence can be seen. For the creep test, only a slight volume increase can be observed. As the deviatoric behaviour of the material has been found to be viscous and cycle dependent [4] the deformation in this stage is likely to be dominated by the hydrostatic stresses, meaning that Equation 5 yields a good approximation to the hydrostatic stress response of the materials.

The hydrostatic stress - volume ratio behaviour obtained during loading in the fifth deformation cycle for the three materials can be seen in Figure 5b. A relatively similar response is seen for the HNBR and the FKM1 materials with 6 % volume increase at a hydrostatic stress of 140 MPa,

while the FKM2 material shows a slightly more compliant volumetric response with 7 % volume increase at maximum stress.

It should be noted that the volumetric response obtained in CAC differs significantly from that obtained in UT, as shown in Figure 3c, where a volume increase of respectively 5 and 20 % was achieved for a hydrostatic stress of less than 6 MPa. Some implications of this loading mode dependent volume behaviour for the constitutive modelling of particle-filled elastomers are discussed in the following section.

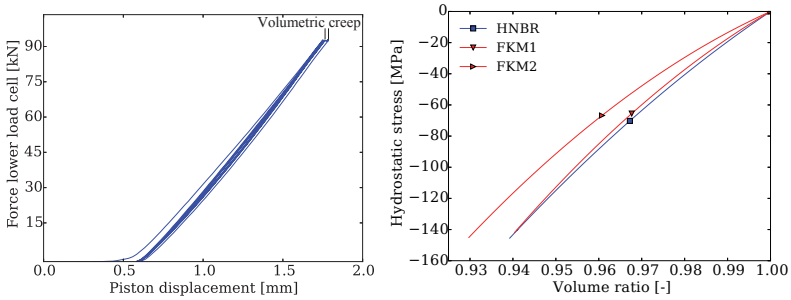

(a) (b)

Figure 5: Results from confined axial compression experiments. (a) Force - displacement data for the HNBR material subjected to six loading cycles and (b) hydrostatic stress - volume ratio behaviour obtained during loading in the fifth deformation cycle for all three compounds.

3. Implications for constitutive modelling

In constitutive modelling of elastomeric materials, it is common to split a hyperelastic strain energy potential W additively in an isochoric and a volumetric contribution

$$W = W_{iso}\left(I_1^*, I_2^*\right) + W_{vol}\left(J\right) \tag{6}$$

where I_1^* and I_2^* are the first and second invariant of the distortional left Cauchy-Green deformation tensor. From this potential function, the hydrostatic stress term can be found as

$$\boldsymbol{\sigma}_{vol} = \frac{\partial W_{vol}}{\partial J}\mathbf{I} = \sigma_H \mathbf{I} \tag{7}$$

While a wide range of both phenomenological and physically based functional forms for the isochoric response has been proposed and discussed in the literature [36], the number of functional forms for the volumetric behaviour is limited. Different phenomenological volumetric hyperelastic potential functions were discussed by Doll and Schweizerhof [37] and by Bischoff et al. [38], and three of the

more commonly applied forms for the volumetric part are [39, 40, 41]

$$
\begin{aligned}
W^a_{vol} &= \frac{\kappa}{2}\left(J-1\right)^2 \Rightarrow \sigma^a_H = \kappa\left(J-1\right) \\
W^b_{vol} &= \frac{\kappa}{2}\left(\frac{J^2-1}{2} - \ln J\right) \Rightarrow \sigma^b_H = \frac{\kappa}{2}\left(J - \frac{1}{J}\right) \\
W^c_{vol} &= \frac{\kappa}{2}\left(\ln J\right)^2 \Rightarrow \sigma^c_H = \kappa\left(\frac{\ln J}{J}\right)
\end{aligned}
\tag{8}
$$

In Figure 6, the parameter κ of the three different volumetric terms given in Equation 8 is optimized to fit the CAC data for the FKM1 material. The predicted hydrostatic stresses companying a volume increase are then compared with the volumetric data obtained for the FKM material in the UT experiments. While it is seen that all three expressions for the volumetric part of the strain energy potential yield a good correspondence with the CAC data, none of them are capable of predicting the compliant volumetric response in UT.

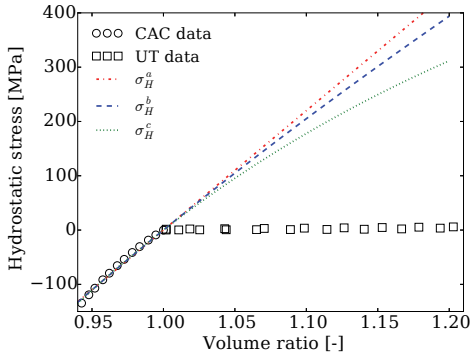

Figure 6: Comparison of different hydrostatic stress terms proposed in literature with experimental data for FKM in UT and CAC.

In addition to the large difference in volumetric response between UT and CAC, purely hyperelastic material models would not be able to capture the hysteresis loop in hydrostatic stress - volume ratio space seen in Figure 3c. While Reese and Govindjee [42] introduced a constitutive framework for viscous volume growth, most models aiming to predict the viscoelastic response of elastomeric materials assume a nearly isochoric behaviour, and only stiff and elastic volumetric deformations are included [1, 2, 3].

Clearly, a new modelling approach is needed to capture the behaviour seen in the macroscopic experiments. An important feature of such a model would be the ability to predict a compliant viscous volume growth for loading modes including positive hydrostatic stresses, at the same time as a stiff and elastic volume response would be predicted in hydrostatic compression. To the best of the authors' knowledge, none of the constitutive models in the literature aimed at modelling elastomeric behaviour includes these effects. However, before one embarks at the task of deriving new constitutive equations, more knowledge on the mechanisms causing the observed macroscopic

behaviour should be obtained. Therefore, the rest of this paper is devoted to study the observed response in more detail, while the derivation of a new model is postponed to a forthcoming paper.

The significant difference in volume change between the two loading modes can possibly be explained by cavitation and decohesion occurring near stiff inclusions in UT, while this would not be applicable during CAC deformation. To investigate this hypothesis further, an in situ SEM study is presented in the following section.

4. SEM study

4.1. Set-up

The SEM study was performed using a Zeiss Gemini Ultra 55 Limited Edition microscope at the Department of Materials Science and Engineering, NTNU. This instrument provided micrographs with a resolution of 3072×2072 pixels. A purpose-built tension rig [43] was placed on the sample board of the microscope to enable in situ measurements during uniaxial tension. An illustration of the tension rig is shown in Figure 7a. Small tension specimens, having dimensions in line with the sketch in Figure 7b, were cut from the ISO geometry tension specimens delivered by the suppliers, i.e. cut from untested samples from the same production batch of specimens as those tested in macroscopic uniaxial tension.

Prior to any deformation, images at 60, 100 and 300 times magnification were obtained of the surface at both the centre and the edge of the specimen, resulting in six images for each compound. The locations of the pre-deformation images are illustrated in Figure 8, showing an overview image of the 3 mm wide gauge section surface. These micrographs were analysed using the Python image processing package scikit-image [44] to obtain an indication of the size, number, and distribution of particles in the materials surface. The particles were distinguished from the matrix material by image segmentation, using Otsu's method [45] to define the threshold value, i.e. minimizing the grey-level variance of each segment.

After tensioning the specimens at a low rate to a nominal longitudinal stretch of 2, the samples were studied again with SEM to look for effects that could explain the macroscopic behaviour seen in Section 2. The samples were then scanned by a random walk procedure and micrographs were captured at sites of interest.

4.2. Results

4.2.1. Particle distribution

The pre-deformation micrograph obtained at 60× magnification in the centre of the specimen surface is shown for both materials in Figure 9. A number of highly reflecting inclusions can be seen at the surfaces. Energy-dispersive X-ray spectroscopy (EDS) suggested that these, for both the HNBR and the FKM material, are ZnO particles. The geometry of the observed particles ranges from nearly circular to oblong shapes, while the particles can be seen to be rather evenly

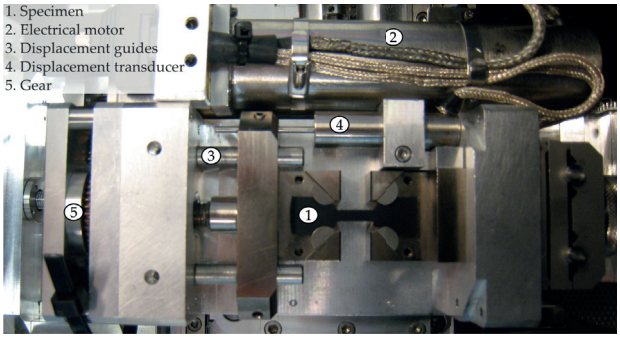

(a)

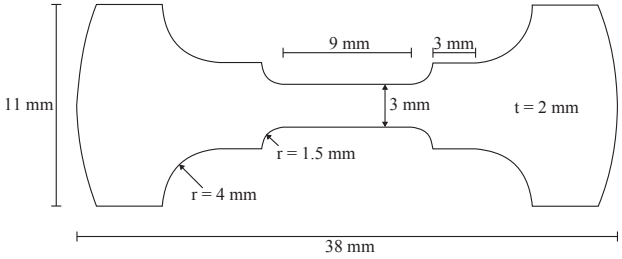

(b)

Figure 7: Setup for in situ SEM study. (a) HNBR specimen in tension rig and (b) geometry of specimens cut from virgin ISO dimension tension samples.

distributed in the surface without any clear clustering. Dimples can be seen at the surface of the FKM material, but it is not clear if these are representative for voids in the bulk material or only surface effects caused by particles removed from the surface during or after the processing of the samples. However, the fraction of internal voids is expected to be limited, due to the stiff and elastic volume response observed in the CAC experiments. Surface dimples were also observed in images of the HNBR material, although not present in the 60× magnification image from the centre part of the sample shown in Figure 9.

From the segmentation process performed on all pre-deformation images, the total number and size of individual particles could be estimated. The obtained area fraction of particles as function of the applied magnification is plotted for all micrographs in Figure 10a, while the total number of particles is shown in Figure 10b. It is clear that the FKM material contains both a larger area fraction and a larger number of particles at the surface. It should be noted that since the number of particles found at the centre location of the FKM material grows as the magnification increases, the area fraction at the low magnification levels for this material is underestimated, since a subset of the image is found to contain more particles than what were counted in the entire micrograph at 60 and 100 times magnification.

In Figure 10c, the particles identified in the 60× magnification images were numbered according

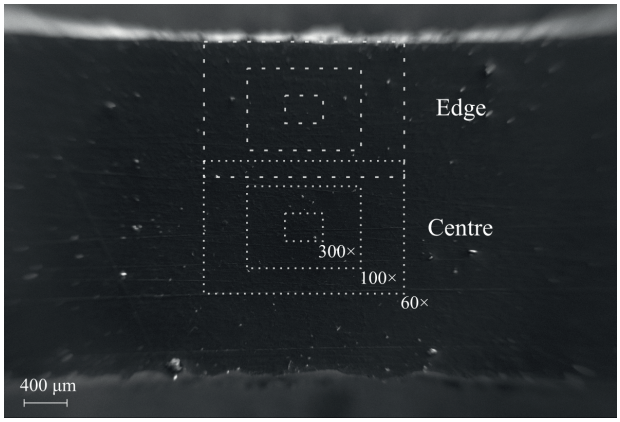

Figure 8: Overview of SEM images of the surface obtained prior to deformation, shown on a micrograph of the HNBR material. The image shows a part of the 9 mm long, 3 mm wide gauge section of the specimens.

to the size of their projected area. This gives an indication of the distribution between large and small particles. For both materials, the edge of the specimen is seen to contain more and larger particles compared with the centre. It is also clear that the materials contain a high number of small particles, and only a few particles having larger size. The largest particle found in the inspected regions had a projected area of 1125 μm^2, found at the edge of the FKM material, while the smallest particle possible to identify with this method at 60× magnification had a projected area of 0.09 μm^2.

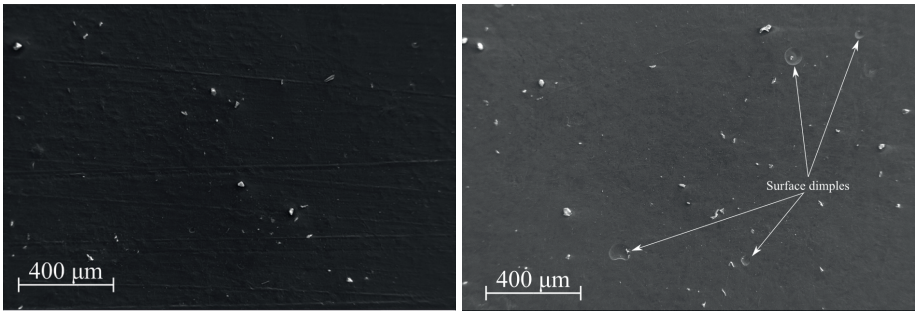

(a) (b)

Figure 9: Pre-deformation SEM images from sample centre at 60× magnification for (a) HNBR and (b) FKM.

4.2.2. Debonding and cavitation

For the in situ tension images, it was found that deforming the specimens changed the conductive properties of the compounds, reducing the image quality at large deformations. This was particularly challenging for the FKM material, yet, matrix-particle debonding and cavitation could be found at the surface of both compounds as illustrated in Figure 11, where sub-figures (a) to (c)

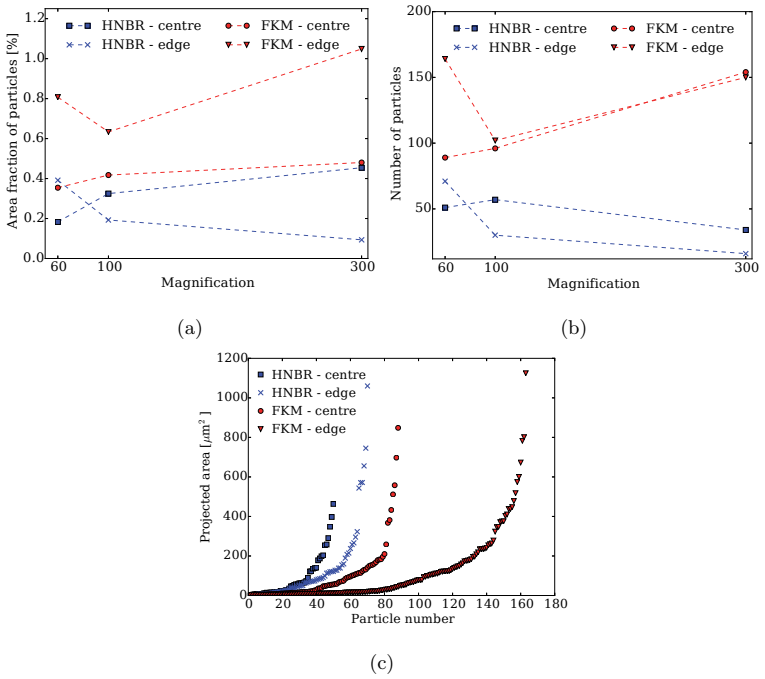

Figure 10: Results obtained from segmentation of the pre-deformation SEM images. (a) Area fraction of particles for all images, (b) the number of particles found in each image, and (c) particle distribution for images at 60× magnification.

address the HNBR material, while (d) addresses the FKM compound.

The image in Figure 11a shows clear debonding at location 1, with cavities formed at both sides of the large particle while the bonding with the matrix seems to be intact at the upper and lower surfaces. At location 2, a cavity is seen with a circular particle near its centre. However, with the cavity being very large compared to the particle, and the particle being completely debonded from the matrix, it is unclear if the cavity is caused by this centre particle or if it is a matrix cavity in the surface caused by the stress situation that incidentally has a centre particle. The particle at location 3 can be seen to have an early-stage debonding at both sides. A slightly different debonding mechanism is illustrated Figure 11b, where a large crater caused by debonding is seen at location 1, while only slight debonding has taken place at location 2. This one-sided debonding mechanism was also observed for other irregularly shaped particles. Another example is provided in Figure 11c, where the large particle has debonded along the surface at location 1 only. At location 2 on the other hand, matrix cavitation, without any visible interior particle, has taken place in front of the large particle. It should be noted that for the micrographs of the HNBR material in Figure 11, particles fully preserving their bonding to the matrix material could also be observed.

For the FKM compound, one micrograph showing a particle in a large cavity could be obtained, as shown in Figure 11d. Due to the large size of the cavity compared with the particle, it is unclear if the debonding is due to the stress situation caused by the centre particle or due to surrounding particles giving rise to a highly triaxial stress situation in the observed area.

While a number of clearly debonding particles could be identified in the in situ images of the HNBR material, only one occurrence of matrix cavitation, the one shown at location 2 in Figure 11c, could be observed. It is not known what caused this free cavity to nucleate, but one hypothesis is that it initiated at a location where a particle had fallen out of the surface during production of the rubber mats from which the specimens were cut. This suggests that the debonding mechanism, and not matrix cavitation, is dominating the volume growth of the material in tension. However, it is noted that matrix cavitation could be more pronounced in the interior of the material, where the absence of a free surface would lead to significantly larger local hydrostatic stresses.

In general, all debonding particles shown in Figure 11 have a relatively large projected area compared with the majority of the particles indicated in Figure 10c.

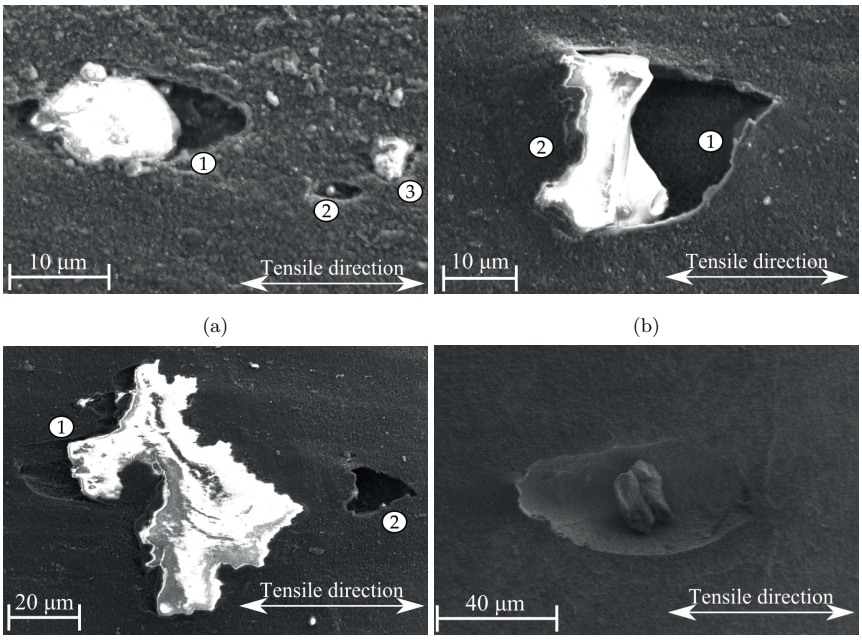

Figure 11: Debonding observed at a nominal longitudinal stretch of approximately 2. (a) Two sided debonding in HNBR, (b) one sided debonding in HNBR, (c) one sided debonding and matrix cavitation in HNBR, and (d) debonding/cavitation in FKM.

5. Unit cell study

5.1. Model

A micromechanical numerical model was used to investigate if the matrix-particle debonding mechanism observed by in situ SEM in Section 4 can explain the volumetric response found in the experimental data of Section 2. It was shown by Willams et al. [46] that such a model would only provide a quantitative prediction of the macroscopic behaviour if a full 3D model was used, taking particle shape, size, distribution, and cohesive strength into account. This would require extensive data on the actual particle distribution, for example through X-ray tomography studies [47, 48], and comprehensive knowledge of the matrix-particle interface behaviour. In addition, running such a model would require large computational resources. The purpose here, however, is to do a qualitative study aimed at investigating the mechanisms of matrix-particle debonding, and how this feature affects the macroscopic response. A relatively simple and efficient numerical model should therefore be sufficient. Thus, a cylinder of matrix material containing one spherical particle embedded at its centre is studied. It is important to note that such a model neglects multiple features of the actual materials like the different particle geometries, the size distribution of the particles, the difference in cohesive behaviour for the particles, interaction effects between the particles and so on.

To incorporate the simple unit cell model in a finite element framework, the commercial software Abaqus/Standard [49] was used. An illustration of the model and the behaviour in the two loading modes are presented in Figure 12, which also shows the finite element discretization. Approximately 1000 elements were used for the matrix material, while about 200 elements were used to mesh the particle. Four node axisymmetric elements with reduced integration and hourglass control, named CAX4R in Abaqus, were applied in the analyses. The external boundaries of the cell were constrained to remain straight throughout the deformation. The model was exposed to UT loading by applying the stress - time data obtained in the experimental tests to the upper boundary as a negative pressure force, while the vertical external boundary was free to move horizontally. The CAC experiment was modelled by applying the stress - time data measured in the fifth cycle of the corresponding test to the upper surface, while a fixed analytically rigid wall constrained the cell from expanding horizontally. Due to the cohesive zone, a length scale must be introduced in the model and the matrix cylinder was given a height and diameter of 20 micrometres.

5.2. Particle size

The macroscopic volume increase obtained in the unit cell model during UT deformation is strongly dependent on the size of the embedded particle, as shown in Figure 13 where the volume ratio obtained at a longitudinal logarithmic strain of 0.7 for simulations with different particle volume fractions is illustrated (for these simulations, no cohesive zone was defined). Comparing with the area fraction of particles in the surface found from the SEM study in Figure 10a (<1

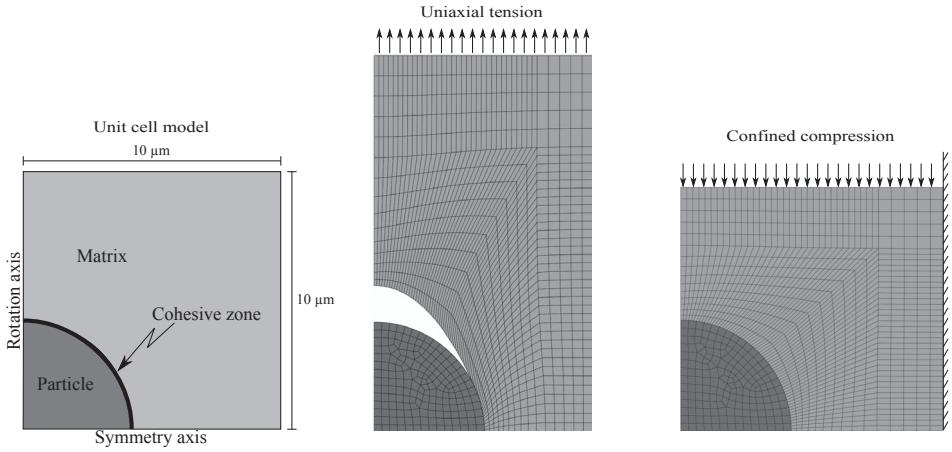

Figure 12: Illustration of axisymmetric unit cell model and its response in the two loading modes, $f_0 = 5\,\%$.

%), it is clear that the volume ratio of particles must be overestimated to get a significant volume growth. There can be multiple explanations for this fact. First, as already mentioned, the model is too simple to provide quantitatively precise results due to the lack of matrix cavitation, neglecting the particle size distribution, inaccurate modelling of the complex particle geometries, and the lack of particle interaction effects. The latter is assumed the most important effect for the total volume growth, as the interaction between particles leads to increased local hydrostatic stresses, promoting decohesion and volume growth [50, 51]. Second, the area fraction of particles obtained from the micrographs might underestimate the actual volume fraction of inclusions due to sub-pixel particles and/or an inhomogeneous particle distribution through the thickness of the samples.

For the purpose of the following qualitative study, the particle size of the basis model was set to yield a volume fraction f_0 of 5 %, such that a clear volume increase could be obtained in UT loading.

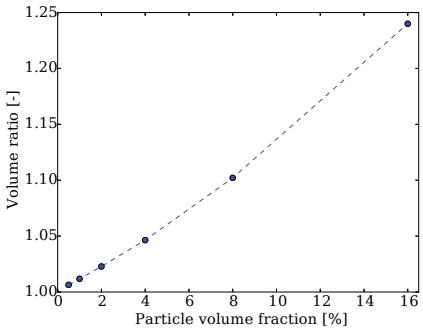

Figure 13: Volume change prediction at a longitudinal logarithmic strain of 0.7 and no cohesion for a set of particle volume fractions.

μ [MPa]	λ_m [-]	D [1/MPa]	S [-]	A [MPa^{-m}s^{-1}]	c [-]	m [-]
2.5	1.6	0.015	12	0.001	0	6

Table 1: Constitutive parameters used for matrix material in unit cell simulations.

5.3. Constitutive modelling

For the constitutive modelling of the matrix material, the visco-hyperelastic Bergström-Boyce model implemented in Abaqus, using a nearly isochoric Arruda-Boyce strain energy potential, was applied. The parameters for the model are listed in Table 1 where the same notation as in Abaqus Theory Guide [52] is adopted, with μ being the shear modulus of the spring in the elastic part, λ_m the locking stretch, D the compressibility parameter (related to the bulk modulus by $\kappa = 2/D$), S the scaling of the stiffness between the elastic and the viscous parts, A a scaling parameter for the viscous deformation, c an exponent for the strain dependence of the viscous deformation, and m an exponent for the stress dependence of the viscous deformation. The parameters used were found to capture the experimentally obtained macroscopic stress - strain behaviour in an approximate manner. The embedded filler particle was modelled as linear elastic with Young's modulus of 140 GPa and Poisson's ratio of 0.3, being approximate values for bulk ZnO [53].

5.4. Cohesive behaviour

The cohesive zone between the matrix and the particle was modelled as an interaction property using a linear traction-separation law with a quadratic stress criterion. Such a modelling of the cohesive zone has been used in a range of studies, e.g. [30, 54, 55] to name a few. The model is illustrated in the sketch in Figure 14. The stress needed to separate the two surfaces increases linearly with a stiffness k until an initiation stress T_{ini} is reached (coinciding with the initiation deformation δ_{ini}). The load bearing capacity of the cohesive zone is then reduced linearly until a total fracture energy of G_c is reached (taking place at a critical deformation of δ_{crit}). Due to the absolute lack of experimental data on the matrix-particle interface behaviour of the materials, the parameters of the base model were set to be $T_{ini} = 6$ MPa, $k = 6$ GPa/μm, and $G_c = 15$ J/m^2, as this gave a reasonable representation of the experimental results. The critical stress was set equal in normal and shear directions.

To investigate the dependence on the cohesive parameters, the total fracture energy or the initiation stress was changed in consecutive simulations, keeping the other parameters constant. The hydrostatic stress - volume ratio results obtained from this small parameter study are shown in Figure 15. Reducing the fracture energy reduces the slope of the curve after fracture initiation, see Figure 15a, and leads to an increased maximum volume. Changing the initiation stress on the other hand, yields a clear effect on the hydrostatic stress level at onset of volume growth, as shown in Figure 15b, while the maximum volume ratio immediately before unloading is hardly affected.

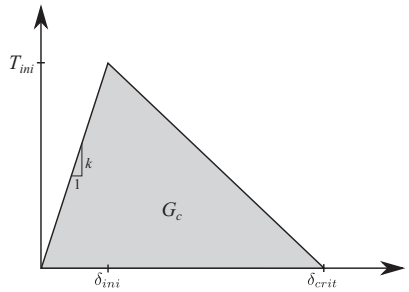

Figure 14: Illustration of the traction-separation law used for the cohesive zone.

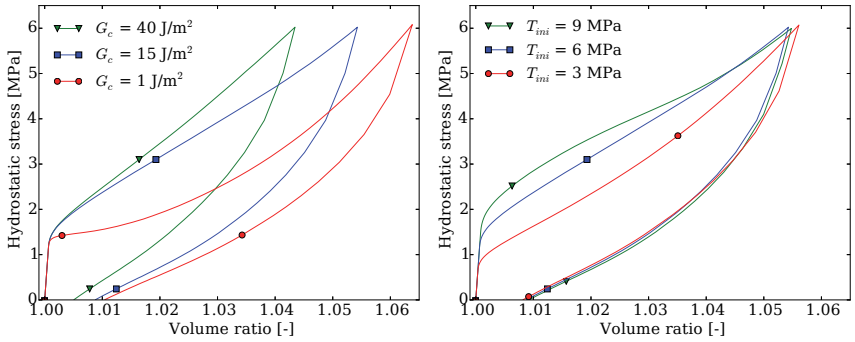

(a) (b)

Figure 15: Parameter study results for the properties of the cohesive zone in the unit cell model subject to tension, (a) dependence on fracture energy and (b) dependence on initiation stress.

5.5. HNBR vs FKM behaviour

To get an indication on the source of the difference in UT volumetric behaviour between the HNBR and FKM compounds, two different sets of material parameters, Model A and Model B, were defined to capture the qualitative response of the HNBR and FKM material respectively. From the parametric study in Section 5.4, it was indicated that the difference in volumetric behaviour between the two materials tested in Section 2 can be caused by an increased initiation stress and a reduced fracture energy on average for the cohesive zones in the HNBR compound compared with the FKM, in addition to fewer debonding particles in the HNBR compound leading to less volume growth. The parameters of Model B were set equal to the base model parameters of Section 5.4, while the value of f_0, D, T_{ini}, and G_c were changed for Model A with the following reasoning; f_0 was reduced to get a lower total volume increase in UT, D was reduced to get a slightly stiffer CAC behaviour, T_{ini} was increased to conform with the large stress level at onset of volume growth, while G_c was reduced to get a more compliant volume behaviour after matrix-particle decohesion. The values of the final parameters are listed in Table 2.

The volumetric behaviour in UT deformation of the unit cell models is shown in Figure 16a,

	f_0 [-]	D $[1/MPa]$	T_{ini} $[MPa]$	G_c $[J/m^2]$
Model A	0.018	0.012	30	9
Model B	0.05	0.015	6	15

Table 2: Model parameters changed to qualitatively capture the difference between HNBR and FKM behaviour.

while the hydrostatic stress - volume ratio obtained in the CAC simulations can be seen in Figure 16b. Qualitatively, both loading modes exhibit a good resemblance of the experimentally obtained results, showing a compliant and viscous behaviour in UT after a critical stress level is reached, while a stiff and purely elastic behaviour was obtained for the volumetric response in the confined axial compression simulations. The initial volumetric stiffness of the model is related to the bulk modulus of the matrix and particle material for both loading modes and is therefore nearly equal in all simulations. The qualitative difference between Model A and Model B is in good correspondence with the difference obtained comparing the HNBR and FKM compounds in the macroscopic tests of Section 2. This suggests that the variation in the observed behaviour for the HNBR and FKM stems from different adhesion properties between the matrix material and the filler particles for the two compounds. In addition, these results indicate that the matrix-particle decohesion and cavitation effects found in the in situ SEM experiments can be the explaining mechanisms for the loading mode dependent volume behaviour observed in the macroscopic tests.

The hysteresis loop of the volumetric response in UT, see Figure 16a, is caused by both viscous effects in the matrix material and the failure of the cohesive zone. This is demonstrated in Figure 17 where the prediction from Model B is compared with the result obtained using a purely hyperelastic matrix material, i.e. the constitutive model is reduced to the Arruda-Boyce hyperelastic potential by $S = A = 0$. While a larger total volume increase is seen for the purely hyperelastic model due the more compliant matrix, it is clear that a significant hysteresis loop can be caused solely by the failure of the cohesive zone. It can be noted that removing the viscous effects in the unit cell model would not have any consequence for the CAC response.

6. Summary and concluding remarks

In this study, HNBR and FKM compounds were tested experimentally in both uniaxial tension and confined axial compression. For the uniaxial tension tests, optical measurements were used to obtain the complete deformation field and thereby capturing the volume change. A moderate volume increase of 5 % was found for the HNBR material, while the FKM compound experienced a large volume change, with an increase of the volume by nearly 20 % for a hydrostatic stress of 6 MPa. In the confined axial compression tests however, very similar results were found between HNBR and FKM compounds, with about 6-7 % reduction of volume for a hydrostatic stress of 140 MPa. Comparing the results from the two loading modes, a large difference in the hydrostatic stress - volume ratio behaviour was observed. It was shown that this difference is not captured

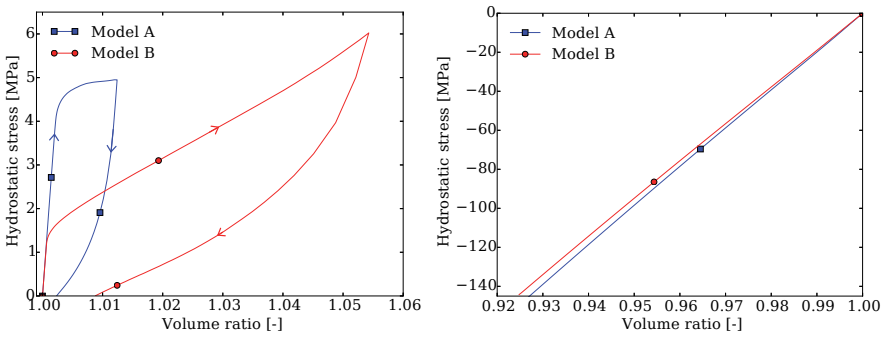

Figure 16: Results from unit cell simulations in (a) UT and (b) CAC, where Model A and B qualitatively represent HNBR and FKM, respectively.

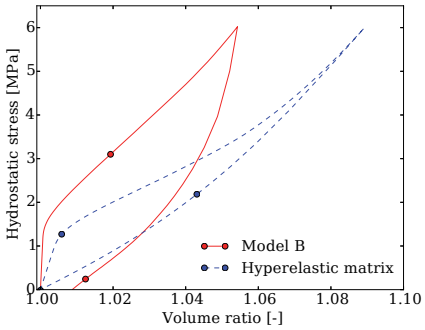

Figure 17: Illustration of the hysteresis loop in tension caused by the cohesive zone.

by available constitutive models for elastomeric materials. The mechanisms responsible for the volumetric behaviour are therefore studied further as a preparation for new micromechanically based constitutive modelling approaches.

To investigate the origin of the volume increase observed in uniaxial tension, an in situ SEM study was performed. Both materials were found to consist of a significant number of ZnO particles, which were shown to debond from the matrix material during tension, causing macroscopic volume growth. In addition, matrix cavitation was observed at the surface.

Based on the SEM experiments, the large difference in volumetric behaviour obtained between the two loading modes was studied by finite element simulations of an axisymmetric unit cell model. The simulations showed that the volumetric response obtained in the experiments could be qualitatively explained by the interaction between matrix material and filler particles, with decohesion occurring during uniaxial tension. In addition, by changing the parameters of the cohesive zone, the qualitative difference between the HNBR and the FKM material could be captured.

The findings of this study prepare for development of new constitutive models aimed at predicting the volumetric response of particle-filled elastomers exposed to various loading modes. Such models should incorporate the underlying physical mechanism of matrix-particle decohesion and possible matrix cavitation, and be able to capture the critical stress level and the viscous volume increase accompanying tension, at the same time as predicting a stiff and elastic volume response for loading modes governed by negative hydrostatic stresses.

Acknowledgements

The authors would like to acknowledge Aker Solutions AS for their funding of this research, the suppliers for providing test samples free of charge, Mr Trond Auestad for his assistance with the macroscopic experiments, and Mr Christian Oen Paulsen for his assistance during the SEM study.

References

[1] J. S. Bergström, M. C. Boyce, Constitutive modeling of the large strain time-dependent behavior of elastomers, Journal of the Mechanics and Physics of Solids 46 (1998) 931–954.

[2] C. Miehe, S. Göktepe, A micromacro approach to rubber-like materials. Part II: The micro-sphere model of finite rubber viscoelasticity, Journal of the Mechanics and Physics of Solids 53 (2005) 2231–2258.

[3] G. Ayoub, F. Zaïri, M. Naït-Abdelaziz, J. Gloaguen, G. Kridli, A visco-hyperelastic damage model for cyclic stress-softening, hysteresis and permanent set in rubber using the network alteration theory, International Journal of Plasticity 54 (2014) 19–33.

[4] A. Ilseng, B. H. Skallerud, A. H. Clausen, Tension behaviour of HNBR and FKM elastomers for a wide range of temperatures, Polymer Testing 49 (2016) 128–136.

[5] A. Ilseng, B. H. Skallerud, A. H. Clausen, Volumetric compression of HNBR and FKM elastomers, Constitutive Models for Rubber IX - Proceedings of the 9th European Conference on Constitutive Models for Rubbers, 2015, pp. 235–241.

[6] L. R. G. Treloar, The elasticity of a network of long-chain molecules-II, Transactions of the Faraday Society 39 (1943) 241–246.

[7] M. Mooney, A theory of large elastic deformation, Journal of Applied Physics 11 (1940) 582–592.

[8] R. S. Rivlin, Large Elastic Deformations of Isotropic Materials. IV. Further Developments of the General Theory, Philosophical Transactions of the Royal Society A: Mathematical, Physical and Engineering Sciences 241 (1948) 379–397.

[9] A. Ciesielski, An Introduction to Rubber Technology, Smithers Rapra Technology, 1999.

[10] A. N. Gent, B. Park, Failure processes in elastomers at or near a rigid spherical inclusion, Journal of Materials Science 19 (1984) 1947–1956.

[11] K. Cho, A. N. Gent, P. S. Lam, Internal fracture in an elastomer containing a rigid inclusion, Journal of Materials Science 22 (1987) 2899–2905.

[12] A. Gent, P. Lindley, Internal Rupture of Bonded Rubber Cylinders in Tension, Proceedings of the Royal Society A: Mathematical, Physical and Engineering Sciences 249 (1959) 195–205.

[13] A. Dorfmann, Stress softening of elastomers in hydrostatic tension, Acta Mechanica 165 (2003) 117–137.

[14] E. Bayraktar, N. Isac, K. Bessri, C. Bathias, Damage mechanisms in natural (NR) and synthetic rubber (SBR): Nucleation, growth and instability of the cavitation, Fatigue and Fracture of Engineering Materials and Structures 31 (2008) 184–196.

[15] O. Lopez-Pamies, M. I. Idiart, T. Nakamura, Cavitation in elastomeric solids: I - A defect-growth theory, Journal of the Mechanics and Physics of Solids 59 (2011) 1464–1487.

[16] W. L. Holt, A. T. McPherson, Change of volume of rubber on stretching : effets of time, elongation and temperature, Journal of Research for the National Bureau of Standards 17 (1936) 657–687.

[17] H. Jones, H. Yiengst, Dilatometer Studies of Pigment-Rubber Systems, Rubber Chem. Technol. 14 (1941) 113–124.

[18] R. Shuttleworth, Volume change measurements in the study of rubber-filler interactions, European Polymer Journal 4 (1968) 31–38.

[19] R. W. Penn, Volume Changes Accompanying the Extension of Rubber, Transactions of The Society of Rheology 14 (1970) 509.

[20] J. B. Le Cam, E. Toussaint, Volume Variation in Stretched Natural Rubber: Competition between Cavitation and Stress-Induced Crystallization, Macromolecules 41 (2008) 7579–7583.

[21] J.-B. Le Cam, E. Toussaint, Cyclic volume changes in rubber, Mechanics of Materials 41 (2009) 898–901.

[22] J. de Crevoisier, G. Besnard, Y. Merckel, H. Zhang, F. Vion-Loisel, J. Caillard, D. Berghezan, C. Creton, J. Diani, M. Brieu, F. Hild, S. Roux, Volume changes in a filled elastomer studied via digital image correlation, Polymer Testing 31 (2012) 663–670.

[23] S. Cantournet, K. Layouni, L. Laiarinandrasana, R. Piques, Experimental investigation and modelling of compressibility induced by damage in carbon black-reinforced natural rubber, Comptes Rendus Mécanique 342 (2014) 299–310.

[24] A. Needleman, Void Growth in an Elastic-Plastic Medium, Journal of Applied Mechanics 39 (1972) 964–970.

[25] V. Tvergaard, Influence of voids on shear band instabilities under plane strain conditions, International Journal of Fracture 17 (1981) 389–407.

[26] J. Faleskog, X. Gao, C. Fong Shih, Cell model for nonlinear fracture analysis - I. Micromechanics calibration, International Journal of Fracture 89 (1998) 355–373.

[27] L. E. B. Dæhli, T. Børvik, O. S. Hopperstad, Influence of loading path on ductile fracture of tensile specimens made from aluminium alloys, International Journal of Solids and Structures 88-89 (2016) 17–34.

[28] A. Steenbrink, E. Van Der Giessen, P. Wu, Void growth in glassy polymers, Journal of the Mechanics and Physics of Solids 45 (1997) 405–437.

[29] L. Cheng, T. Guo, Void interaction and coalescence in polymeric materials, International Journal of Solids and Structures 44 (2007) 1787–1808.

[30] A. S. Ognedal, A. H. Clausen, T. Berstad, T. Seelig, O. S. Hopperstad, Void nucleation and growth in mineral-filled PVC An experimental and numerical study, International Journal of Solids and Structures 51 (2014) 1494–1506.

[31] J. S. Bergström, M. C. Boyce, Mechanical Behavior of Particle Filled Elastomers, Rubber Chemistry and Technology 72 (1999) 633–656.

[32] ISO, 37:2011 Rubber, vulcanized or thermoplastic - Determination of tensile stress-strain properties, Tech. rep. (2011).

[33] E. Fagerholt, T. Børvik, O. Hopperstad, Measuring discontinuous displacement fields in cracked specimens using digital image correlation with mesh adaptation and crack-path optimization, Optics and Lasers in Engineering 51 (2013) 299–310.

[34] ISO, 815-1:2014 Rubber, vulcanized or thermoplastic – Determination of compression set – Part 1: At ambient or elevated temperatures, Tech. rep. (2014).

[35] C. Harris, M. Stephens, A combined corner and edge detector, in: Alvey vision conference, Vol. 15, Manchester, UK, 1988, p. 50.

[36] M. C. Boyce, E. M. Arruda, Constitutive Models of Rubber Elasticity: A Review, Rubber Chemistry and Technology 73 (2000) 504–523.

[37] S. Doll, K. Schweizerhof, On the Development of Volumetric Strain Energy Functions, Journal of Applied

Mechanics 67 (1999) 17–21.

[38] J. E. Bischoff, E. M. Arruda, K. Grosh, A new constitutive model for the compressibility of elastomers at finite deformations, Rubber Chemistry and Technology 74 (2001) 541–559.

[39] T. Sussman, K.-J. Bathe, A finite element formulation for nonlinear incompressible elastic and inelastic analysis, Computers and Structures 26 (1987) 357–409.

[40] J. C. Simo, C. Miehe, Associative coupled thermoplasticity at finite strains: Formulation, numerical analysis and implementation, Computer Methods in Applied Mechanics and Engineering 98 (1992) 41–104.

[41] H. Hencky, The Elastic Behavior of Vulcanized Rubber, Rubber Chemistry and Technology 6 (1933) 217–224.

[42] S. Reese, S. Govindjee, A theory of finite viscoelasticity and numerical aspects, International Journal of Solids and Structures 35 (1998) 3455–3482.

[43] M. Karlsen, J. Hjelen, Ø. Grong, G. Rørvik, R. Chiron, U. Schubert, E. Nilsen, SEM/EBSD based in situ studies of deformation induced phase transformations in supermartensitic stainless steels, Materials Science and Technology 24 (2008) 64–72.

[44] S. van der Walt, J. L. Schönberger, J. Nunez-Iglesias, F. Boulogne, J. D. Warner, N. Yager, E. Gouillart, T. Yu, scikit-image: image processing in Python., PeerJ 2 (2014) e453.

[45] N. Otsu, Threshold selection method from gray-level histograms, IEEE Trans Syst Man Cybern SMC-9 (1979) 62–66.

[46] J. J. Williams, J. Segurado, J. LLorca, N. Chawla, Three dimensional (3D) microstructure-based modeling of interfacial decohesion in particle reinforced metal matrix composites, Materials Science and Engineering A 557 (2012) 113–118.

[47] L. Laiarinandrasana, T. F. Morgeneyer, H. Proudhon, C. Regrain, Damage of semicrystalline polyamide 6 assessed by 3D X-ray tomography: From microstructural evolution to constitutive modeling, Journal of Polymer Science, Part B: Polymer Physics 48 (2010) 1516–1525.

[48] H. A. Cayzac, K. Saï, L. Laiarinandrasana, Damage based constitutive relationships in semi-crystalline polymer by using multi-mechanisms model, International Journal of Plasticity 51 (2013) 47–64.

[49] Abaqus, 6.13-1, Dassault Systèmes, 2013.

[50] S. Ghosh, Y. Ling, B. Majumdar, R. Kim, Interfacial debonding analysis in multiple fiber reinforced composites, Mechanics of Materials 32 (2000) 561–591.

[51] P. A. Toulemonde, J. Diani, P. Gilormini, N. Desgardin, On the account of a cohesive interface for modeling the behavior until break of highly filled elastomers, Mechanics of Materials 93 (2016) 124–133.

[52] Abaqus Theory Guide 6.13, Dassault Systèmes, 2013.

[53] C. Q. Chen, Y. Shi, Y. S. Zhang, J. Zhu, Y. J. Yan, Size Dependence of Young's Modulus in ZnO Nanowires, Physical Review Letters 96 (2006) 75505.

[54] J. Segurado, J. Llorca, A computational micromechanics study of the effect of interface decohesion on the mechanical behavior of composites, Acta Materialia 53 (2005) 4931–4942.

[55] H. M. Inglis, P. H. Geubelle, K. Matous, H. Tan, Y. Huang, Cohesive modeling of dewetting in particulate composites: micromechanics vs. multiscale finite element analysis, Mechanics of Materials 39 (2007) 580–595.

Paper III

Arne Ilseng, Bjørn H. Skallerud, Arild H. Clausen

Volume growth during uniaxial tension of particle-filled elastomers at ambient to low temperatures – Experiments and modelling

To be submitted for journal publication

Paper III

Volume growth during uniaxial tension of particle-filled elastomers at ambient to low temperatures – Experiments and modelling

Arne Ilseng[a,b,*], Bjørn H. Skallerud[a], Arild H. Clausen[a]

[a] *Department of Structural Engineering, NTNU, Norwegian University of Science and Technology, 7491 Trondheim, Norway*
[b] *Aker Solutions AS, 3408 Tranby, Norway*

Abstract

In this article, the volumetric deformation accompanying uniaxial tension of particle-filled elastomeric materials is studied. An experimental set-up, enabling full field deformation measurements at low temperatures, is outlined and data on the volume response in uniaxial tension of two HNBR and one FKM compounds at temperatures from −18 to 23 °C are reported. The volumetric deformation was found to increase with reduced temperature for all compounds. To explain the observed dilatation, in situ scanning electron microscopy was used to inspect matrix-particle debonding occurring at the surface of the materials. A new constitutive model, combining the Bergström-Boyce visco-hyperelastic formulation with a Gurson flow potential function is outlined to account for the observed debonding effects in a numerical framework. The new model is shown to give a good prediction of the experimental data, including the volumetric response, for the FKM compound at all temperature levels.

Keywords: Elastomers, Volumetric deformation, Low temperatures, SEM, Constitutive modelling, DIC

1. Introduction

Particle-filled elastomeric materials are applied in a range of industries where they can be exposed to large temperature variations, like automotive, aerospace, and oil and gas. For subsea oil and gas equipment, elastomeric seals are essential for correct operation. Therefore, to prevent failure of such seals during service, strict and time consuming qualification testing, possibly involving temperatures from −18 to 150 °C and pressures up to 140 MPa [1], must be carried out prior to installation. The lead-time and man-hour cost of obtaining a combination of elastomeric material and seal design that would pass the qualification tests could be greatly reduced by introducing numerical analyses, like finite element simulations, into the design process. For such analyses to be predictive and thereby cost saving, increased understanding of the underlying mechanisms occurring in elastomeric materials at various temperature and pressure levels and improved constitutive models that capture these effects are of utmost importance.

*arne.ilseng@ntnu.no

A common presumption for elastomeric material behaviour is that their deformation is fully or nearly isochoric. However, it was early shown by Gent and Park [2] and Cho et al. [3] that the inclusion of stiff filler particles, as done in nearly all industrially applied elastomer compounds, could give rise to matrix-particle debonding and subsequent volume growth. In the later years, the advances of optical measurement techniques, like digital image correlation (DIC), have facilitated accurate quantitative measurements of the possible volume growth occurring when filled elastomers are loaded in tension. Le Cam and Toussaint [4] measured the volume change accompanying uniaxial tension of filled and unfilled natural rubber specimens by the use of DIC at one surface and an assumption of material isotropy. They found a significantly larger volume growth to occur in the filled specimens. The same authors also reported significant volume growth in a filled SBR elastomer by the same experimental procedure [5]. de Crevoisier et al. [6] used two cameras for DIC measurements to capture the complete strain field during uniaxial tension of a filled SBR material, and thereby avoiding the isotropy assumption when calculating the volume change. During cyclic deformation, they found the volume growth of each cycle to start when the longitudinal strain exceeded the previously obtained maximum deformation. Cantournet et al. [7] reported the volume change of a particle filled natural rubber to be strongly dependent on deformation mode. For confined and hydrostatic compression, a stiff volumetric response was reported, while matrix-particle decohesion around ZnO particles gave a more compliant volumetric behaviour in uniaxial tension. For a deformation mode dominated by hydrostatic tension on the other hand, voids were reported to nucleate unrelated to filler particle locations. Such loading mode dependence was later echoed by Ilseng et al. [8], studying the relation between the macroscopic volume response in uniaxial tension and confined axial compression experiments and the underlying mechanism of matrix-particle decohesion. While the effect of temperature on the viscoelastic behaviour of elastomers is well studied in the literature [9, 10, 11, 12], the volume growth of filled elastomers exposed to uniaxial tension loading at different temperature levels has not yet been studied.

Although experimental evidence shows that particle-filled elastomers might yield large volume variations in certain loading modes, most constitutive models for such materials available in the literature neglect this effect. For rate independent elastomeric behaviour, a range of different hyperelastic potential functions exists [13, 14, 15, 16]. In these models, a small volumetric contribution is added to the isochoric potential to include slight compressibility and ensure numerical stability. To also account for the viscous features of elastomeric behaviour, a number of models combining hyperelastic springs and strain-rate dependent dashpots have been proposed [17, 18, 19, 20], with the visco-hyperelastic model of Bergström and Boyce [19], combining the eight-chain strain energy potential [16] with a non-linear viscous formulation, being the most extensively applied. The stiff and fully elastic volumetric response observed in hydrostatic compression experiments [21, 22, 23] normally dictates the volumetric behaviour in these models, while the possible volume growth in tension due to matrix-particle decohesion is neglected. A few authors have proposed constitutive

models that account for large volume growth in elastomeric materials [24, 25, 26]. Yet, the focus of these studies was on rate-independent theoretical considerations of cavitation growth for loading states of large triaxial stresses, and matrix-particle debonding during uniaxial tension was not considered.

While constitutive models that capture the effects of matrix-particle decohesion and cavitation growth on the macroscopic response have gained limited attention in studies of elastomeric materials, it is an important area of research for ductile metallic materials. In that field, an essential piece of work, dealing with yielding of a rigid-perfectly plastic matrix containing a spherical void, was put forward by Gurson [27]. The Gurson model has subsequently been modified or extended in multiple works concerned with metallic materials [28, 29, 30, 31, 32], and there are also some applications to thermoplastic polymers [33, 34, 35]. To the best of the authors' knowledge, the Gurson formulation has not yet been applied to describe the volumetric behaviour of elastomeric compounds.

In the present work, a new experimental set-up that enables DIC measurements of the complete deformation field at low temperatures is outlined. Novel data on the volume growth accompanying tension of HNBR and FKM materials are obtained for a temperature range from -18 to 23 °C. An in situ scanning electron microscopy (SEM) study was performed at room temperature to investigate the matrix-particle debonding accompanying tension of these materials. To incorporate the volume growth in a constitutive framework, a new model is proposed by modifying the Bergström-Boyce model [19] with the use of a Gurson flow potential function [27] for the viscous behaviour.

The article is organized as follows: In the following section the set-up and experimental results for the macroscopic tension tests are outlined. Section 3 presents the set-up and the results obtained for the in situ SEM investigation. Thereafter, in Section 4, a new constitutive model including the observed viscous volume growth caused by matrix-particle debonding is presented and compared with the macroscopic experimental results. Concluding remarks are given in Section 5.

2. Macroscopic experiments

2.1. Materials

Two different HNBR compounds and one FKM material are studied herein and are in the following denoted HNBR1, HNBR2, and FKM. All three compounds are commonly used for sealing applications in the oil and gas industry, and were delivered from the suppliers as dumbbell shaped specimens die stamped from 2 mm thick sheets. The dimensions were in line with ISO 37 Type–1 and Type–2 [36]. The different materials, their dumbbell geometry, the measured pre-testing density, and the temperature range and hardness values provided by the suppliers are listed in Table 1. According to the suppliers, the lower bound of the temperature range indicates the temperature for which the materials have fully transitioned into the glassy region.

Table 1: Tested materials, their geometries and properties

Material	Geometry	Density	Temperature range	Hardness
HNBR1	ISO 37 Type 1	1.29 g/cm^3	−35 to 150 °C	86 shore A
HNBR2	ISO 37 Type 2	1.19 g/cm^3	−29 to 160 °C	89 IRHD
FKM	ISO 37 Type 2	1.77 g/cm^3	−40 to 200 °C	89 IRHD

2.2. Set-up

The macroscopic tension experiments were performed using an Instron 5944 testing machine with a 2 kN load cell. The specimens were loaded to a maximum machine displacement of 40 mm, and then directly unloaded until zero force was measured by the load cell, all at a deformation rate of 1 mm/s. The same deformation procedure was applied for all temperature levels and materials, and a new specimen was used for each test. The testing temperatures were set to −18, 0 and 23 °C. Two tests were run for each combination of material and temperature, with the duplicates showing consistency of the reported results.

A custom-built temperature chamber, made of 10 mm thick transparent polycarbonate (PC) plates and connected to a supply of liquid nitrogen (LN_2), was used to obtain the low temperature testing conditions. Stable testing temperatures were achieved by controlling the flow of LN_2 using a PID regulator. To avoid icing and condensation on the chamber walls, a tabletop fan was used to ensure sufficient air circulation around the chamber. The temperature of the specimen surface was monitored throughout the deformation cycle by a FLIR SC7000 infrared camera, calibrated for temperatures down to −20 °C. A rectangular hole was made in the chamber to obtain an unobstructed view between the infrared camera and the specimen. For optical deformation measurements, two Prosilica GC2450 CCD cameras were placed outside of the transparent chamber and logged images of the wide and narrow surface of the specimen at a frame rate of 7 Hz. The materials tested here were shown by Ilseng et al. [8] to behave transversely anisotropic, and the dual camera set-up is therefore needed to obtain quantitative volume measurements. The experimental set-up is illustrated in Figure 1a, where the temperature chamber, specimen n and n+1, the two CCD cameras, the infrared camera, the tabletop fan, and the LN_2 container can be seen.

To use DIC to calculate the local deformations, a grey scale speckle pattern must be applied in the gauge section of the specimens. Ilseng et al. [12] found that the traditional use of black and white spray paint to obtain this speckle pattern was unsuitable at low temperature levels, due to cracking of the paint during deformation. As an alternative, a thin layer of a Molycote 33 Medium low temperature grease was applied to the specimens, and icing sugar was sprinkled in the greased area. A sieve with a wire mesh size of 75 µm was used to ensure a fine-grained and evenly distributed layer of the icing sugar. Opposed to traditional spray painting, the grease and icing sugar speckle pattern did not experience cracking during deformation at low temperatures. The use of the PC chamber and a grease-and-powder speckle pattern was shown by Johnsen et al. [37]

to yield similar results as tests with traditional spray painted speckle pattern and no temperature chamber.

The frames captured by the two cameras were post-processed using the in house DIC software *eCorr* [38]. An example of reference and deformed configuration captured with Camera 1 for a test of the HNBR1 material at $-18\,^{\circ}\mathrm{C}$ is seen in Figure 1b. For the reference frame, the initial DIC mesh is shown; while for the deformed configuration, a fringe plot of the first principal logarithmic strain is included. The logarithmic element strains in the principal directions ϵ_i^e were calculated for each element in the DIC mesh by *eCorr*, with $i = 1$ denoting the longitudinal direction and e representing the element number, and corresponding stretch values were found through $\lambda_i^e = \exp[\epsilon_i^e]$. A representative principal stretch value was obtained by calculating the mean stretch over all n elements as

$$\lambda_i = \frac{1}{n}\sum_{e=1}^{n} \lambda_i^e \tag{1}$$

and a representative logarithmic strain value was found by $\epsilon_i = \log \lambda_i$. There was a good agreement between the representative longitudinal logarithmic strain ϵ_1 found from the two independent yet synchronized cameras [8]. Using the three representative principal stretch ratios λ_i, the volume ratio J was calculated as

$$J = \lambda_1 \lambda_2 \lambda_3 \tag{2}$$

while the longitudinal Cauchy stress was found from

$$\sigma_1 = \frac{F}{A} = \frac{F}{\lambda_2 \lambda_3 A_0} \tag{3}$$

where F is the force measured by the load cell, A the current cross sectional area, A_0 the initial cross sectional area, and λ_2 and λ_3 are the transverse stretch ratios. For the uniaxial tension tests ($\sigma_2 = \sigma_3 = 0$), the hydrostatic stress is defined as

$$\sigma_H = \frac{\sigma_1}{3} \tag{4}$$

Finite element simulations of the thermal conditioning process, using the material parameters and the numerical procedure outlined by Ilseng et al. [12], showed that 8 minutes of thermal conditioning should be sufficient to cool the centre of the sample from room temperature to below $-17.5\,^{\circ}\mathrm{C}$. During the experimental testing, specimen $n{+}1$ was placed in the temperature chamber at the same time as sample n was mounted in the testing machine for cooling. A 10-minute conditioning period was included between mounting a sample in the machine and the start of the deformation cycle. During this period, the machine was set to retain zero force in the load cell to account for thermal contraction of the specimen. Before the first test at a new temperature level, a 30-minute tempering period was included to ensure sufficient cooling of the steel grips of the testing machine.

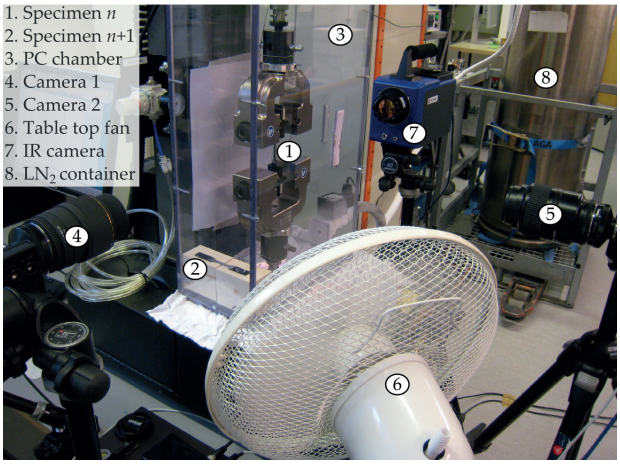

(a)

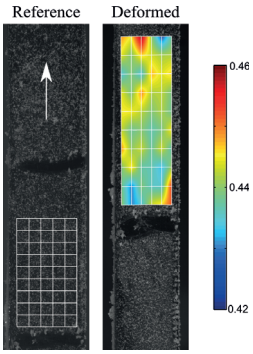

(b)

Figure 1: (a) Experimental set-up used in the macroscopic tension experiments, (b) DIC frames from Camera 1 for a test on HNBR1 at $-18\,^{\circ}\mathrm{C}$, the white arrow on the reference configuration indicates tension direction, while the black horizontal lines in the speckle pattern were used to match the location of the mesh between images from Camera 1 and Camera 2. The fringe plot indicates the value of the first principal logarithmic strain.

2.3. Results

2.3.1. Stress - strain

The longitudinal Cauchy stress - longitudinal logarithmic strain behaviour of the three materials is shown in Figure 2. The slight wobbling in the loading curve for the HNBR2 and the FKM materials at −18 °C coincided with the injection of liquid nitrogen into the chamber and was likely caused by small temperature variations in the specimens. As expected, a clear increase of stiffness and strength for the loading process can be seen to take place as the temperature is reduced. During unloading however, the temperature level had limited influence on the material response. The significant dip in stress level seen to occur at a strain level of about 0.4 in the HNBR1 material at low temperatures was previously discussed by Ilseng et al. [12], where matrix-particle debonding with low fracture energy was suggested as a plausible physical mechanism.

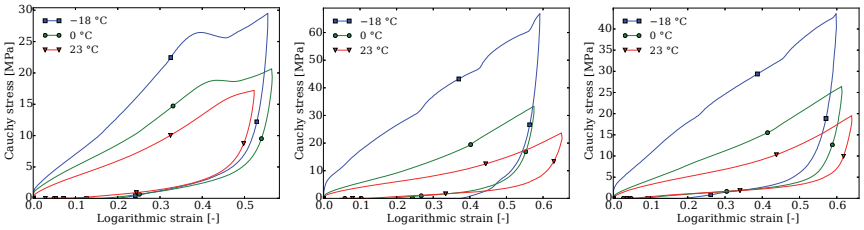

(a) (b) (c)

Figure 2: Cauchy stress - logarithmic strain data for all temperatures (a) HNBR1, (b) HNBR2, and (c) FKM.

2.3.2. Volume growth

The volume ratio vs longitudinal logarithmic strain data are shown for all materials and temperatures in Figure 3. It appears that a significant increase of volume is present for all three compounds, although somewhat more modest for the HNBR2 material than for the two others. A clear trend is that all materials increase their volumetric deformation as the temperature is reduced. In addition, for the low strain regime the volume ratio is close to unity, before a clear volume increase is seen when a critical strain level is reached. This behaviour is in line with a matrix-particle debonding theory, where a certain amount of strain/stress would be needed for the bonding between the matrix and the particles to break, and thereby the volume to increase. The onset of volume growth for the HNBR1 material, as illustrated in Figure 3a, is observed to coincide with the stress dip seen in Figure 2a. In addition, a clear loop in the loading-unloading behaviour can be seen for this compound, with the volume ratio being clearly larger for the same strain level during unloading compared with loading. Further, the volume growth of the HNBR1 material is strongly temperature dependent, with the maximum volume variation being only a few percent at 23 °C, while more than 20 % volume growth was obtained for the test at −18 °C. The results for the HNBR2 material presented in Figure 3b display virtually no volume change at room

temperature. However, as the temperature decreased, a clear volume increase can be observed in the large deformation regime. In the FKM results on the other hand, presented in Figure 3c, more than 20 % volume increase is seen for the test at 23 °C. The volume ratio - logarithmic strain response is relatively similar for the 23 and 0 °C tests, while the volume change at −18 °C is clearly larger, with a maximum value of 28 % volume growth.

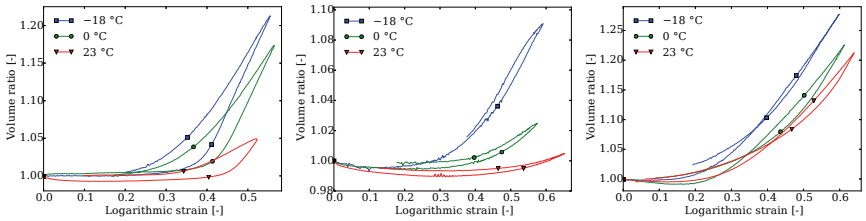

(a) (b) (c)

Figure 3: Volume ratio - logarithmic strain data for all three temperatures (a) HNBR1, (b) HNBR2, and (c) FKM.

To obtain a continuum based constitutive model of the volume growth in elastomers, the relation between the hydrostatic stress and the volume ratio, as shown in Figure 4, is important. For all materials, a critical stress level is needed before the volume growth starts. This critical stress level appears to increase with decreasing temperature, while the slope of the curves after the volume increase has started is nearly equal for all temperature levels. A clear hysteresis loop is apparent for all materials at all temperatures, indicating a viscous volumetric behaviour. As the volume returns to its initial value for the 0 and 23 °C tests, the process is assumed to be viscoelastic. For the HNBR1 material in Figure 4a, there is a plateau level where the volume increases significantly for a nearly constant hydrostatic stress value. Compared to the loading process, the response during unloading is less sensitive to the temperature level, as illustrated by the FKM material at 0 and 23 °C for which the unloading curves almost perfectly coincide.

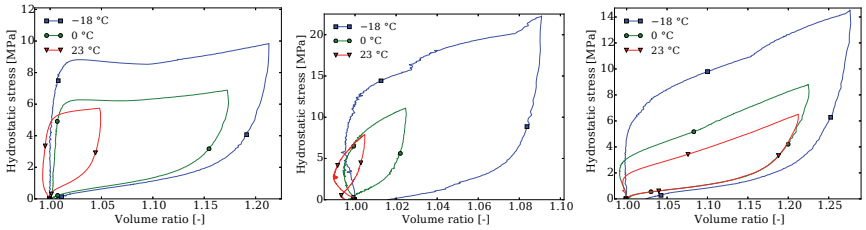

(a) (b) (c)

Figure 4: Hydrostatic stress - volume ratio data for all three temperatures (a) HNBR1, (b) HNBR2, and (c) FKM.

2.3.3. Temperature change

The maximum temperature increase in the deformation cycle, measured at the surface of the materials by the infrared camera, is shown for all tests in Figure 5. For all materials, the temperature change increased at colder testing conditions, as to be expected from the enlarged hysteresis loops obtained at low temperatures in the stress - strain plots of Figure 2. The high stress levels at reduced temperatures may also explain why the largest increase of temperature occurs at −18 °C. The greatest temperature change was found for the HNBR2 material tested at −18 °C, which experienced a temperature increase of 9 °C at its surface.

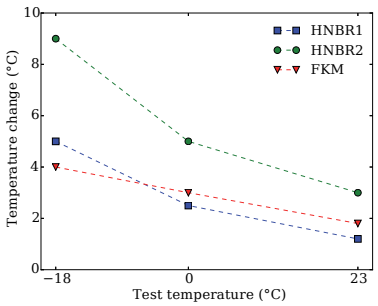

Figure 5: Maximum temperature increase at the surface of the samples during deformation for all materials and test temperatures.

3. In situ SEM experiments

3.1. Motivation

A micromechanical theory for the large volume growth accompanying tension of the materials at hand is that debonding between the matrix material and filler particles leads to cavities and thereby macroscopic volume growth. If this hypothesis is correct, micrographs of such debonding should be possible to obtain by in situ SEM. Therefore, the two compounds HNBR1 and FKM, showing clear volume growth for the macroscopic tension tests at room temperature, were investigated by in situ SEM. The full study and its results are discussed in length by Ilseng et al. [8].

3.2. Set-up

A purpose-built tension rig [39] was placed on the sample board of a Zeiss Gemini Ultra 55 Limited Edition microscope to obtain the in situ micrographs. An illustration of the tension rig can be seen in Figure 6a. Small tension specimens, having dimensions in line with the sketch in Figure 6b, were cut from the ISO geometry specimens delivered by the suppliers. The materials were tested at room temperature and deformed at a low strain rate to a nominal stretch of 2. The stretched specimens were studied in the microscope by a random-walk procedure, and micrographs with a resolution of 3072×2072 pixels were captured at locations of interest.

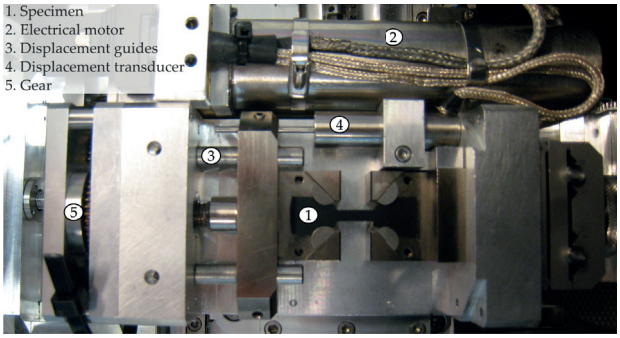

(a)

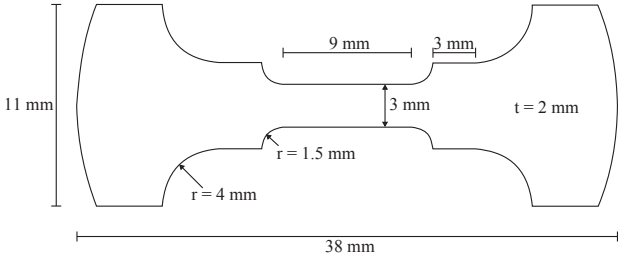

(b)

Figure 6: Setup for the in situ SEM study, (a) test specimen in tension rig, and (b) geometry of in situ specimens cut from the ISO dimension samples.

3.3. Results

For the HNBR1 material, debonding between the matrix material and particle inclusions was observed at multiple locations, as illustrated by the two marked particles in Figure 7a. Energy-dispersive X-ray spectroscopy (EDS) suggested that the highly reflecting inclusions in the HNBR1 compound are ZnO particles. For the FKM compound however, it was found that the conductive properties of the material were challenging in the deformed configuration. Therefore, only one occurrence of matrix-particle debonding could be found, as illustrated in Figure 7b. However, matrix-particle decohesion seems to be a viable theory for the volumetric growth that accompany uniaxial tension of the particle-filled elastomers.

4. Constitutive modelling

4.1. Preliminaries

From the experimental results presented in Section 2 and 3 it is clear that significant volume increase, partly or solely caused by matrix-particle debonding, can accompany tension of particle-filled elastomeric materials and that this volume growth gets more pronounced as the temperature is reduced. It was also shown that a threshold value for the hydrostatic stress has to be reached before any significant increase of volume takes place. In addition, a significant hysteresis in the hydrostatic

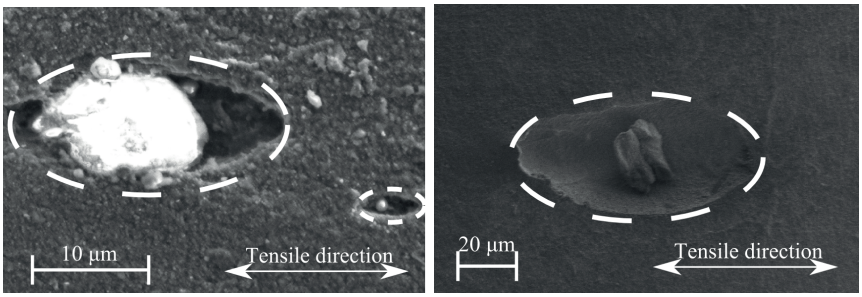

(a) (b)

Figure 7: Debonding observed at a nominal longitudinal stretch of two for (a) HNBR1 and (b) FKM. Cavities are indicated by dashed white lines.

stress - volume ration behaviour was observed. In this section, a new constitutive model, combining the visco-hyperelastic Bergström-Boyce model [19] with the Gurson flow potential function [27], is outlined to capture the experimentally observed behaviour. For the constitutive modelling presented, an isotropic material behaviour is assumed.

To introduce the notation used in this section, a brief recapitulation of important continuum mechanical concepts is included. For a thorough review, the reader is referred to the textbooks by Holzapfel [40] or Belytschko et al. [41]. The main kinematic variable of continuum mechanics is the deformation gradient $\mathbf{F}$, and it is defined by

$$\mathbf{F} = \frac{\partial \boldsymbol{x}}{\partial \boldsymbol{X}} \tag{5}$$

where $\boldsymbol{x}$ is a particle position in the current configuration, and $\boldsymbol{X}$ is the position of the same particle in the reference configuration. Further, the left and right Cauchy-Green deformation tensors, $\mathbf{b}$ and $\mathbf{C}$ respectively, are defined as

$$\mathbf{b} = \mathbf{F}\mathbf{F}^T, \quad \mathbf{C} = \mathbf{F}^T\mathbf{F} \tag{6}$$

while the volume ratio J can be found from

$$J = \det\mathbf{F} \tag{7}$$

Purely distortional parts of the Cauchy-Green deformation tensors are found through

$$\mathbf{b}^* = J^{-2/3}\mathbf{b}, \quad \mathbf{C}^* = J^{-2/3}\mathbf{C} \tag{8}$$

The deviatoric part of a tensor $\mathbf{A}$ is calculated as

$$\mathbf{A}' = \mathbf{A} - \left(\frac{1}{3}\mathrm{tr}\mathbf{A}\right)\mathbf{I} \tag{9}$$

where $\mathbf{I}$ is the second order unit tensor. The first invariant of the full and the distortional left and right Cauchy-Green tensors are

$$I_1 = \mathrm{tr}\mathbf{b} = \mathrm{tr}\mathbf{C}, \quad I_1^* = \mathrm{tr}\mathbf{b}^* = \mathrm{tr}\mathbf{C}^* \tag{10}$$

4.2. Model formulation

The model consists of two parallel parts having a hyperelastic spring in Part A and a non-linear viscous dashpot in series with a hyperelastic spring in Part B, as illustrated by the rheological 1D representation in Figure 8. The deformation gradient of Part A and Part B is by definition equal to the total deformation gradient

$$\mathbf{F} = \mathbf{F}_{\mathrm{A}} = \mathbf{F}_{\mathrm{B}} \tag{11}$$

while the total Cauchy stress is the sum of the stresses in Part A and Part B

$$\boldsymbol{\sigma} = \boldsymbol{\sigma}_{\mathrm{A}} + \boldsymbol{\sigma}_{\mathrm{B}} \tag{12}$$

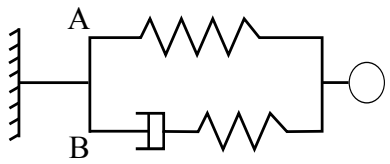

Figure 8: 1D rheological representation of the constitutive model.

4.2.1. Part A

As in the Bergström-Boyce model [19], the elastic spring in Part A is governed by the 8-chain Arruda-Boyce potential function [16] for the isochoric part combined with a volumetric potential function as used by Simo and Miehe [42]. The Cauchy stress tensor then reads

$$\boldsymbol{\sigma}_{\mathrm{A}} = \frac{\mu_{\mathrm{A}}\lambda_L}{3J_{\mathrm{A}}\lambda_{\mathrm{A}}^*}\mathcal{L}^{-1}\left(\frac{\lambda_A^*}{\lambda_L}\right)(\mathbf{b}_{\mathrm{A}}^*)' + \frac{\kappa_{\mathrm{A}}}{2}\left(J_{\mathrm{A}} - \frac{1}{J_{\mathrm{A}}}\right)\mathbf{I} \tag{13}$$

where μ_{A} is the effective shear modulus, κ_{A} the effective bulk modulus, λ_L the locking stretch, J_A is the volume ratio of Part A found from $J_A = \det\mathbf{F}_{\mathrm{A}}$, and $\mathcal{L}^{-1}$ is the inverse of the Langevin function, defined by $\mathcal{L}(x) = \coth(x) - 1/x$. For the Fortran implementation of the model, the inverse Langevin function was solved by Newton's method, using a Padé approximation [43] for the initial guess. The effective stretch λ_{A}^* is defined as

$$\lambda_{\mathrm{A}}^* = \sqrt{\frac{1}{3}\mathrm{tr}\mathbf{b}_{\mathrm{A}}^*} \tag{14}$$

4.2.2. Part B

Kinematics. The deformation gradient of Part B is decomposed multiplicatively in an elastic and a viscous part [44], as illustrated in Figure 9

$$\mathbf{F}_{\mathrm{B}} = \mathbf{F}_{\mathrm{B}}^e\mathbf{F}_{\mathrm{B}}^v \tag{15}$$

This leads to a multiplicative split in elastic and viscous parts also for the volume ratio of Part B

$$J_{\mathrm{B}} = J_{\mathrm{B}}^e J_{\mathrm{B}}^v \tag{16}$$

The viscous velocity gradient defined on the intermediate configuration $\tilde{\Omega}$, see Figure 9, can be found as

$$\tilde{\mathbf{L}}_{\mathrm{B}}^{v} = \dot{\mathbf{F}}_{\mathrm{B}}^{v} \left(\mathbf{F}_{\mathrm{B}}^{v}\right)^{-1} = \tilde{\mathbf{D}}_{\mathrm{B}}^{v} + \tilde{\mathbf{W}}_{\mathrm{B}}^{v} \tag{17}$$

where $\tilde{\mathbf{D}}_{\mathrm{B}}^{v}$ is the symmetric rate-of-deformation tensor and $\tilde{\mathbf{W}}_{\mathrm{B}}^{v}$ the anti-symmetric spin tensor. Due to material isotropy, one can obtain that $\tilde{\mathbf{W}}_{\mathrm{B}}^{v} = 0$ and a relation for $\tilde{\mathbf{D}}_{\mathrm{B}}^{v}$ can be defined

$$\tilde{\mathbf{D}}_{\mathrm{B}}^{v} = \dot{\gamma}_{\mathrm{B}} \mathbf{N}_{\mathrm{B}}^{v} \tag{18}$$

where a constitutive equation is needed for the viscous multiplier $\dot{\gamma}_{\mathrm{B}}$. The direction of the viscous deformation is denoted $\mathbf{N}_{\mathrm{B}}^{v}$, and can be found as the gradient of a flow potential function g according to

$$\mathbf{N}_{\mathrm{B}}^{v} = \frac{\partial g}{\partial \tilde{\mathbf{\Sigma}}_{\mathrm{B}}} \tag{19}$$

where $\tilde{\mathbf{\Sigma}}_{\mathrm{B}}$ is the Mandel stress tensor, defined on the intermediate configuration and related to the Cauchy stress $\boldsymbol{\sigma}_{\mathrm{B}}$ by

$$\tilde{\mathbf{\Sigma}}_{\mathrm{B}} = J_{\mathrm{B}}^{e} \left(\mathbf{F}_{\mathrm{B}}^{e}\right)^{T} \boldsymbol{\sigma}_{\mathrm{B}} \left(\mathbf{F}_{\mathrm{B}}^{e}\right)^{-T} \tag{20}$$

By combining Equation 17 and 18, a rate equation for the viscous deformation gradient can be obtained as

$$\dot{\mathbf{F}}_{\mathrm{B}}^{v} = \dot{\gamma}_{\mathrm{B}} \mathbf{N}_{\mathrm{B}}^{v} \mathbf{F}_{\mathrm{B}}^{v} \tag{21}$$

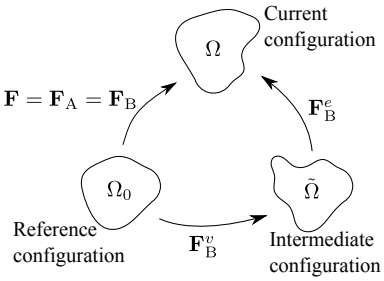

Figure 9: Illustration of the multiplicative decomposition of the deformation gradient.

Elastic spring. For the spring in Part B, an eight-chain model formulated on the intermediate configuration $\tilde{\Omega}$ is used

$$\tilde{\mathbf{\Sigma}}_{\mathrm{B}} = \frac{\mu_{\mathrm{B}} \lambda_L}{3\lambda_{\mathrm{B}}^{e*}} \mathcal{L}^{-1}\left(\frac{\lambda_{\mathrm{B}}^{e*}}{\lambda_L}\right) \left(\tilde{\mathbf{C}}_{\mathrm{B}}^{e*}\right)' + \frac{\kappa_{\mathrm{B}}}{2}\left(\left(J_{\mathrm{B}}^{e}\right)^2 - 1\right)\mathbf{I} \tag{22}$$

where μ_B is the shear modulus of the spring, κ_B is the bulk modulus, and $\lambda_{\mathrm{B}}^{e*} = \sqrt{\frac{\mathrm{tr}\mathbf{C}_{\mathrm{B}}^{e*}}{3}}$.

Dashpot. The constitutive relation for the viscous multiplier $\dot{\gamma}_{\mathrm{B}}$ is defined as

$$\dot{\gamma}_{\mathrm{B}} = \dot{\gamma}_{\mathrm{B}}^{0} \left(\frac{\sqrt{\tilde{\boldsymbol{\Sigma}}_{\mathrm{B}} : \tilde{\boldsymbol{\Sigma}}_{\mathrm{B}}}}{f_v \tau} \right)^{m} \tag{23}$$

where $\dot{\gamma}_{\mathrm{B}}^{0}$ is included to ensure dimensional consistency, while τ represents a scaling stress. The term f_v is introduced to incorporate the difference in the strain rate sensitivity between loading and unloading and is defined as [45]

$$f_v = 1 + \alpha \boldsymbol{\epsilon} : \boldsymbol{\epsilon}^{e} \tag{24}$$

where α is a material parameter, $\boldsymbol{\epsilon} = \ln[\mathbf{V}]$, and $\boldsymbol{\epsilon}^{e} = \ln[\mathbf{V}^{e}]$, with $\mathbf{V}$ being the left stretch tensor defined as $\mathbf{V}^2 = \mathbf{b}$, and correspondingly $(\mathbf{V}^{e})^2 = \mathbf{b}_{\mathrm{B}}^{e}$. The exponent m in equation 23 is a material parameter that, since f_v theoretically can be negative, is set to be an even number to ensure thermodynamic consistency, i.e. $\dot{\gamma}_{\mathrm{B}} \geq 0$, for any deformation. It can be noted that the full Mandel stress tensor is used in Equation 23, as opposed to only the deviatoric part as in the original Bergström-Boyce model [19]. This is done to ensure that viscous volume growth is obtained also for hydrostatic tension loading, as to be expected from a matrix-particle decohesion theory. In addition, a purely stress-activated viscous deformation is employed, neglecting the deformation induced viscosity in the original model, as it improved the fit between the model and the experimental results.

For the flow potential g, used to obtain the direction of the viscous deformation in line with Equation 19, the Gurson yield function [27] was applied to incorporate the effects of matrix-particle decohesion

$$g = \left(\frac{\sigma_{eq}}{\bar{\sigma}} \right)^2 + 2 q_1 f \cosh \left(\frac{q_2 \mathrm{tr} \tilde{\boldsymbol{\Sigma}}_{\mathrm{B}}}{2\bar{\sigma}} \right) - \left(1 + q_3 f^2 \right) \tag{25}$$

where f is the void fraction, $\bar{\sigma}$ is a normalizing stress, q_i are the material parameters introduced in the model by Tvergaard [28], while σ_{eq} is the equivalent stress defined by the relation

$$\sigma_{eq} = \sqrt{\frac{3}{2} \tilde{\boldsymbol{\Sigma}}_{\mathrm{B}}' : \tilde{\boldsymbol{\Sigma}}_{\mathrm{B}}'} \tag{26}$$

The direction of the viscous deformation can then be obtained as

$$\mathbf{N}_{\mathrm{B}}^{v} = \frac{\partial g}{\partial \tilde{\boldsymbol{\Sigma}}_{\mathrm{B}}} = \frac{q_1 q_2 f}{\bar{\sigma}} \sinh \left(\frac{q_2 \mathrm{tr} \tilde{\boldsymbol{\Sigma}}_{\mathrm{B}}}{2\bar{\sigma}} \right) \mathbf{I} + \frac{3}{\bar{\sigma}^2} \tilde{\boldsymbol{\Sigma}}_{\mathrm{B}}' = n_{vol} \mathbf{I} + n_{dev} \tilde{\boldsymbol{\Sigma}}_{\mathrm{B}}' \tag{27}$$

Note that for the Gurson formulation, the unit of $\mathbf{N}_{\mathrm{B}}^{v}$ is 1/Pa, meaning that the unit of $\dot{\gamma}_{\mathrm{B}}^{0}$ must be Pa/s.

The initial particle fraction f_0 is an input parameter to the model, while an evolution equation defined from the conservation of mass reads

$$\dot{f} = (1 - f) \, \mathrm{tr} \tilde{\mathbf{D}}_{\mathrm{B}}^{v} = (1 - f) \left(3 \dot{\gamma}_{\mathrm{B}} n_{vol} \right) \tag{28}$$

Here, it is assumed that the volume fraction of voids can only increase due to growth of cavities around filler particles, and not through void nucleation. The particles that were found to debond

from the matrix of the HNBR1 material were identified as ZnO particles, known to be nearly rigid compared with the elastomeric matrix. Therefore, the porosity f is assumed equal or greater than the initial porosity level f_0 at all times. This is included in the model through the steps of Algorithm 1.

Algorithm 1: Procedure to ensure $f \geq f_0$ in iteration step n+1

Input from step n: $(I_{1B})_n$, f_n, $\dot{\gamma}_{\mathrm{B}n}$

$n_{dev} = \frac{3}{\bar{\sigma}^2}$

$n_{vol} = \frac{q_1 q_2 f_n}{\bar{\sigma}} \sinh\left(\frac{q_2 (I_{1B})_n}{2\bar{\sigma}}\right)$

$\dot{f} = (1 - f_n)\, 3\dot{\gamma}_{Bn} n_{vol}$

$f_{n+1} = f_n + dt\dot{f}$

if $f_{n+1} < f_0$ **then**

  $f_{n+1} = f_0$

  $n_{vol} = 0$

end

$\mathbf{N}_B^v = n_{vol}\mathbf{I} + n_{dev}\tilde{\mathbf{\Sigma}}'_B$

4.3. Temperature dependence

For the thermal modelling of the materials, the deformation induced temperature increase presented in Section 2.3.3 is neglected, limiting the simulations to isothermal conditions. Consequently, the temperature dependence can be included in the model solely by defining the material parameters as a function of the testing temperature [46]. A simple mathematical relation was applied to all temperature dependent parameters, defined for the dummy parameter a as [47]

$$a\,(\theta) = a_0 \exp\left[\frac{\theta_0 - \theta}{\theta_{base}}\right] \tag{29}$$

where θ is the testing temperature, a_0 the parameter value at $\theta_0 = 296$ K, and θ_{base} a scaling temperature. The model can be further developed to account for non-isothermal conditions, see [46, 48, 9].

4.4. Determination of material parameters

To illustrate the capabilities of the proposed model, the behaviour of the FKM material at the three testing temperatures was simulated. To obtain the temperature dependent parameters, the optimization software LS-OPT [49] was used, resulting in the parameter values listed in Table 2. The rest of the model parameters were defined as temperature independent, and their values are listed in Table 3. The bulk moduli $\kappa_B = 2.2$ GPa was found from confined axial compression experiments on similar materials [8], while $m = 6$, $\lambda_L = 1.8$, and $\alpha = 50$ were values found to yield reasonable agreement between simulation and experimental results for all temperature levels. The same locking stretch was used for the spring in Part A and Part B. Since $\dot{\gamma}_{\mathrm{B}}^0$ was included in Equation 23 only for dimensional consistency, its value was set to unity. For the parameters q_1 and q_2, the same values as proposed by Tvergaard [28], being 1.5 and 1 respectively, were used

Table 2: Optimized a_0 and θ_{base} values of Equation 29 for temperature dependent parameters, optimized for the FKM material.

	a_0	θ_{base}
μ_A	1.33 MPa	41.7 K
μ_B	17.20 MPa	27.7 K
κ_A	24.0 MPa	134.0 K
τ	0.63 MPa	33.8 K
$\bar{\sigma}$	0.40 MPa	31.1 K

Table 3: Temperature independent variables used for the FKM material.

κ_B	m	λ_L	α	$\dot{\gamma}_B^0$	q_1	q_2	f_0
2.2 GPa	6	1.8	50	1 Pa/s	1.5	1	0.01

(note that q_3 in Equation 25 is not present in the model due to the differentiation in Equation 27). The initial particle volume fraction f_0 was set to 0.01 based on the pre-deformation SEM images presented by Ilseng et al. [8].

4.5. Results

The constitutive model was implemented in Fortran as an explicit user-defined material model for the commercial finite element software LS-DYNA [50], and was tested on an 8-node brick element. The loading was defined by applying the stress-time history of the FKM experiment at the corresponding testing temperature to the upper boundary of the element.

The Cauchy stress - logarithmic strain and hydrostatic stress - volume ratio results from the proposed model are compared with the experimental data for the three temperature levels in Figure 10. In general, a good agreement between experimental and simulation results is obtained, and the temperature dependence of the material is well captured by the simple relation used in the model.

For the stress - strain response in Figure 10a, a reasonably good fit between the model and the experimental data is seen, although a too compliant response is obtained in the 23 °C simulation, leading to an overestimation of the maximum deformation. For the 0 and −18 °C simulations on the other hand, the initial stiffness is seen to be too high, exaggerating the stress response at small strains. In addition, the strain level at the end of the unloading is larger in the simulation results than in the experimental data.

Looking closer at the hydrostatic stress - volume ratio results in Figure 10b, the loading behaviour of the simulations conform well to the experimental data, while for the unloading on the other hand, the volume ratios predicted by the model are decreasing too slowly during the initial phase. Moreover, as for the strain level, the predicted volume ratios at the end of the deformation cycles are too large compared with the experimental data.

The evolution of the void fraction f with hydrostatic stress is shown in Figure 10c for all three simulations. Here, it is seen that the void fraction grows as the hydrostatic stress is increasing, while it is nearly constant during the initial decrease of the hydrostatic stress. The plateaus of the curves in Figure 10c correspond with the initially slow decrease of the volume ratios in Figure 10b. The explanation for this behaviour can be found from the gradient component n_{vol} of Equation 27. As the material starts to unload, the volumetric stress in the spring of Part B goes from tension to compression, yielding a low value of n_{vol} during this transition. Consequently, the changes of the volumetric part of the viscous deformation gradient tensor (Equation 21) and the void volume fraction (Equation 28) are small during the initial phase of unloading.

The relation between the two bulk moduli of the model, κ_A and κ_B, deserves some further attention. The fact that $\kappa_A << \kappa_B$ ensures that nearly all volumetric deformation in Part B occurs in the dashpot during uniaxial tension, making the volumetric increase visco-hyperelastic. When, on the other hand, the model is subjected to negative hydrostatic stress situations, the requirement of $f \geq f_0$ suppresses the dashpot from deforming volumetrically, and the stiff rate-independent volumetric response of the spring in Part B is dominating the overall behaviour, matching observations from experimental work [23]. This is illustrated in Figure 10d, where the model's response to a volumetric compression is compared with experimental results from confined axial compression tests at room temperature [23]. It is likely that the bulk modulus κ_B to some extent is temperature dependent, as the bulk modulus obtained by hydrostatic compression testing of natural rubber was reported by Wood and Martin [22] to decrease as the temperature was reduced, however, this dependence would have limited influence on the simulation results presented herein.

5. Concluding remarks

An experimental procedure enabling measurement of the volume growth accompanying tension of elastomers at low temperatures was outlined. The use of grease and icing sugar to obtain the DIC speckle patterns was found to be superior over traditional spray painting for low testing temperatures. The results from the HNBR and FKM compounds showed a significant increase in volume growth as the temperature was reduced from 23 to -18 °C. By the use of in situ SEM, matrix-particle debonding was observed during tension of two of the materials at room temperature, yielding a micro-mechanical explanation for the macroscopically observed volume growth. The thermal sensitivity of the volumetric response is thereby assumed to stem from a temperature dependence of the cohesive zone properties. A new constitutive model, building on the Bergström-Boyce visco-hyperelastic elastomer model and the Gurson flow potential function, was outlined to capture the observed effects within a relatively simple continuum mechanical formulation. The new constitutive model was implemented as a user material for the finite element software LS-DYNA. Thermal features were included in the model by defining a temperature dependent mathematical

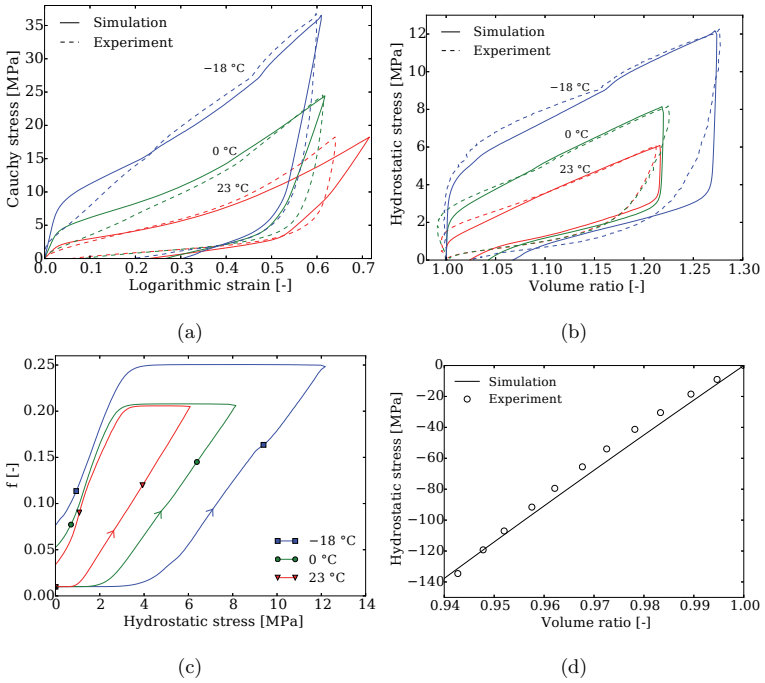

Figure 10: Simulation results from the proposed constitutive model, (a) Cauchy stress - logarithmic strain compared with FKM experimental data, (b) hydrostatic stress - volume ratio compared with FKM experimental data, (c) evolution of f during the simulations at each temperature, and (d) model behaviour under volumetric compression compared with experimental confined axial compression data.

relation for five of the model parameters. With optimized input parameters, the model showed a good fit to the experimental data for both the stress - strain behaviour and the hydrostatic stress - volume ratio response at all three temperature levels. In addition, the response to a hydrostatic compression stress is seen to conform well to previously presented results for confined axial compression.

Acknowledgements

The authors acknowledge Aker Solutions AS for their funding of this research. In addition, the authors would like to express their gratitude to Mr Trond Auestad for his assistance with the low temperature tension tests, and Mr Christian Oen Paulsen for his assistance during the SEM study.

References

[1] ISO, 10423:2009 Petroleum and natural gas industries Drilling and production equipment Wellhead and christmas tree equipment, Tech. rep. (2009).

[2] A. N. Gent, B. Park, Failure processes in elastomers at or near a rigid spherical inclusion, Journal of Materials Science 19 (1984) 1947–1956.

[3] K. Cho, A. N. Gent, P. S. Lam, Internal fracture in an elastomer containing a rigid inclusion, Journal of Materials Science 22 (1987) 2899–2905.

[4] J. B. Le Cam, E. Toussaint, Volume Variation in Stretched Natural Rubber: Competition between Cavitation and Stress-Induced Crystallization, Macromolecules 41 (2008) 7579–7583.

[5] J.-B. Le Cam, E. Toussaint, Cyclic volume changes in rubber, Mechanics of Materials 41 (2009) 898–901.

[6] J. de Crevoisier, G. Besnard, Y. Merckel, H. Zhang, F. Vion-Loisel, J. Caillard, D. Berghezan, C. Creton, J. Diani, M. Brieu, F. Hild, S. Roux, Volume changes in a filled elastomer studied via digital image correlation, Polymer Testing 31 (2012) 663–670.

[7] S. Cantournet, K. Layouni, L. Laiarinandrasana, R. Piques, Experimental investigation and modelling of compressibility induced by damage in carbon black-reinforced natural rubber, Comptes Rendus Mécanique 342 (2014) 299–310.

[8] A. Ilseng, B. H. Skallerud, A. H. Clausen, An experimental and numerical study on the volume change of particle-filled elastomers in various loading modes, Submitted - 2016.

[9] A. Lion, On the large deformation behaviour of reinforced rubber at different temperatures, Journal of the Mechanics and Physics of Solids 45 (1997) 1805–1834.

[10] A. D. Drozdov, J. Christiansen, Thermo-viscoplasticity of carbon black-reinforced thermoplastic elastomers, International Journal of Solids and Structures 46 (2009) 2298–2308.

[11] H. Laurent, G. Rio, A. Vandenbroucke, N. Aït Hocine, H. L. G. Rio, A. V. N. Aït, Experimental and numerical study on the temperature-dependent behavior of a fluoro-elastomer, Mechanics of Time-Dependent Materials 18 (2014) 721–742.

[12] A. Ilseng, B. H. Skallerud, A. H. Clausen, Tension behaviour of HNBR and FKM elastomers for a wide range of temperatures, Polymer Testing 49 (2016) 128–136.

[13] R. S. Rivlin, Large Elastic Deformations of Isotropic Materials. IV. Further Developments of the General Theory, Philosophical Transactions of the Royal Society A: Mathematical, Physical and Engineering Sciences 241 (1948) 379–397.

[14] O. H. Yeoh, Some forms of the strain energy function for rubber, Rubber Chemistry and Technology 66 (1993) 754–771.

[15] R. W. Ogden, Large Deformation Isotropic Elasticity: On the Correlation of Theory and Experiment for Compressible Rubberlike Solids, Proceedings of the Royal Society of London A: Mathematical, Physical and Engineering Sciences 328 (1972) 567–583.

[16] E. M. Arruda, M. C. Boyce, A three-dimensional constitutive model for the large stretch behavior of rubber elastic materials, Journal of the Mechanics and Physics of Solids 41 (1993) 389–412.

[17] G. A. Holzapfel, J. C. Simo, A new viscoelastic constitutive model for continuous media at finite thermomechanical changes, International Journal of Solids and Structures 33 (1996) 3019–3034.

[18] A. Lion, A constitutive model for carbon black filled rubber: Experimental investigations and mathematical representation, Continuum Mechanics and Thermodynamics 8 (1996) 153–169.

[19] J. S. Bergström, M. C. Boyce, Constitutive modeling of the large strain time-dependent behavior of elastomers, Journal of the Mechanics and Physics of Solids 46 (1998) 931–954.

[20] G. Ayoub, F. Zaïri, M. Naït-Abdelaziz, J. Gloaguen, G. Kridli, A visco-hyperelastic damage model for cyclic stress-softening, hysteresis and permanent set in rubber using the network alteration theory, International Journal of Plasticity 54 (2014) 19–33.

[21] P. W. Bridgman, The Compression of Sixty-One Solid Substances to 25,000 kg/cm2 Determined by a New Rapid Method, Proceedings of the American Academy of Arts and Sciences 76 (1945) 9–24.

[22] L. A. Wood, G. M. Martin, Compressibility of Natural Rubber at Pressures Below 500 KG/CM2, Rubber Chemistry and Technology 37 (1964) 850–865.

[23] A. Ilseng, B. H. Skallerud, A. H. Clausen, Volumetric compression of HNBR and FKM elastomers, Constitutive Models for Rubber IX - Proceedings of the 9th European Conference on Constitutive Models for Rubbers, 2015,

pp. 235–241.

[24] J. Li, D. Mayau, F. Song, A constitutive model for cavitation and cavity growth in rubber-like materials under arbitrary tri-axial loading, International Journal of Solids and Structures 44 (2007) 6080–6100.

[25] J. Li, D. Mayau, V. Lagarrigue, A constitutive model dealing with damage due to cavity growth and the Mullins effect in rubber-like materials under triaxial loading, Journal of the Mechanics and Physics of Solids 56 (2008) 953–973.

[26] O. Lopez-Pamies, T. Nakamura, M. I. Idiart, Cavitation in elastomeric solids: II - Onset-of-cavitation surfaces for Neo-Hookean materials, Journal of the Mechanics and Physics of Solids 59 (2011) 1488–1505.

[27] A. L. Gurson, Continuum Theory of Ductile Rupture by Void Nucleation and Growth: Part I-Yield Criteria and Flow Rules for Porous Ductile Media, Journal of Engineering Materials and Technology 99 (1977) 2–15.

[28] V. Tvergaard, Influence of voids on shear band instabilities under plane strain conditions, International Journal of Fracture 17 (1981) 389–407.

[29] Z. Zhang, C. Thaulow, J. Ødegård, A complete Gurson model approach for ductile fracture, Engineering Fracture Mechanics 67 (2000) 155–168.

[30] T. Pardoen, J. W. Hutchinson, Extended model for void growth and coalescence, Journal of the Mechanics and Physics of Solids 48 (2000) 2467–2512.

[31] J. Wen, Y. Huang, K. Hwang, C. Liu, M. Li, The modified Gurson model accounting for the void size effect, International Journal of Plasticity 21 (2005) 381–395.

[32] K. Nahshon, J. W. Hutchinson, Modification of the Gurson Model for shear failure, European Journal of Mechanics, A/Solids 27 (2008) 1–17.

[33] A. Steenbrink, E. Van Der Giessen, P. Wu, Void growth in glassy polymers, Journal of the Mechanics and Physics of Solids 45 (1997) 405–437.

[34] M. Challier, J. Besson, L. Laiarinandrasana, R. Piques, Damage and fracture of polyvinylidene fluoride (PVDF) at 20 C: Experiments and modelling, Engineering Fracture Mechanics 73 (2006) 79–90.

[35] T. F. Guo, J. Faleskog, C. F. Shih, Continuum modeling of a porous solid with pressure-sensitive dilatant matrix, Journal of the Mechanics and Physics of Solids 56 (2008) 2188–2212.

[36] ISO, 37:2011 Rubber, vulcanized or thermoplastic - Determination of tensile stress-strain properties, Tech. rep. (2011).

[37] J. Johnsen, F. Grytten, O. S. Hopperstad, A. H. Clausen, Experimental set-up for determination of the large-strain tensile behaviour of polymers at low temperatures, Polymer Testing 53 (2016) 305–313.

[38] E. Fagerholt, T. Børvik, O. Hopperstad, Measuring discontinuous displacement fields in cracked specimens using digital image correlation with mesh adaptation and crack-path optimization, Optics and Lasers in Engineering 51 (2013) 299–310.

[39] M. Karlsen, J. Hjelen, Ø. Grong, G. Rørvik, R. Chiron, U. Schubert, E. Nilsen, SEM/EBSD based in situ studies of deformation induced phase transformations in supermartensitic stainless steels, Materials Science and Technology 24 (2008) 64–72.

[40] G. A. Holzapfel, Nonlinear Solid Mechanics: A Continuum Approach for Engineering, John Wiley & Sons, 2000.

[41] T. Belytschko, W. K. Liu, B. Moran, K. Elkhodary, Nonlinear Finite Elements for Continua and Structures, Wiley, 2014.

[42] J. C. Simo, C. Miehe, Associative coupled thermoplasticity at finite strains: Formulation, numerical analysis and implementation, Computer Methods in Applied Mechanics and Engineering 98 (1992) 41–104.

[43] A. Cohen, A Padé approximant to the inverse Langevin function, Rheologica Acta 30 (1991) 270–273.

[44] F. Sidoroff, Un modèle viscoélastique non linéaire avec configuration intermédiaire, Journal de Mécanique 13 (1974) 679–713.

[45] J. Bergström, Mechanics of Solid Polymers, Elsevier, 2015.

[46] S. C. H. Lu, K. S. Pister, Decomposition of deformation and representation of the free energy function for

isotropic thermoelastic solids, International Journal of Solids and Structures 11 (1975) 927–934.

[47] J. Bergström, L. Hilbert, A constitutive model for predicting the large deformation thermomechanical behavior of fluoropolymers, Mechanics of Materials 37 (2005) 899–913.

[48] G. Holzapfel, J. Simo, Entropy elasticity of isotropic rubber-like solids at finite strains, Computer Methods in Applied Mechanics and Engineering 132 (1996) 17–44.

[49] Livermore Software Technology Corporation (LSTC), LS-OPT User's Manual, version 5.2, 2015.

[50] Livermore Software Technology Corporation (LSTC), LS-DYNA keyword user's manual, version R8.0, vols 1 and 2, 2016.

Appendix

A.1

Arne Ilseng, Bjørn H. Skallerud, Arild H. Clausen

Case study of elastomer seals using FEM

Eight national conference on Computational Mechanics, 2015, pp. 203-218, ISBN:978-84-944244-9-6

A.1

8. National Conference on Computational Mechanics
MekIT'15
B. Skallerud and H I Andersson (Eds)

CASE STUDY OF ELASTOMER SEALS USING FEM

ARNE ILSENG[1], BJØRN H. SKALLERUD[1] AND ARILD H. CLAUSEN[1]

[1]Department of Structural Engineering
Norwegian University of Science and Technology
7491 Trondheim, Norway
e-mail: arne.ilseng@ntnu.no

Key words: Computational Methods, Elastomer seals, Compressibility

Abstract. Increased use of numerical calculations, such as finite element simulations, during the design process of elastomer seals exposed to high pressures could possibly reduce the occurrence of seal failure in the oil and gas industry. A generic model of an elastomer seal was used to study its sensitivity to changes in the input parameters. Base parameters for the deviatoric and volumetric part of two hyperelastic models were obtained by performing simple tension and volumetric compression experiments on a hydrogenated nitrile butadiene rubber compound. It is shown that the sealing force of the model is mainly affected by changes in the bulk modulus, while the maximum principal strain in the seal is dominated by the values of the shear modulus and the elastomer-steel friction parameter.

1 INTRODUCTION

Unexpected failure of elastomer seals exposed to high pressures is an expensive issue for the oil and gas industry. Increased use of numerical calculations, such as finite element simulations, during the design process of such seals could possibly reduce the occurrence of failure, and thereby cut costs. For numerical simulations to be predictive and useful, a reasonable accuracy of the model parameters is of outmost importance. In the oil and gas industry, many different elastomer materials (i.e. materials with different polymer basis) and elastomer compounds (i.e. same polymer basis but different type or amount of fillers, bonding promoters etc.) are used for sealing applications. Naturally, these different materials/compounds might have different mechanical properties. In addition, aspects as ageing, temperature changes, exposure to fluids, etc. can change the material performance during service. Obtaining precise data for all compounds exposed to all possible service conditions would therefore be a tremendous task. To gain knowledge of how elastomer seal performance is affected by possible changes in material parameters is therefore of interest.

Due to their low shear to bulk modulus ratio, elastomers are commonly assumed incompressible for unconfined deformation and multiple studies have investigated the deviatoric material behaviour of numerous elastomer compounds (e.g. the classical data by Treloar [16], and the work by Bergström and Boyce [3]). For sealing applications though, the service condition is by design highly confined and exposed to a significant pressure level, possibly as high as 138 MPa [11], and therefore the compressibility of the material cannot be neglected. Only a few studies on the compressibility of elastomers are present in the literature, e.g. with the work by Bridgman [7], Wood and Martin [17], and Bradley et al. [6], but no studies could be found for the compressibility of elastomer materials typically used in the oil and gas industry.

When it comes to the constitutive modelling of elastomers, a lot of work has been done on the incompressible material behaviour [15, 13, 18, 2], and some work on the compressible behaviour [1, 4]. Boyce and Arruda [5] presented a thorough review of different constitutive models for elastomers.

In this work, simple tension and volumetric compression tests were performed on a hydrogenated nitrile butadiene rubber (HNBR) compound and the test data was used to obtain material parameters for two different hyperelastic models. A generic sealing case was studied numerically to indicate the difference between the two material models. In addition, a parameter study, altering one of the input parameters at the time in subsequent simulations, was performed to investigate how the input parameters affect the obtained results. The present article is organized as follows. In the coming section, general material modelling for elastomer materials is outlined. Thereafter, the uniaxial tension test and the volumetric compression test are described and material parameters are obtained from the test data. In Section 4, the geometry and loading of the case study are outlined, while the results of the case study are presented and discussed in Section 5. In the final section, conclusions from the work are presented.

2 MATERIAL MODELLING

The fundamental point of departure for a continuum mechanics material description is the deformation gradient $\mathbf{F}$, yielding a mapping between reference and current configuration. The deformation gradient is defined mathematically by

$$\mathbf{F} = \frac{\partial \mathbf{x}}{\partial \mathbf{X}} \tag{1}$$

where $\mathbf{x}$ represents the current position of a material point, and $\mathbf{X}$ represents the reference position of a material point. Based on the deformation gradient, the left Cauchy-Green tensor can be defined as $\mathbf{b} = \mathbf{F}\mathbf{F}^T$, and its principal invariants I_1, I_2, and I_3 are given according to

$$I_1 = \mathrm{tr}\left(\mathbf{b}\right) = \lambda_1^2 + \lambda_2^2 + \lambda_3^2 \tag{2}$$
$$I_2 = \frac{1}{2}\left[\left(\mathrm{tr}\mathbf{b}\right)^2 - \mathrm{tr}\left(\mathbf{b}^2\right)\right] = \lambda_1^2\lambda_2^2 + \lambda_2^2\lambda_3^2 + \lambda_3^2\lambda_1^2$$
$$I_3 = J^2 = \mathrm{det}\mathbf{b} = \lambda_1^2\lambda_2^2\lambda_3^2$$

where the notation λ_i is used for the stretch ratio in the principal direction i, and J denotes the volume ratio. In isotropic hyperelastic material modelling, a strain energy function $U = U(I_1, I_2, I_3)$ is used to define the material behaviour. According to Flory [9] the strain energy function can be split additively into a deviatoric and a volumetric part. By defining two modified invariants $\bar{I}_1 = J^{-2/3}I_1$ and $\bar{I}_2 = J^{-4/3}I_2$, an additive split of the strain energy can be written as

$$U = U_{dev}\left(\bar{I}_1, \bar{I}_2\right) + U_{vol}\left(J\right) \tag{3}$$

Physically, the deviatoric part defines the entropic energy, neglecting entropy changes due to volumetric deformation, while the volume part represents changes in the internal energy [4]. Due to its numerical convenience, the additive split is commonly incorporated in commercial finite element software. Based on the strain energy potential, the deviatoric and volumetric part of the Cauchy stress are calculated by

$$\boldsymbol{\sigma}_{dev} = \frac{2}{J}DEV\left[\left(\frac{\partial U_{dev}}{\partial \bar{I}_1} + \bar{I}_1\frac{\partial U_{dev}}{\partial \bar{I}_2}\right)\bar{\mathbf{b}} - \frac{\partial U_{dev}}{\partial \bar{I}_2}\bar{\mathbf{b}}\cdot\bar{\mathbf{b}}\right] \tag{4}$$
$$\boldsymbol{\sigma}_{vol} = \frac{\partial U_{vol}}{\partial J}\mathbf{I}$$

where $\mathbf{I}$ denotes the second order unit tensor, and $\bar{\mathbf{b}}$ is the isochoric part of the left Cauchy-Green tensor, $\bar{\mathbf{b}} = J^{-2/3}\mathbf{b}$. The deviatoric part of $\bar{\mathbf{b}}$ is defined as $DEV\left[\bar{\mathbf{b}}\right] = \bar{\mathbf{b}} - \frac{1}{3}\bar{I}_1\mathbf{I}$. To obtain material parameters for the deviatoric part of the equation, $\boldsymbol{\sigma}_{dev}$ can be estimated from uniaxial tension tests. The deformation state in a uniaxial tension test is given by

$$\lambda_1 = \lambda \tag{5}$$
$$\lambda_2 = \lambda_3 = \sqrt{\frac{J}{\lambda}}$$
$$\bar{I}_1 = J^{-2/3}\left(\lambda^2 + 2\frac{J}{\lambda}\right)$$

The left Cauchy-Green tensor for this deformation state is obtained as

$$\mathbf{b} = \begin{bmatrix}\lambda^2 & 0 & 0\\ 0 & \frac{J}{\lambda} & 0\\ 0 & 0 & \frac{J}{\lambda}\end{bmatrix} \tag{6}$$

For the case of a compressible material under uniaxial tension the 11-component of $DEV\left[\bar{\mathbf{b}}\right]$ can be found as

$$DEV\left[\bar{\mathbf{b}}\right]_{11} = \frac{2J^{-2/3}}{3}\left(\lambda^2 - \frac{J}{\lambda}\right) \tag{7}$$

2.1 Neo-Hookean model

The strain energy potential for the neo - Hookean model [14] is defined as

$$U_{dev} = \frac{\mu_0}{2}\left(\bar{I}_1 - 3\right) \tag{8}$$

where μ_0 is the initial shear modulus. By use of Equation (4) and Equation (7), the 11-component of the deviatoric stress tensor can be found for a uniaxial tension case

$$\sigma^{11}_{dev,neo} = \frac{2\mu_0 J^{-5/3}}{3}\left(\lambda^2 - \frac{J}{\lambda}\right) \tag{9}$$

2.2 Yeoh model

To better conform to the non-linear behaviour found for uniaxial testing of elastomers, a Yeoh model [18] can be used for the deviatoric part of the strain energy rather than the neo-Hookean model. The strain energy function is then defined as

$$U_{dev} = C_{10}\left(\bar{I}_1 - 3\right) + C_{20}\left(\bar{I}_1 - 3\right)^2 + C_{30}\left(\bar{I}_1 - 3\right)^3 \tag{10}$$

where C_{i0} are parameters to be defined from experimental data. As opposed to the neo-Hookean model, which can be derived from single chain Gaussian statistics theory, the Yeoh model is purely phenomenological and the constants cannot be given any physical interpretation. Using Equation (4) and Equation (7), the 11-component of the deviatoric part of the Cauchy stress can be found for the Yeoh model as

$$\sigma^{11}_{dev,yeoh} = \frac{4J^{-5/3}}{3\lambda}\left(C_{10} + 2C_{20}\left(\bar{I}_1 - 3\right) + 3C_{30}\left(\bar{I}_1 - 3\right)^2\right)(\lambda - J) \tag{11}$$

2.3 Volumetric model

The volumetric part of the strain energy potential is given herein by a simple model as used by Miehe [12], leading to a linear stress - volume change relation

$$\begin{aligned} U_{vol} &= \frac{\kappa_0}{2}(J-1)^2 \\ \boldsymbol{\sigma}_{vol} &= \kappa_0 (J-1)\,\mathbf{I} \end{aligned} \tag{12}$$

where κ_0 is the initial bulk modulus of the material. The value of κ_0 can be estimated based on a pressure - volume change relation obtained from experimental data.

3 MODEL PARAMETERS FROM EXPERIMENTAL DATA

3.1 Deviatoric response

Uniaxial tension tests on the HNBR material were performed by use of an Instron 5944 testing machine with a 2 kN load cell. A conceptual drawing of the test sample is shown in Figure 1a. To enable digital image correlation (DIC) measurements, a random grey

scale speckle pattern was painted on the gauge section of the specimens and two cameras logged pictures of respectively the wide and the narrow surface during deformation. Representative results for the long-term behaviour of the material were obtained by applying five cycles of deformation as a precondition to remove most of the softening effects in the material, and camera logging started at the beginning of the sixth cycle. The specimens were deformed 40 mm from their initial length at a deformation rate of 1.5 mm/s, and the machine thereafter returned by load control to a force of 0 kN. By use of an in-house DIC software [8], the stretch ratios for both the longitudinal and the two transverse directions were calculated. The three stretch ratios were used to obtain the true stress level throughout the test, in addition to calculating the volume change accompanying tension. Since the maximum volume change during the test was found to be 0.3%, this was neglected when fitting the models to the test data. The experimentally obtained stress-stretch curve and the fit of the neo-Hookean and the Yeoh material models are shown in Figure 2a. A hysteresis loop is seen for the experimental loading/unloading data, representing the time dependency of the elastomer behaviour. Since purely elastic models are used for the simulations, this time dependency is not included in the material modelling. From the fit, it can be seen that the neo-Hookean model is unable of representing the non-linear behaviour found in the experimental data. For the Yeoh model on the other hand, the equilibrium behaviour of the experimental curve is well captured.

3.2 Volumetric response

A rig for volumetric compression testing was designed to be used with an Instron 5982 universal testing machine with a t-slot table. The layout of the test set-up is illustrated in Figure 1b. It involves two pistons with load cells and a 20 mm thick steel plate supported on four bolts. The centre hole of the steel plate was produced with a diameter of 29 mm and a tolerance of $+0.05$ mm, -0.00 mm. To ensure a tight fit, the upper and lower pistons were machined with a diameter of 29 mm and a tolerance of $+0.00$ mm, -0.05 mm. The plate was fixed to the t-slot table of the testing machine by the four steel bolts, while the two pistons were screwed onto the load cells. In addition to the 100 kN load cell of the test machine, an HBM U2A 100 kN load cell was included below the specimen, fixed to the t-slot table with bolts. To avoid uncertainties in the displacement measurement due to machine compliance, a checkerboard pattern was applied to the upper piston. By logging pictures of this pattern during the deformation, the displacement was calculated by use of a point tracker routine [10]. It was assumed that the test set-up, which was made out of steel, was rigid and that all deformation therefore occurred in the specimen. A thin layer of silicon grease was applied to all surfaces of the specimen to reduce frictional forces. By logging the force in both load cells, it was found that the friction level was kept below 1.3 kN. The friction was therefore neglected when computing the material data. The machine deformed the specimen at a rate of 3 mm/min by load control until the load in the upper load cell reached a level of 95 kN, thereafter the load was reduced to 0.1 kN. Four cycles of deformation were applied as a precondition, and volume data

were obtained for the fifth cycle. The experimentally found pressure - volume ratio data and the fit of the volume part of the material model are seen in Figure 2b. It can be seen that the linear material model gives a good fit to the experimentally obtained data.

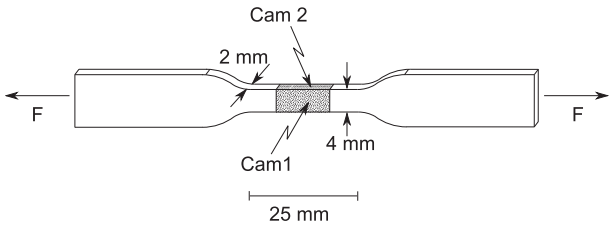

(a) Set-up for tension test

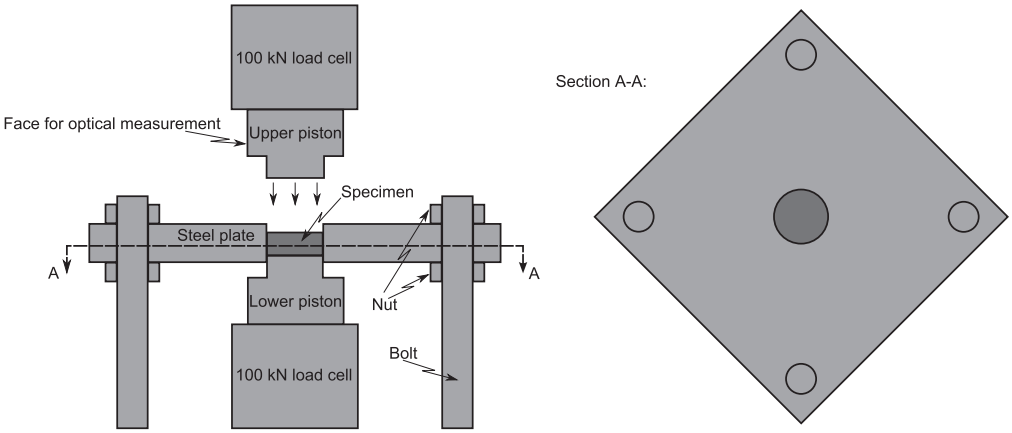

(b) Set-up for volumetric compression test

Figure 1: Experimental set-up for tension test and volumetric compression test

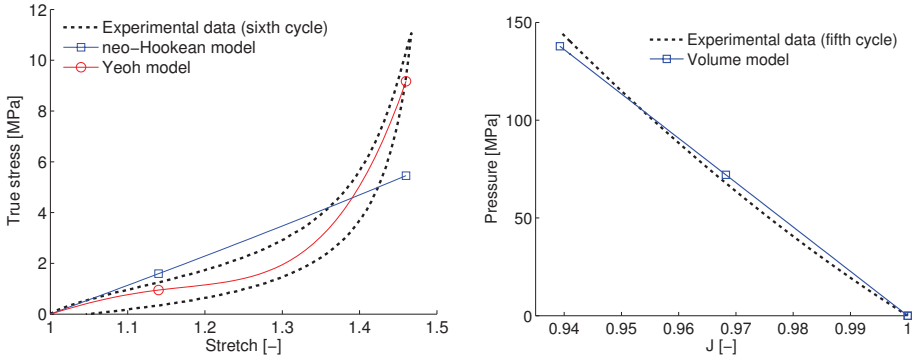

(a) Fit of material models to simple tension test

(b) Fit of material model to pressure - volume change data

Figure 2: Fit of material models to experimental for simple tension and volumetric compression

3.3 Elastomer-steel friction

The frictional forces between the elastomer specimen and the steel plate were calculated in the volumetric compression test. By reverse engineering, the friction parameter was optimized so that an axisymmetric model of the test set-up, using a linear description of the friction level, gave the same peak force as the experimental data. The experimental data and simulation result are shown in Figure 3. It is clear that assuming linear friction does not capture the physics of the experimental test. Anyhow, a linear friction model is useful within the scope of this work, which is to get an indication of how a variation of the friction level effects seal performance. An overview of the base parameters obtained from the experimental work and used for the case study simulations is presented in Table 1.

Table 1: Base model parameters

neo-Hookean	Yeoh			Volume model	Friction coefficient
μ_0	C_{10}	C_{20}	C_{30}	κ_0	f
5.7 MPa	7.1 MPa	-15.4 MPa	40 MPa	2.3 GPa	0.012

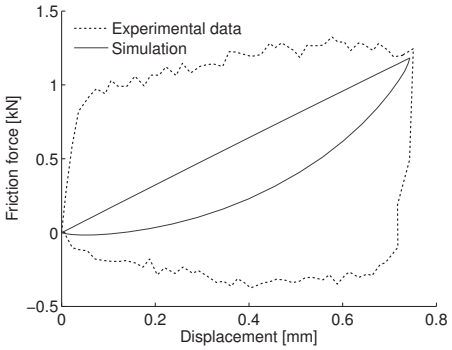

Figure 3: Frictional forces in experiment and simulation. Frictional coefficient of 0.012 used in simulation.

4 CASE STUDY GEOMETRY

Due to its appropriateness for numerical simulations, a model of an axisymmetric seal with a square cross section was used for the case study. The modelled seal had an internal diameter of 200 mm and a width of 8.4 mm. Analytically rigid plates were modelled to enclose the seal. A sketch of the geometry is shown in Figure 4. The loading of the seal was applied in two steps, first the vertical rigid plate was displaced in negative x-direction to reduce the width of the specimen by 15%, and thereafter the introduction of a fluid in the upper chamber was represented by applying a pressure load of 100 MPa on the upper surface of the seal. The axisymmetric geometry was discretized in Abaqus/Standard by 10 000 8-node biquadratic hybrid elements with reduced integration (CAX8RH). A surface-to-surface contact algorithm was used to enforce the contact between the elastomer and the rigid casing. The behaviour normal to the rigid boundaries was strictly enforced by a direct method, while linear friction was assumed for the tangential behaviour, using a penalty method. To evaluate how the parameters effect the numerical model, the sealing force, i.e. the horizontal force obtained in the vertical rigid plate in Figure 4, and the maximum principal logarithmic strain were evaluated for each simulation. The sealing force can be regarded as a measure of the seal performance, while the maximum principal logarithmic strain gives an indication of how much the seal is distorted, and thereby the risk of material failure. It should be noted that the location of the maximum principal logarithmic strain might change between the different analyses.

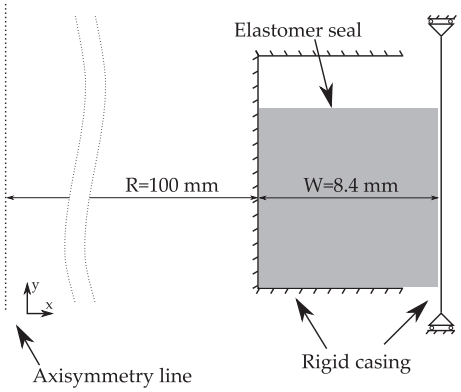

Figure 4: Conceptual layout of case study

5 CASE STUDY RESULTS

5.1 Sensitivity to choice of deviatoric part of material model

To investigate the sensitivity to the choice of model for the deviatoric part of the material behaviour, simulations were run with both the neo-Hookean and the Yeoh model. The resulting sealing force during the analyses can be seen in Figure 5a, while a contour plot of the maximum principal logarithmic strain obtained in the end configuration for the two simulations is shown in Figure 5b. It was found that the Yeoh model gave a sealing force at the end of the compression step (at pseudo time t1) of 47 kN, while for the neo-Hookean model the force was significantly lower, with 26 kN at the end of the compression of the specimen. During the pressure loading though (pseudo time t1 to t2), the force difference between the two models diminished, being only 1.4% after pressurization. A slightly higher maximum principal logarithmic strain was obtained for the neo-Hookean model (0.199) in the end configuration compared with the Yeoh model (0.177). In the further parameter study, the neo-Hookean model is used for the deviatoric material behaviour since it facilitates a simple change of the material shear modulus.

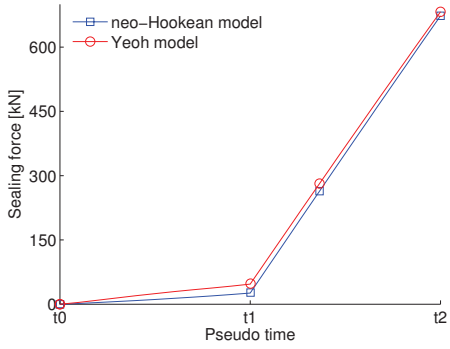

(a) Calculated sealing force for neo-Hookean and Yeoh model

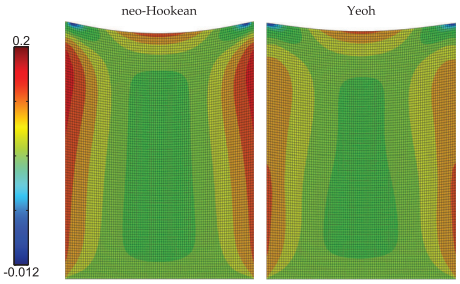

(b) Contour plot of maximum principal logarithmic strain for neo-Hookean and Yeoh model

Figure 5: Comparison of neo-Hookean and Yeoh model for the deviatoric part of the hyperelastic model

5.2 Sensitivity to shear modulus

In the following parameter study, one input parameter was varied around its base value for each simulation, while the other parameters were kept constant at the base values given in Table 1. In the coming figures, the results are normalized with respect to the values obtained for the neo-Hookean model using the base parameters, while the value of the altered input parameter is normalized with respect to the base value.

Figure 6a shows the normalized sealing force obtained as the initial shear modulus of the neo-Hookean model was changed, while the normalized maximum principal logarithmic strain at the end of the analyses is addressed in Figure 6b. For the sealing force, a clear increase is seen with increasing shear modulus, although the total change is limited to approximately 1.5% increase in force for a shear modulus twice as large. For the strain results, on the other hand, the effect of a change in the shear modulus is more pronounced, with a clear decrease in maximum principal logarithmic strain as the shear modulus increases. For an initial shear modulus of 2.8 MPa the maximum principal shear strain increased by more than 50%.

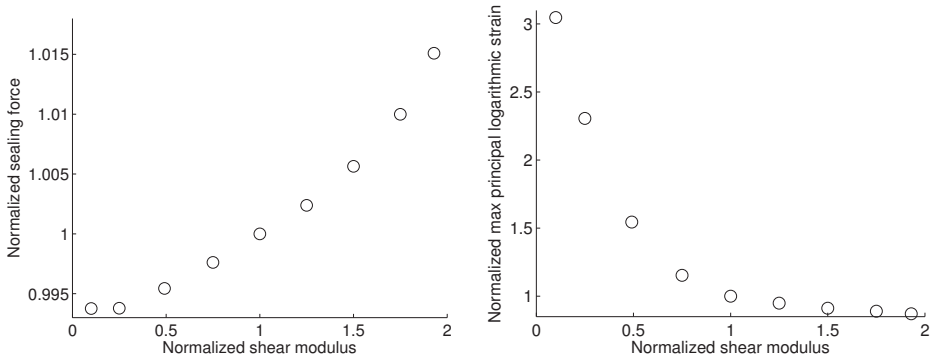

(a) Effect on sealing force (b) Effect on max principal strain

Figure 6: Parameter study for shear modulus

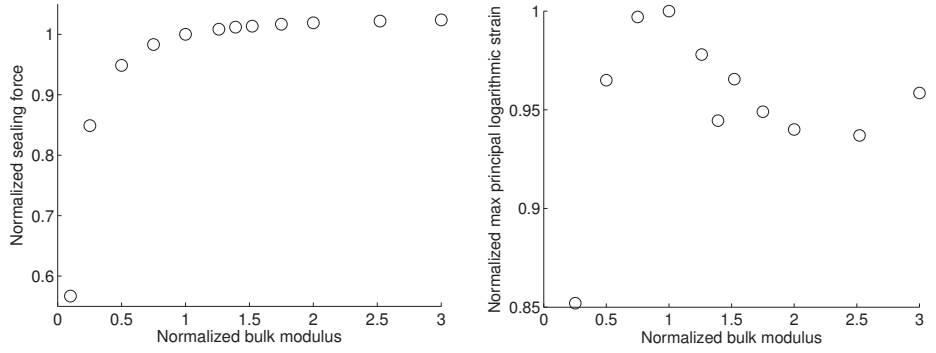

(a) Effect on sealing force (b) Effect on max principal strain

Figure 7: Parameter study for bulk modulus

5.3 Sensitivity to bulk modulus

The sensitivity of the sealing force on the initial bulk modulus in the volumetric part of the neo-Hookean model is plotted in Figure 7a, whereas the normalized maximum principal logarithmic strain at the end of the analyses is shown in Figure 7b. While increasing the bulk modulus above the base value has limited effect on the sealing force, a reduction of the bulk modulus give a pronounced reduction in the sealing force. Reducing the bulk modulus to a value of 0.23 GPa leads to a 43% reduction in the sealing force. It should be noted that even though a reduction of the bulk modulus by 90% seems extreme, calculating the Poisson's ratio as

$$\nu = \frac{3\kappa_0 - 2\mu_0}{2\left(3\kappa_0 + \mu_0\right)} \tag{13}$$

yields a value of 0.4988 for the base parameters, while 0.4877 is found for a bulk modulus of 0.23 GPa. In Figure 8, the progress of the sealing force as the pressure increases is shown for different values of the bulk modulus. It is seen that as the bulk modulus is reduced, the relation turns from linear to clearly non-linear. Thereby, as the applied pressure increase, using the correct value for the bulk modulus becomes increasingly important to obtain the correct sealing force.

For the strain measure, no clear trend is seen for a change of the bulk modulus. This can be explained by the change of location for the maximum principal strain between the different simulations. For the lowest values of the bulk modulus, compressive strains are dominating the seal deformation leading to a significant reduction in the maximum principal strain.

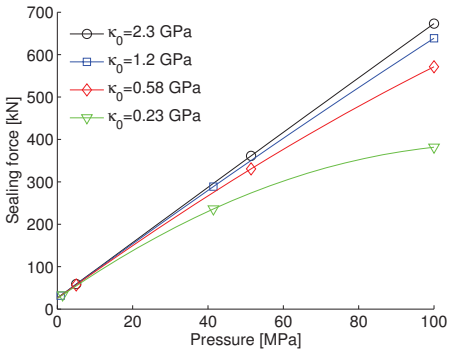

Figure 8: Sealing force as function of applied pressure

5.4 Sensitivity to friction coefficient

The sealing force and the maximum principal strain obtained for different values of the elastomer-steel friction parameter is shown in Figure 9a and Figure 9b respectively. There is a clear trend of an increasing sealing force as the friction parameter is increased, but the change is limited between -1.3% and +0.5%. The effect of changing the friction parameter is much stronger on the strain measure, where an increase in the friction parameter gives a significantly higher maximum principal strain.

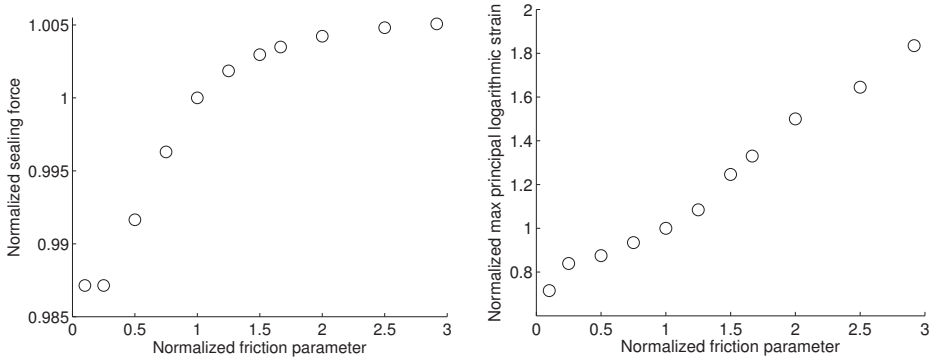

(a) Effect on sealing force (b) Effect on max principal strain

Figure 9: Parameter study for coefficient of friction between elastomer and steel

5.5 Discussion

From the results in the previous subsections, it is seen that for the high pressure sealing model studied, the choice of deviatoric material model has limited effect on the sealing force and the maximum principal logarithmic strain obtained in the end configuration. On the other hand, the neo-Hookean and Yeoh models gives substantially different sealing forces for the deformation in the first step of the numerical simulations.

From the parameter study, it is seen that the sealing force in the model is mainly affected by a reduction of the bulk modulus from its base value. Figure 10 shows how the normalized sealing force change as the Poisson's ratio, defined by Equation (13), was varied either through a change of the shear modulus or by a shift in the bulk modulus. It is clear that the Poisson's ratio is insufficient as a parameter to describe the elastomer behaviour, as the response of the model is dependent on both the shear and the bulk modulus. The shear modulus and the friction coefficient is seen to be the most important parameters for the level of maximum principal strain.

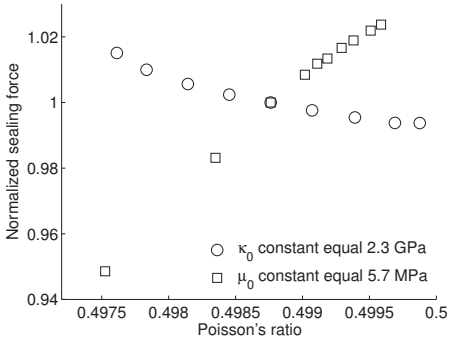

Figure 10: Sealing force as a function of Poisson's ratio for constant bulk modulus and constant shear modulus

6 CONCLUSIONS

Simple tension and volumetric compression experiments on an HNBR compound were performed. From the test data, parameters for two models of the deviatoric part and one model of the volumetric part of the strain energy function were obtained.

In the numerical case study, the two different models for the deviatoric part of the strain energy function were compared. There was a marked difference in the force level obtained for the two models during the initial phase of compressing the seal, while the difference between the models diminished as the external pressure was applied. Through a parameter study, it was found that the bulk modulus of the material seems to be the most important parameter for the level of the sealing force, while the shear modulus and the friction parameter are most important for the maximum principal strain obtained in the seal.

Based on the findings herein, great care should be taken when defining the bulk modulus for a simulation of an elastomer seal, since assuming an arbitrary nearly incompressible behaviour for the material might greatly overestimate the sealing force. More research should be conducted to obtain bulk modulus data for different elastomer materials and compounds, and how the bulk modulus change with time, temperature, exposure to fluids etc.

REFERENCES

[1] Anand, L. A constitutive model for compressible elastomeric solids. *Computational Mechanics 18*, 5 (1996), 339–355.

[2] Arruda, E. M., and Boyce, M. C. A three-dimensional constitutive model for the large stretch behavior of rubber elastic materials. *Journal of the Mechanics and Physics of Solids 41*, 2 (1993), 389–412.

[3] Bergström, J. S., and Boyce, M. C. Mechanical Behavior of Particle Filled Elastomers. *Rubber Chemistry and Technology 72*, 4 (1999), 633–656.

[4] Bischoff, J. E., Arruda, E. M., and Grosh, K. A new constitutive model for the compressibility of elastomers at finite deformations. *Rubber Chemistry and Technology 74*, 4 (2001), 541–559.

[5] Boyce, M. C., and Arruda, E. M. Constitutive models of rubber elasticity: A review. *Rubber Chemistry and Technology 73*, 3 (2000), 504–523.

[6] Bradley, G. L., Chang, P. C., and McKenna, G. B. Rubber modeling using uniaxial test data. *Journal of Applied Polymer Science 81*, 4 (2001), 837–848.

[7] Bridgman, P. W. The Compression of Sixty-One Solid Substances to 25,000 kg/cm2 Determined by a New Rapid Method. *Proceedings of the American Academy of Arts and Sciences 76*, 1 (1945), 9–24.

[8] Fagerholt, E. *Field measurements in mechanical testing using close-range photogrammetry and digital image analysis*. Phd thesis, 2012.

[9] Flory, P. J. Thermodynamic relations for high elastic materials. *Transactions of the Faraday Society 57*, 0 (1961), 829–838.

[10] Harris, C., and Stephens, M. A combined corner and edge detector. In *Alvey vision conference* (1988), vol. 15, Manchester, UK, p. 50.

[11] ISO. 10423:2009 Petroleum and natural gas industries – Drilling and production equipment – Wellhead and christmas tree equipment. Report, International Organization for Standardization, 2009.

[12] Miehe, C., Stein, E., and Wagner, W. Associative multiplicative elastoplasticity: Formulation and aspects of the numerical implementation including stability analysis. *Computers and Structures 52*, 5 (1994), 969–978.

[13] Ogden, R. W. Large deformation isotropic elasticity-on the correlation of theory and experiment for incompressible rubberlike solids. *Proceedings of the Royal Society of London. A. Mathematical and Physical Sciences 326*, 1567 (1972), 565–584.

[14] Rivlin, R. S. Large Elastic Deformations of Isotropic Materials. I. Fundamental Concepts. *Philosophical Transactions of the Royal Society of London. Series A, Mathematical and Physical Sciences 240*, 822 (1948), 459–490.

[15] Treloar, L. R. G. The elasticity of a network of long-chain molecules.iii. *Trans. Faraday Soc. 42* (1946), 83–94.

[16] Treloar, L. R. G. *The Physics of Rubber Elasticity.* OUP Oxford, 2005.

[17] Wood, L. A., and Martin, G. M. Compressibility of Natural Rubber at Pressures Below 500 KG/CM2. *Rubber Chemistry and Technology 37*, 4 (1964), 850–865.

[18] Yeoh, O. H. Some forms of the strain energy function for rubber. *Rubber Chemistry and Technology 66*, 5 (1993), 754–771.

A.2

Arne Ilseng, Bjørn H. Skallerud, Arild H. Clausen

Volumetric compression of HNBR and FKM elastomers

Constitutive Models for Rubber IX – Proceedings of the 9th European Conference on Constitutive Models for Rubbers, 2015, pp. 235-241, ISBN:978-1-138-02873-9

A.2

Volumetric compression of HNBR and FKM elastomers

A. Ilseng, B.H. Skallerud & A.H. Clausen
Department of Structural Engineering
Norwegian University of Science and Technology, Trondheim, Norway.

ABSTRACT: Due to their highly confined service condition and exposure to large hydrostatic pressures, the correct compressibility level is an important parameter for the numerical analysis of elastomeric seals. A volumetric compression rig, enabling the measurement of the frictional force throughout the test, was designed. Six different elastomer compounds, all commonly used in the oil and gas industry, were exposed to cyclic volumetric compression to a hydrostatic pressure level of 140 MPa. As opposed to deviatoric compression, no significant stress softening was observed between the volumetric compression cycles. For the pressure - volume ratio relation obtained for the elastomers, a second order polynomial gave a very good resemblance of the experimental data. At the maximum hydrostatic pressure, the six compounds showed a volume ratio between 0.93 and 0.94. Volumetric creep tests with 30 minutes at a constant hydrostatic pressure of 140 MPa were also conducted. Limited volumetric creep was observed for all compounds, with a maximum measured volume change of 0.35%. A numerical case study was conducted to address implications of the obtained experimental results.

1 INTRODUCTION

Unexpected failure of elastomer seals is an expensive issue for the oil and gas industry. Increased use of numerical calculations, such as finite element simulations, during the design process of seals can possibly reduce the occurrence of such undesired events. For numerical simulations to be predictive and useful, a correct description of the material behaviour is of outmost importance. Elastomer seals in the oil and gas industry are exposed to extreme service conditions facing large temperature variations, pressure variations, exposure to production fluids etc. To obtain predictive results for seal performance the effect of all these challenges must be quantitatively given. This paper will be limited to the effect of pressure variations. By design, elastomeric seals are in a highly confined configuration, and they can today be qualified for service pressures as high as 138 MPa (ISO 2009).

Elastomeric materials are known to have a bulk modulus multiple orders of magnitude larger than their shear modulus. A large bulk to shear modulus ratio means that the material would change its shape rather than changing its volume, leading to a close to incompressible behaviour (e.g. no change of volume) during an unconfined deformation. Assuming incompressible behaviour of elastomers can facilitate powerful analytical solutions for simple geometries and loading situations (see, among others, the work by Treloar (1975) and Ogden (2013)). In situations that are more complex though, the use of numerical methods, like finite element simulations, are often necessary to obtain predictive results. In such simulations, a rather arbitrary level of slight compressibility is normally included to avoid numerical difficulties like element locking. For unconfined deformations, this assumption normally gives satisfactory results, although Destrade et al. (2012) showed that the normal stresses in shearing deformation could be sensitive to the compressibility level used. When the material is highly confined and exposed to large hydrostatic pressure, as is the case for seals, a precise level of the compressibility is needed to obtain predictive results (see the work by Zimmermann & Stommel (2013) for a further discussion).

The level of material compressibility can be measured in different manners and Horgan & Murphy (2009) presented a description of these methods in their work. Boyce & Arruda (2000) reviewed experimental data and material models for elastomer compressibility present in the literature at that time. In the following section, literature data for the pressure - volume ratio relation of elastomers are presented and discussed. In Section 3, the experimental work is described. Section 4 presents and discuss the experimental results. Implications of the obtained material data for numerical modelling of a seal case are exemplified in Section 5, while some concluding remarks are given in Section 6.

2 LITERATURE DATA

In the literature today, only a few studies present data for the compressibility of elastomers under hydrostatic pressure. Figure 1 shows data from the studies by Bridgman (1945), Wood & Martin (1964), and Bradley et al. (2001). The measured pressure levels are plotted versus the volume ratio J, i.e. the current volume divided by the reference volume.

Bridgman (1945) tested fourteen different elastomeric materials, more specifically two natural rubbers and twelve synthetic elastomers. The pressure level used in Bridgman's study was rather extreme with a maximum pressure of 25 000 kg/cm^2 and the first data point logged at 2 000 kg/cm^2 $\approx$ 200 MPa. In Figure 1 the two first data points for the most and least compressible materials, being hevea gum and Duprene respectively, are included.

Wood & Martin (1964) presented data for the compressibility of a *"peroxide cured vulcanizate of natural rubber"* for a temperature range of 0-25°C and up to a pressure of 50 MPa. A clear temperature dependency of the compressibility was reported, with an increasing compressibility for an increasing temperature. The results obtained at 25°C are presented in Figure 1.

Bradley et al. (2001) obtained compressibility data for a *"carbon black-reinforced rubber compound of the same composition as that used in the manufacture of the elastomeric bearings"*, with a pressure range up to 150 MPa. These data are presented in Figure 1.

Based on the rather limited data in the literature, it seems that elastomeric materials have a linear volume - pressure relation for a hydrostatic pressure below 200 MPa, while (Bridgman 1945) suggests a non-linear behaviour for the pressure range above 200 MPa. A challenge with this assumption is that the materials showing the non-linear effects have the first data points at 200 MPa, possibly concealing non-linear behaviour in the lower pressure regime. It is anyway clear that it appears to be a significant difference in compressibility for different elastomer materials. None of the studies in the literature deals with materials commonly used for sealing in the oil and gas industry.

3 EXPERIMENTAL WORK

3.1 *Materials*

This study deals with the compressibility of hydrogenated nitrile butadiene rubber (HNBR) and fluoroelastomer (FKM). These materials are commonly used as sealing materials in the oil and gas industry due to their great chemical resistance. To get an idea of differences in volumetric behaviour for different compounds with the same polymer basis, four different HNBR and two different FKM compounds were tested. While all compounds have a HNBR or FKM

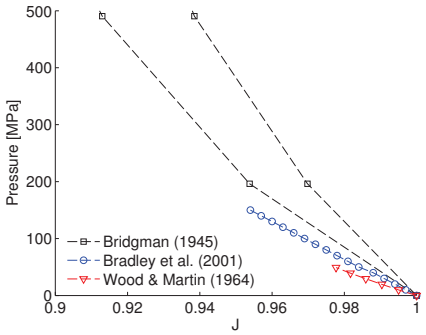

Figure 1: Literature data of volume change up to a pressure of 500 MPa. Data adapted from Bridgman (1945), Bradley et al. (2001), and Wood & Martin (1964).

Table 1: List of compounds with height, diameter, and density measured prior to testing.

Compound	Height [mm]	Diameter [mm]	Density [g/cm^3]
HNBR1	12.90	28.67	1.29
HNBR2	12.46	28.88	1.23
HNBR3	12.50	28.94	1.29
HNBR4	12.43	28.98	1.16
FKM1	12.57	28.87	2.33
FKM2	12.43	28.86	1.84

polymer basis, the amount of fillers, bonding promoters etc. vary between the different compounds. The labels HNBR1, HNBR2, and so on are used to identify the different compounds.

Specimens with dimensions according to the ISO standard for compression testing of elastomers (ISO 2014), having a diameter of 29 mm and height of 12.5 mm, were ordered from different suppliers. Dimensions and densities measured prior to testing are presented in Table 1. A thin layer of silicone grease was applied to all surfaces of the specimens as lubrication. This was found to significantly reduce the frictional forces, especially for the two FKM compounds.

3.2 *Set-up*

A rig for volumetric compression testing was designed to be used with an Instron 5982 universal testing machine with a t-slot table. The layout of the test set-up is illustrated in Figure 2. It involves two pistons with load cells and a 20 mm thick steel plate supported on four bolts. The centre hole of the steel plate was produced with a diameter of 29 mm and a tolerance of +0.05 mm, −0.00 mm. To ensure a tight fit, the upper and lower pistons were machined with a diameter of 29 mm and a tolerance of +0.00 mm, −0.05 mm. The plate was fixed to the t-slot table of the testing machine by four steel bolts, while the two pistons were screwed onto the load cells. In addition to the 100 kN load cell of the test machine, an HBM U2A 100 kN load cell was included below the specimen, fixed to the t-slot table with bolts. The frictional forces arising between the elastomer specimen

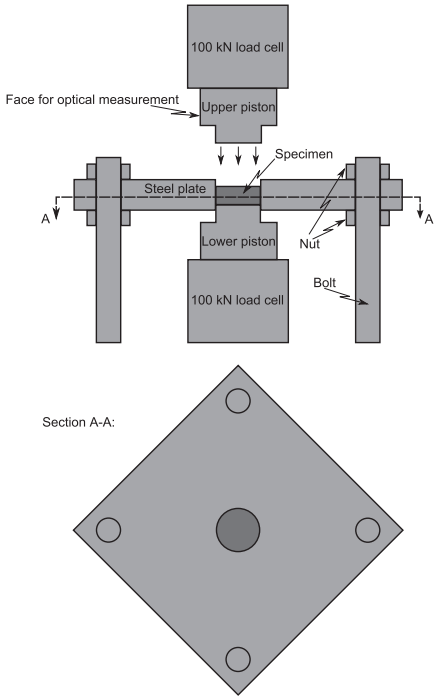

Figure 2: Sketch of the test set-up, section view (upper part) and cross-sectional view (lower part).

and the steel plate were determined as the difference between the forces measured by the two load cells. The frictional forces are in the following defined as positive working towards the upper load cell of the system in Figure 2. To avoid uncertainties in the displacement measurements due to the machine compliance, a checkerboard pattern was applied to the upper piston. By logging pictures of this pattern during the deformation, the displacement was calculated by use of a point tracker routine (Harris & Stephens 1988). It was assumed that the test set-up, which was made of steel, was fully rigid and that all deformation therefore occurred in the specimen.

3.3 *Procedure*

To obtain results representative for the general long-term behaviour of the elastomers, six cycles of deformation were applied. A force level of 95 kN in the upper load cell, corresponding to a pressure level of 140 MPa, was applied by load control, before returning to 0.1 kN and starting a new cycle. In the sixth cycle, the force level in the upper load cell was held constant at 95 kN for 30 minutes before returning to 0.1 kN. During loading/unloading a deformation rate of 3 mm/min was applied. Volumetric data are extracted from the fifth cycle and for the hold period of the sixth cycle. The test procedure is indicated in Figure 3.

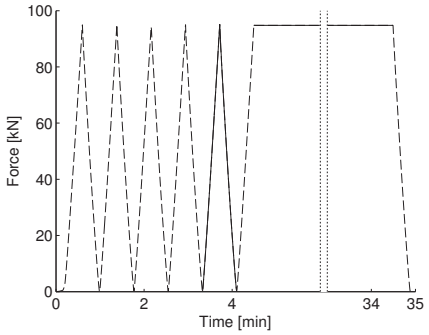

Figure 3: Force level during testing of HNBR1. A solid line indicates the fifth cycle and the hold period. The time axis is broken from 6 to 33 minutes to enhance readability.

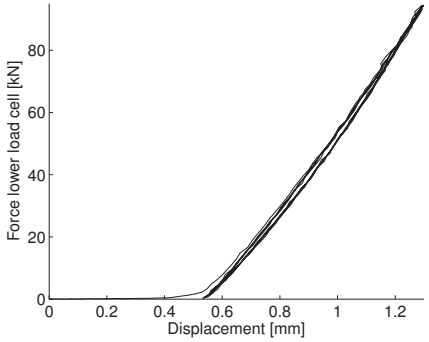

Figure 4: First five deformation cycles - HNBR1.

4 EXPERIMENTAL RESULTS

4.1 *Repeatability of cycles*

The force-displacement curve for the first five deformation cycles of the HNBR1 compound is shown in Figure 4. It is seen that for the first cycle the force level increased slowly until approximately 0.5 mm of deformation. During this first part of deformation, it is assumed that the specimen deforms deviatorically to get in full contact with the enclosing steel plate. When full contact is obtained the volumetric compression begins, leading to a stiffer response. The amount of initial deformation was significantly lower for the other materials, having a larger initial diameter as shown in Table 1. From the second to the fifth deformation cycle no clear difference can be seen in the force-displacement relation. A similar repeatability between cycles was found for all compounds tested. It should be noted that no Mullins softening (Mullins 1948) could be observed between the cycles. This suggests that the softening effect observed for unconfined cyclic deformation of elastomer materials is an effect related to the deviatoric part of the material behaviour.

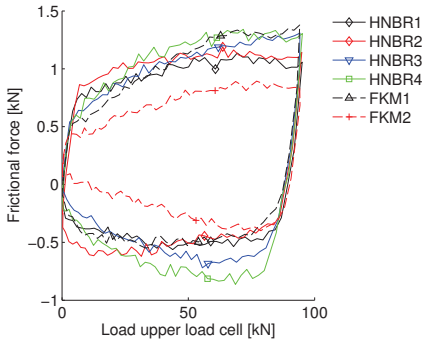

Figure 5: Frictional force measured for all tests. Friction is defined as positive working towards the upper load cell.

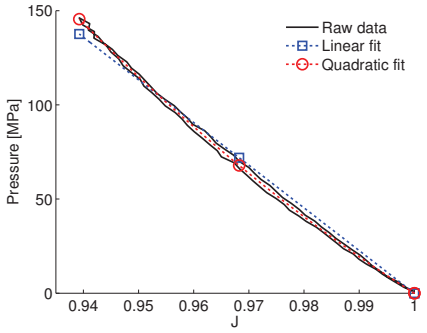

Figure 6: Linear and quadratic polynomial fit to raw data for HNBR1.

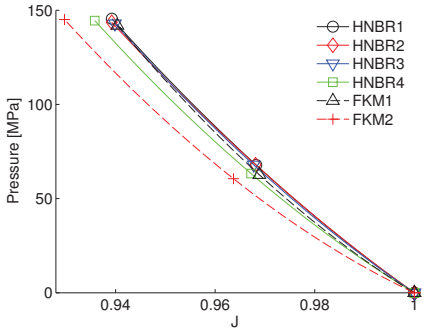

Figure 7: Fitted compressibility data for all compounds.

4.2 *Frictional forces*

The frictional forces measured for all tests are shown in Figure 5. The maximum friction was obtained for the FKM1 compound, with a peak force of 1.3 kN (less than 1.4% of the force in the upper load cell). Thereby, the frictional forces are neglected in the following calculations of hydrostatic pressure.

4.3 *Volumetric deformation*

The volume ratio of the material can be described by

$$J = \frac{V}{V_0} = \frac{H}{H_0} \tag{1}$$

where J is the volume ratio, V is the current volume of the material, V_0 is the initial volume of the material, H is the current height of the specimen, and H_0 is the initial height of the specimen. In Equation 1, it is assumed that the specimen perfectly fills the hole of the rigid steel plate, leading to a constant cross sectional area of the specimen throughout the deformation. For an incompressible material, J equals unity at all times.

The volume change of the material due to hydrostatic pressure was calculated for the fifth deformation cycle. The pressure level was obtained by dividing the force in the lower load cell by the area of the hole in the steel plate. To enhance readability, a polynomial function was adapted to the raw loading/unloading data by use of a least squares method. Based on this fit, the pressure and volume ratio were calculated. As an example, a linear and a quadratic fit are shown for the HNBR1 compound in Figure 6. It is seen that the quadratic fit represents the raw data very well, while the linear fit is slightly less suited to capture the observed material behaviour. This trend was representative for all compounds tested. The resulting quadratic polynomial fit of the pressure - volume ratio data is presented for all compounds in Figure 7. It is seen that while the HNBR materials (solid lines) have a relatively low discrepancy of compressibility, the two FKM materials (dashed lines) have a larger difference in compressibility, with the FKM2 compound being clearly more compressible than the FKM1 compound. In contrast to the data for other elastomers presented in the literature, see Section 2, non-linear pressure response is clearly present also below the pressure level of 200 MPa for the materials tested. The volume ratio obtained at maximum pressure was between 0.93 and 0.94 for all compounds. It should be noted, that for an equal level of pressure the compressibility observed in the literature data is significantly lower, with a volume ratio of 0.954 at 150 MPa in the data from Bradley et al. (2001), see Figure 1.

4.4 *Volumetric creep*

For the period of constant force in the sixth cycle, the relative displacement logged by the machine was used to measure the volume creep of the materials. This is justified by assuming that the machine compliance is a function of the force level and thereby constant during the period of constant force. To enhance readability the data were smoothed by a moving average algorithm. Figure 8 presents the volumetric creep normalized with respect to the observed volume at the start of the creep period. It can be seen that the relative creep that occurred in the compounds was low, with

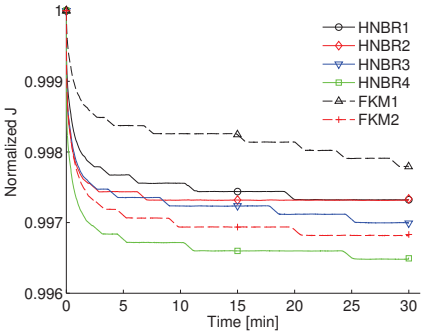

Figure 8: Relative volumetric creep for all compounds.

HNBR4 displaying the largest creep with a volume reduction of approximately 0.35% during 30 minutes. It should be noted that while HNBR4 has the lowest density, it displayed the largest volumetric creep. On the other hand, FKM1 has the largest density combined with the lowest volumetric creep.

5 IMPLICATIONS FOR NUMERICAL MODELLING

5.1 *Test case*

To exemplify the effect of material compressibility for typical seal behaviour, an axisymmetric model with a square cross section was studied numerically. The studied seal had an internal diameter of 200 mm and a width of 8.4 mm. Analytically rigid plates were modelled to enclose the seal. A sketch of the geometry is shown in Figure 9. The loading of the seal was applied in two steps, first the vertical rigid plate was displaced in negative x-direction to reduce the width of the specimen by 15%, and thereafter the introduction of a fluid in the upper chamber was simulated by applying a pressure load of 100 MPa on the upper surface of the seal. The axisymmetric geometry of the seal was discretized by 10 000 CAX8RH elements in Abaqus/Standard. A surface-to-surface contact algorithm was used to enforce the contact between the elastomer and the rigid casing. The normal behaviour was modelled as hard-contact by a direct method, while linear friction behaviour was assumed for the tangential behaviour, using a penalty method.

5.2 *Material modelling*

The simple compressible neo-Hookean model implemented in Abaqus was used. The strain energy potential is defined as

$$U = \frac{\mu_0}{2}\left(\bar{I}_1 - 3\right) + \frac{\kappa_0}{2}\left(J-1\right)^2 \tag{2}$$

where μ_0 is the shear modulus of the material, κ_0 the bulk modulus, and $\bar{I}_1$ is the incompressible first strain

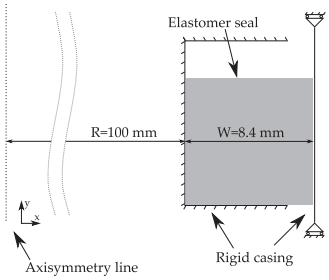

Figure 9: Sketch of axisymmetric model.

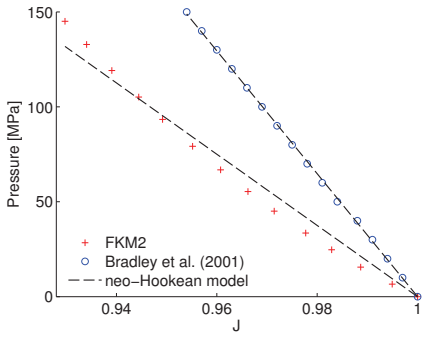

Figure 10: Fit of compressible part of neo-Hookean model to FKM2 data and the data from Bradley et al. (2001).

invariant. From the strain energy potential the volumetric part of the stress can be found as

$$\boldsymbol{\sigma}_{vol} = \frac{\partial U}{\partial J}\mathbf{I} = \kappa_0\left(J-1\right)\mathbf{I} \tag{3}$$

where $\mathbf{I}$ denotes the second order unit tensor. The material parameter κ_0 can be found by fitting Equation 3 to experimental data.

To indicate the implication of the experimental results, three simulations were run with different compressibility levels; based on experimental data for FKM2, based on data from Bradley et al. (2001), and assuming material incompressibility. The curves for a least squares fit of the volumetric part of the neo-Hookean model to the test data for the FKM2 and the Bradley et al. (2001) data are shown in Figure 10. It is seen that a reasonable fit with the FKM2 material was obtained with $\kappa_0 = 1.88$ GPa, although the non-linear material behaviour is not captured by the model. For the Bradley et al. (2001) data on the other hand, a very good fit was obtained with $\kappa_0 = 3.24$ GPa. For all simulations, the shear modulus was kept constant at 5.7 MPa and the elastomer-steel friction was 0.012.

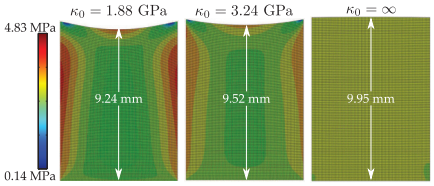

Figure 11: Resulting contour plots for different levels of compressibility.

5.3 *Results*

Resulting contour plots of the Mises stress, defined by

$$\sigma_{Mises} = \sqrt{\frac{3}{2}\boldsymbol{\sigma}_{dev} : \boldsymbol{\sigma}_{dev}} \tag{4}$$

where $\boldsymbol{\sigma}_{dev}$ is the deviatoric part of the Cauchy stress tensor, in the end configuration is shown in Figure 11. It can be seen that the compressibility level effects the geometrical shape as well as the level of the Mises stress. The maximum Mises stress obtained from the FKM2 data was 4.83 MPa, using the Bradley et al. data a maximum Mises stress of 4.28 MPa was obtained, while for the incompressible case a maximum of 3.83 MPa was found. It should be noted that the incompressibility assumption leads to an underestimated Mises stress in the seal. For the geometry of the seal, it is seen that the incompressible case retained a nearly rectangular shape in the end configuration, while the compressible seals got a significant deformation of the upper surface. As indicated in Figure 11, the height of the centre line was 9.95 mm for the incompressible simulation, 9.52 mm using the Bradley et al. data, and 9.24 mm with the FKM2 data.

6 CONCLUSIONS

Six elastomers, four HNBR compounds and two FKM compounds, were tested in volumetric compression. Under cyclic volumetric deformation there was seen no sign of softening in the HNBR and FKM elastomers tested herein. For the general volumetric behaviour, a second order polynomial was seen to give a very good fit for the relation between volume ratio and hydrostatic pressure. This is in contrast to the data presented in the literature, which indicate a linear relation between volume ratio and pressure for hydrostatic pressures below 200 MPa. It should also be noted that the compressibility of the materials tested herein is significantly larger than what is indicated in the literature data. The volumetric creep during constant hydrostatic pressure was found to be relatively low with a change in the volume ratio of less than 0.35% during a 30 min hold time. There might also be a correlation between material density and volumetric creep, with increased creep for reduced density. Comparing the four HNBR compounds with the two FKM compounds, there was no clear trend that one of the material groups have a higher compressibility than the other has, or achieve more volumetric creep deformation. Through a numerical study of an example case, it was shown that the incompressibility assumption led to a reduced maximum Mises stress for a typical sealing application compared with the experimental compressibility levels. In addition, there was a significant change of the geometry in the end configuration as the material compressibility was introduced.

REFERENCES

Boyce, M. C. & E. M. Arruda (2000). Constitutive models of rubber elasticity: A review. *Rubber Chemistry and Technology 73*(3), 504–523.

Bradley, G. L., P. C. Chang, & G. B. McKenna (2001). Rubber modeling using uniaxial test data. *Journal of Applied Polymer Science 81*(4), 837–848.

Bridgman, P. W. (1945). The Compression of Sixty-One Solid Substances to 25,000 kg/cm2 Determined by a New Rapid Method. *Proceedings of the American Academy of Arts and Sciences 76*(1), 9–24.

Destrade, M., M. D. Gilchrist, J. Motherway, & J. G. Murphy (2012). Slight compressibility and sensitivity to changes in Poisson's ratio. *International Journal for Numerical Methods in Engineering 90*(4), 403–411.

Harris, C. & M. Stephens (1988). A combined corner and edge detector. In *Alvey vision conference*, Volume 15, pp. 50. Manchester, UK.

Horgan, C. O. & J. G. Murphy (2009). Compression tests and constitutive models for the slight compressibility of elastic rubber-like materials. *International Journal of Engineering Science 47*(11-12), 1232–1239.

ISO (2009). 10423:2009 Petroleum and natural gas industries – Drilling and production equipment – Wellhead and christmas tree equipment. Report, International Organization for Standardization.

ISO (2014). 815-1:2014 Rubber, vulcanized or thermoplastic – Determination of compression set – Part 1: At ambient or elevated temperatures. Report, International Organization for Standardization.

Mullins, L. (1948). Effect of Stretching on the Properties of Rubber. *Rubber Chemistry and Technology 21*(2), 281–300.

Ogden, R. (2013). *Non-Linear Elastic Deformations*. Dover Civil and Mechanical Engineering. Dover Publications.

Treloar, L. R. G. (1975). *The physics of rubber elasticity*. Oxford university press.

Wood, L. A. & G. M. Martin (1964). Compressibility of Natural Rubber at Pressures Below 500 KG/CM2. *Rubber Chemistry and Technology 37*(4), 850–865.

Zimmermann, J. & M. Stommel (2013). The mechanical behaviour of rubber under hydrostatic compression and the effect on the results of finite element analyses. *Archive of Applied Mechanics 83*(2), 293–302.

DEPARTMENT OF STRUCTURAL ENGINEERING
NORWEGIAN UNIVERSITY OF SCIENCE AND TECHNOLOGY

N–7491 TRONDHEIM, NORWAY
Telephone: +47 73 59 47 00 Telefax: +47 73 59 47 01

"Reliability Analysis of Structural Systems using Nonlinear Finite Element Methods",
C. A. Holm, 1990:23, ISBN 82-7119-178-0.

"Uniform Stratified Flow Interaction with a Submerged Horizontal Cylinder",
Ø. Arntsen, 1990:32, ISBN 82-7119-188-8.

"Large Displacement Analysis of Flexible and Rigid Systems Considering
Displacement-Dependent Loads and Nonlinear Constraints",
K. M. Mathisen, 1990:33, ISBN 82-7119-189-6.

"Solid Mechanics and Material Models including Large Deformations",
E. Levold, 1990:56, ISBN 82-7119-214-0, ISSN 0802-3271.

"Inelastic Deformation Capacity of Flexurally-Loaded Aluminium Alloy Structures",
T. Welo, 1990:62, ISBN 82-7119-220-5, ISSN 0802-3271.

"Visualization of Results from Mechanical Engineering Analysis",
K. Aamnes, 1990:63, ISBN 82-7119-221-3, ISSN 0802-3271.

"Object-Oriented Product Modeling for Structural Design",
S. I. Dale, 1991:6, ISBN 82-7119-258-2, ISSN 0802-3271.

"Parallel Techniques for Solving Finite Element Problems on Transputer Networks",
T. H. Hansen, 1991:19, ISBN 82-7119-273-6, ISSN 0802-3271.

"Statistical Description and Estimation of Ocean Drift Ice Environments",
R. Korsnes, 1991:24, ISBN 82-7119-278-7, ISSN 0802-3271.

“Properties of concrete related to fatigue damage: with emphasis on high strength concrete”,
G. Petkovic, 1991:35, ISBN 82-7119-290-6, ISSN 0802-3271.

"Turbidity Current Modelling",
B. Brørs, 1991:38, ISBN 82-7119-293-0, ISSN 0802-3271.

"Zero-Slump Concrete: Rheology, Degree of Compaction and Strength. Effects of Fillers as Part Cement-Replacement",
C. Sørensen, 1992:8, ISBN 82-7119-357-0, ISSN 0802-3271.

"Nonlinear Analysis of Reinforced Concrete Structures Exposed to Transient Loading",
K. V. Høiseth, 1992:15, ISBN 82-7119-364-3, ISSN 0802-3271.

"Finite Element Formulations and Solution Algorithms for Buckling and Collapse Analysis of Thin Shells",
R. O. Bjærum, 1992:30, ISBN 82-7119-380-5, ISSN 0802-3271.

"Response Statistics of Nonlinear Dynamic Systems",
J. M. Johnsen, 1992:42, ISBN 82-7119-393-7, ISSN 0802-3271.

"Digital Models in Engineering. A Study on why and how engineers build and operate digital models for decisison support",
J. Høyte, 1992:75, ISBN 82-7119-429-1, ISSN 0802-3271.

"Sparse Solution of Finite Element Equations",
A. C. Damhaug, 1992:76, ISBN 82-7119-430-5, ISSN 0802-3271.

"Some Aspects of Floating Ice Related to Sea Surface Operations in the Barents Sea",
S. Løset, 1992:95, ISBN 82-7119-452-6, ISSN 0802-3271.

"Modelling of Cyclic Plasticity with Application to Steel and Aluminium Structures",
O. S. Hopperstad, 1993:7, ISBN 82-7119-461-5, ISSN 0802-3271.

"The Free Formulation: Linear Theory and Extensions with Applications to Tetrahedral Elements
with Rotational Freedoms",
G. Skeie, 1993:17, ISBN 82-7119-472-0, ISSN 0802-3271.

"Høyfast betongs motstand mot piggdekkslitasje. Analyse av resultater fra prøving i Veisliter'n",
T. Tveter, 1993:62, ISBN 82-7119-522-0, ISSN 0802-3271.

"A Nonlinear Finite Element Based on Free Formulation Theory for Analysis of Sandwich Structures",
O. Aamlid, 1993:72, ISBN 82-7119-534-4, ISSN 0802-3271.

"The Effect of Curing Temperature and Silica Fume on Chloride Migration and Pore Structure of High Strength Concrete",
C. J. Hauck, 1993:90, ISBN 82-7119-553-0, ISSN 0802-3271.

"Failure of Concrete under Compressive Strain Gradients",
G. Markeset, 1993:110, ISBN 82-7119-575-1, ISSN 0802-3271.

"An experimental study of internal tidal amphidromes in Vestfjorden",
J. H. Nilsen, 1994:39, ISBN 82-7119-640-5, ISSN 0802-3271.

"Structural analysis of oil wells with emphasis on conductor design",
H. Larsen, 1994:46, ISBN 82-7119-648-0, ISSN 0802-3271.

"Adaptive methods for non-linear finite element analysis of shell structures",
K. M. Okstad, 1994:66, ISBN 82-7119-670-7, ISSN 0802-3271.

"On constitutive modelling in nonlinear analysis of concrete structures",
O. Fyrileiv, 1994:115, ISBN 82-7119-725-8, ISSN 0802-3271.

"Fluctuating wind load and response of a line-like engineering structure with emphasis on motion-induced wind forces",
J. Bogunovic Jakobsen, 1995:62, ISBN 82-7119-809-2, ISSN 0802-3271.

"An experimental study of beam-columns subjected to combined torsion, bending and axial actions",
A. Aalberg, 1995:66, ISBN 82-7119-813-0, ISSN 0802-3271.

"Scaling and cracking in unsealed freeze/thaw testing of Portland cement and silica fume concretes",
S. Jacobsen, 1995:101, ISBN 82-7119-851-3, ISSN 0802-3271.

"Damping of water waves by submerged vegetation. A case study of laminaria hyperborea",
A. M. Dubi, 1995:108, ISBN 82-7119-859-9, ISSN 0802-3271.

"The dynamics of a slope current in the Barents Sea",
Sheng Li, 1995:109, ISBN 82-7119-860-2, ISSN 0802-3271.

"Modellering av delmaterialenes betydning for betongens konsistens",
Ernst Mørtsell, 1996:12, ISBN 82-7119-894-7, ISSN 0802-3271.

"Bending of thin-walled aluminium extrusions",
Birgit Søvik Opheim, 1996:60, ISBN 82-7119-947-1, ISSN 0802-3271.

"Material modelling of aluminium for crashworthiness analysis",
Torodd Berstad, 1996:89, ISBN 82-7119-980-3, ISSN 0802-3271.

"Estimation of structural parameters from response measurements on submerged floating tunnels",
Rolf Magne Larssen, 1996:119, ISBN 82-471-0014-2, ISSN 0802-3271.

“Numerical modelling of plain and reinforced concrete by damage mechanics”,
Mario A. Polanco-Loria, 1997:20, ISBN 82-471-0049-5, ISSN 0802-3271.

“Nonlinear random vibrations - numerical analysis by path integration methods”,
Vibeke Moe, 1997:26, ISBN 82-471-0056-8, ISSN 0802-3271.

"Numerical prediction of vortex-induced vibration by the finite element method",
Joar Martin Dalheim, 1997:63, ISBN 82-471-0096-7, ISSN 0802-3271.

"Time domain calculations of buffeting response for wind sensitive structures",
Ketil Aas-Jakobsen, 1997:148, ISBN 82-471-0189-0, ISSN 0802-3271.

"A numerical study of flow about fixed and flexibly mounted circular cylinders",
Trond Stokka Meling, 1998:48, ISBN 82-471-0244-7, ISSN 0802-3271.

"Estimation of chloride penetration into concrete bridges in coastal areas",
Per Egil Steen, 1998:89, ISBN 82-471-0290-0, ISSN 0802-3271.

"Stress-resultant material models for reinforced concrete plates and shells",
Jan Arve Øverli, 1998:95, ISBN 82-471-0297-8, ISSN 0802-3271.

"Chloride binding in concrete. Effect of surrounding environment and concrete composition",
Claus Kenneth Larsen, 1998:101, ISBN 82-471-0337-0, ISSN 0802-3271.

"Rotational capacity of aluminium alloy beams",
Lars A. Moen, 1999:1, ISBN 82-471-0365-6, ISSN 0802-3271.

"Stretch Bending of Aluminium Extrusions",
Arild H. Clausen, 1999:29, ISBN 82-471-0396-6, ISSN 0802-3271.

"Aluminium and Steel Beams under Concentrated Loading",
Tore Tryland, 1999:30, ISBN 82-471-0397-4, ISSN 0802-3271.

"Engineering Models of Elastoplasticity and Fracture for Aluminium Alloys",
Odd-Geir Lademo, 1999:39, ISBN 82-471-0406-7, ISSN 0802-3271.

"Kapasitet og duktilitet av dybelforbindelser i trekonstruksjoner",
Jan Siem, 1999:46, ISBN 82-471-0414-8, ISSN 0802-3271.

"Etablering av distribuert ingeniørarbeid; Teknologiske og organisatoriske erfaringer fra en norsk ingeniørbedrift",
Lars Line, 1999:52, ISBN 82-471-0420-2, ISSN 0802-3271.

"Estimation of Earthquake-Induced Response",
Símon Ólafsson, 1999:73, ISBN 82-471-0443-1, ISSN 0802-3271.

"Coastal Concrete Bridges: Moisture State, Chloride Permeability and Aging Effects"
Ragnhild Holen Relling, 1999:74, ISBN 82-471-0445-8, ISSN 0802-3271.

"Capacity Assessment of Titanium Pipes Subjected to Bending and External Pressure",
Arve Bjørset, 1999:100, ISBN 82-471-0473-3, ISSN 0802-3271.

“Validation of Numerical Collapse Behaviour of Thin-Walled Corrugated Panels”,
Håvar Ilstad, 1999:101, ISBN 82-471-0474-1, ISSN 0802-3271.

“Strength and Ductility of Welded Structures in Aluminium Alloys”,
Miroslaw Matusiak, 1999:113, ISBN 82-471-0487-3, ISSN 0802-3271.

“Thermal Dilation and Autogenous Deformation as Driving Forces to Self-Induced Stresses in High Performance Concrete”,
Øyvind Bjøntegaard, 1999:121, ISBN 82-7984-002-8, ISSN 0802-3271.

“Some Aspects of Ski Base Sliding Friction and Ski Base Structure”,
Dag Anders Moldestad, 1999:137, ISBN 82-7984-019-2, ISSN 0802-3271.

"Electrode reactions and corrosion resistance for steel in mortar and concrete",
Roy Antonsen, 2000:10, ISBN 82-7984-030-3, ISSN 0802-3271.

"Hydro-Physical Conditions in Kelp Forests and the Effect on Wave Damping and Dune Erosion. A case study on Laminaria Hyperborea",
Stig Magnar Løvås, 2000:28, ISBN 82-7984-050-8, ISSN 0802-3271.

"Random Vibration and the Path Integral Method",
Christian Skaug, 2000:39, ISBN 82-7984-061-3, ISSN 0802-3271.

"Buckling and geometrical nonlinear beam-type analyses of timber structures",
Trond Even Eggen, 2000:56, ISBN 82-7984-081-8, ISSN 0802-3271.

”Structural Crashworthiness of Aluminium Foam-Based Components”,
Arve Grønsund Hanssen, 2000:76, ISBN 82-7984-102-4, ISSN 0809-103X.

“Measurements and simulations of the consolidation in first-year sea ice ridges, and some aspects of mechanical behaviour”,
Knut V. Høyland, 2000:94, ISBN 82-7984-121-0, ISSN 0809-103X.

”Kinematics in Regular and Irregular Waves based on a Lagrangian Formulation”,
Svein Helge Gjøsund, 2000-86, ISBN 82-7984-112-1, ISSN 0809-103X.

”Self-Induced Cracking Problems in Hardening Concrete Structures”,
Daniela Bosnjak, 2000-121, ISBN 82-7984-151-2, ISSN 0809-103X.

"Ballistic Penetration and Perforation of Steel Plates",
Tore Børvik, 2000:124, ISBN 82-7984-154-7, ISSN 0809-103X.

"Freeze-Thaw resistance of Concrete. Effect of: Curing Conditions, Moisture Exchange and Materials",
Terje Finnerup Rønning, 2001:14, ISBN 82-7984-165-2, ISSN 0809-103X

"Structural behaviour of post tensioned concrete structures. Flat slab. Slabs on ground",
Steinar Trygstad, 2001:52, ISBN 82-471-5314-9, ISSN 0809-103X.

"Slipforming of Vertical Concrete Structures. Friction between concrete and slipform panel",
Kjell Tore Fosså, 2001:61, ISBN 82-471-5325-4, ISSN 0809-103X.

"Some numerical methods for the simulation of laminar and turbulent incompressible flows",
Jens Holmen, 2002:6, ISBN 82-471-5396-3, ISSN 0809-103X.

“Improved Fatigue Performance of Threaded Drillstring Connections by Cold Rolling”,
Steinar Kristoffersen, 2002:11, ISBN: 82-421-5402-1, ISSN 0809-103X.

"Deformations in Concrete Cantilever Bridges: Observations and Theoretical Modelling",
Peter F. Takâcs, 2002:23, ISBN 82-471-5415-3, ISSN 0809-103X.

"Stiffened aluminium plates subjected to impact loading",
Hilde Giæver Hildrum, 2002:69, ISBN 82-471-5467-6, ISSN 0809-103X.

"Full- and model scale study of wind effects on a medium-rise building in a built up area",
Jónas Thór Snæbjørnsson, 2002:95, ISBN82-471-5495-1, ISSN 0809-103X.

“Evaluation of Concepts for Loading of Hydrocarbons in Ice-infested water”,
Arnor Jensen, 2002:114, ISBN 82-417-5506-0, ISSN 0809-103X.

”Numerical and Physical Modelling of Oil Spreading in Broken Ice”,
Janne K. Økland Gjøsteen, 2002:130, ISBN 82-471-5523-0, ISSN 0809-103X.

”Diagnosis and protection of corroding steel in concrete”,
Franz Pruckner, 20002:140, ISBN 82-471-5555-4, ISSN 0809-103X.

“Tensile and Compressive Creep of Young Concrete: Testing and Modelling”,
Dawood Atrushi, 2003:17, ISBN 82-471-5565-6, ISSN 0809-103X.

“Rheology of Particle Suspensions. Fresh Concrete, Mortar and Cement Paste with Various Types of Lignosulfonates”,
Jon Elvar Wallevik, 2003:18, ISBN 82-471-5566-4, ISSN 0809-103X.

“Oblique Loading of Aluminium Crash Components”,
Aase Reyes, 2003:15, ISBN 82-471-5562-1, ISSN 0809-103X.

“Utilization of Ethiopian Natural Pozzolans”,
Surafel Ketema Desta, 2003:26, ISSN 82-471-5574-5, ISSN:0809-103X.

“Behaviour and strength prediction of reinforced concrete structures with discontinuity regions”, Helge Brå, 2004:11, ISBN 82-471-6222-9, ISSN 1503-8181.

“High-strength steel plates subjected to projectile impact. An experimental and numerical study”, Sumita Dey, 2004:38, ISBN 82-471-6282-2 (printed version), ISBN 82-471-6281-4 (electronic version), ISSN 1503-8181.

“Alkali-reactive and inert fillers in concrete. Rheology of fresh mixtures and expansive reactions.”
Bård M. Pedersen, 2004:92, ISBN 82-471-6401-9 (printed version), ISBN 82-471-6400-0 (electronic version), ISSN 1503-8181.

“On the Shear Capacity of Steel Girders with Large Web Openings”.
Nils Christian Hagen, 2005:9 ISBN 82-471-6878-2 (printed version), ISBN 82-471-6877-4 (electronic version), ISSN 1503-8181.

”Behaviour of aluminium extrusions subjected to axial loading”.
Østen Jensen, 2005:7, ISBN 82-471-6873-1 (printed version), ISBN 82-471-6872-3 (electronic version), ISSN 1503-8181.

”Thermal Aspects of corrosion of Steel in Concrete”.
Jan-Magnus Østvik, 2005:5, ISBN 82-471-6869-3 (printed version), ISBN 82-471-6868 (electronic version), ISSN 1503-8181.

”Mechanical and adaptive behaviour of bone in relation to hip replacement.” A study of bone remodelling and bone grafting.
Sébastien Muller, 2005:34, ISBN 82-471-6933-9 (printed version), ISBN 82-471-6932-0 (electronic version), ISSN 1503-8181.

“Analysis of geometrical nonlinearities with applications to timber structures”.
Lars Wollebæk, 2005:74, ISBN 82-471-7050-5 (printed version), ISBN 82-471-7019-1 (electronic version), ISSN 1503-8181.

“Pedestrian induced lateral vibrations of slender footbridges”,
Anders Rönnquist, 2005:102, ISBN 82-471-7082-5 (printed version), ISBN 82-471-7081-7 (electronic version), ISSN 1503-8181.

“Initial Strength Development of Fly Ash and Limestone Blended Cements at Various Temperatures Predicted by Ultrasonic Pulse Velocity”,
Tom Ivar Fredvik, 2005:112, ISBN 82-471-7105-8 (printed version), ISBN 82-471-7103-1 (electronic version), ISSN 1503-8181.

“Behaviour and modelling of thin-walled cast components”,
Cato Dørum, 2005:128, ISBN 82-471-7140-6 (printed version), ISBN 82-471-7139-2 (electronic version), ISSN 1503-8181.

“Behaviour and modelling of selfpiercing riveted connections”,
Raffaele Porcaro, 2005:165, ISBN 82-471-7219-4 (printed version), ISBN 82-471-7218-6 (electronic version), ISSN 1503-8181.

”Behaviour and Modelling og Aluminium Plates subjected to Compressive Load”,
Lars Rønning, 2005:154, ISBN 82-471-7169-1 (printed version), ISBN 82-471-7195-3 (electronic version), ISSN 1503-8181.

”Bumper beam-longitudinal system subjected to offset impact loading”,
Satyanarayana Kokkula, 2005:193, ISBN 82-471-7280-1 (printed version), ISBN 82-471-7279-8 (electronic version), ISSN 1503-8181.

“Control of Chloride Penetration into Concrete Structures at Early Age”,
Guofei Liu, 2006:46, ISBN 82-471-7838-9 (printed version), ISBN 82-471-7837-0 (electronic version), ISSN 1503-8181.

“Modelling of Welded Thin-Walled Aluminium Structures”,
Ting Wang, 2006:78, ISBN 82-471-7907-5 (printed version), ISBN 82-471-7906-7 (electronic version), ISSN 1503-8181.

”Time-variant reliability of dynamic systems by importance sampling and probabilistic analysis of ice loads”,
Anna Ivanova Olsen, 2006:139, ISBN 82-471-8041-3 (printed version), ISBN 82-471-8040-5 (electronic version), ISSN 1503-8181.

“Fatigue life prediction of an aluminium alloy automotive component using finite element analysis of surface topography”.
Sigmund Kyrre Ås, 2006:25, ISBN 82-471-7791-9 (printed version), ISBN 82-471-7791-9 (electronic version), ISSN 1503-8181.

”Constitutive models of elastoplasticity and fracture for aluminium alloys under strain path change”,
Dasharatha Achani, 2006:76, ISBN 82-471-7903-2 (printed version), ISBN 82-471-7902-4 (electronic version), ISSN 1503-8181.

“Simulations of 2D dynamic brittle fracture by the Element-free Galerkin method and linear fracture mechanics”,
Tommy Karlsson, 2006:125, ISBN 82-471-8011-1 (printed version), ISBN 82-471-8010-3 (electronic version), ISSN 1503-8181.

“Penetration and Perforation of Granite Targets by Hard Projectiles”,
Chong Chiang Seah, 2006:188, ISBN 82-471-8150-9 (printed version), ISBN 82-471-8149-5 (electronic version), ISSN 1503-8181.

"Deformations, strain capacity and cracking of concrete in plastic and early hardening phases",
Tor Arne Hammer, 2007:234, ISBN 978-82-471-5191-4 (printed version), ISBN 978-82-471-5207-2 (electronic version), ISSN 1503-8181.

"Crashworthiness of dual-phase high-strength steel: Material and Component behaviour", Venkatapathi Tarigopula, 2007:230, ISBN 82-471-5076-4 (printed version), ISBN 82-471-5093-1 (electronic version), ISSN 1503-8181.

"Fibre reinforcement in load carrying concrete structures",
Åse Lyslo Døssland, 2008:50, ISBN 978-82-471-6910-0 (printed version), ISBN 978-82-471-6924-7 (electronic version), ISSN 1503-8181.

"Low-velocity penetration of aluminium plates",
Frode Grytten, 2008:46, ISBN 978-82-471-6826-4 (printed version), ISBN 978-82-471-6843-1 (electronic version), ISSN 1503-8181.

"Robustness studies of structures subjected to large deformations",
Ørjan Fyllingen, 2008:24, ISBN 978-82-471-6339-9 (printed version), ISBN 978-82-471-6342-9 (electronic version), ISSN 1503-8181.

"Constitutive modelling of morsellised bone",
Knut Birger Lunde, 2008:92, ISBN 978-82-471-7829-4 (printed version), ISBN 978-82-471-7832-4 (electronic version), ISSN 1503-8181.

"Experimental Investigations of Wind Loading on a Suspension Bridge Girder",
Bjørn Isaksen, 2008:131, ISBN 978-82-471-8656-5 (printed version), ISBN 978-82-471-8673-2 (electronic version), ISSN 1503-8181.

"Cracking Risk of Concrete Structures in The Hardening Phase",
Guomin Ji, 2008:198, ISBN 978-82-471-1079-9 (printed version), ISBN 978-82-471-1080-5 (electronic version), ISSN 1503-8181.

"Modelling and numerical analysis of the porcine and human mitral apparatus",
Victorien Emile Prot, 2008:249, ISBN 978-82-471-1192-5 (printed version), ISBN 978-82-471-1193-2 (electronic version), ISSN 1503-8181.

"Strength analysis of net structures",
Heidi Moe, 2009:48, ISBN 978-82-471-1468-1 (printed version), ISBN 978-82-471-1469-8 (electronic version), ISSN1503-8181.

"Numerical analysis of ductile fracture in surface cracked shells",
Espen Berg, 2009:80, ISBN 978-82-471-1537-4 (printed version), ISBN 978-82-471-1538-1 (electronic version), ISSN 1503-8181.

"Subject specific finite element analysis of bone – for evaluation of the healing of a leg lengthening and evaluation of femoral stem design",
Sune Hansborg Pettersen, 2009:99, ISBN 978-82-471-1579-4 (printed version), ISBN 978-82-471-1580-0 (electronic version), ISSN 1503-8181.

"Evaluation of fracture parameters for notched multi-layered structures",
Lingyun Shang, 2009:137, ISBN 978-82-471-1662-3 (printed version), ISBN 978-82-471-1663-0 (electronic version), ISSN 1503-8181.

"Modelling of Dynamic Material Behaviour and Fracture of Aluminium Alloys for Structural Applications"
Yan Chen, 2009:69, ISBN 978-82-471-1515-2 (printed version), ISBN 978-82 471-1516-9 (electronic version), ISSN 1503-8181.

"Nanomechanics of polymer and composite particles"
Jianying He 2009:213, ISBN 978-82-471-1828-3 (printed version), ISBN 978-82-471-1829-0 (electronic version), ISSN 1503-8181.

"Mechanical properties of clear wood from Norway spruce"
Kristian Berbom Dahl 2009:250, ISBN 978-82-471-1911-2 (printed version) ISBN 978-82-471-1912-9 (electronic version), ISSN 1503-8181.

"Modeling of the degradation of TiB_2 mechanical properties by residual stresses and liquid Al penetration along grain boundaries"
Micol Pezzotta 2009:254, ISBN 978-82-471-1923-5 (printed version) ISBN 978-82-471-1924-2 (electronic version) ISSN 1503-8181.

"Effect of welding residual stress on fracture"
Xiabo Ren 2010:77, ISBN 978-82-471-2115-3 (printed version) ISBN 978-82-471-2116-0 (electronic version), ISSN 1503-8181.

"Pan-based carbon fiber as anode material in cathodic protection system for concrete structures"
Mahdi Chini 2010:122, ISBN 978-82-471-2210-5 (printed version) ISBN 978-82-471-2213-6 (electronic version), ISSN 1503-8181.

"Structural Behaviour of deteriorated and retrofitted concrete structures"
Irina Vasililjeva Sæther 2010:171, ISBN 978-82-471-2315-7 (printed version) ISBN 978-82-471-2316-4 (electronic version) ISSN 1503-8181.

"Prediction of local snow loads on roofs"
Vivian Meløysund 2010:247, ISBN 978-82-471-2490-1 (printed version) ISBN 978-82-471-2491-8 (electronic version) ISSN 1503-8181.

"Behaviour and modelling of polymers for crash applications"
Virgile Delhaye 2010:251, ISBN 978-82-471-2501-4 (printed version) ISBN 978-82-471-2502-1 (electronic version) ISSN 1503-8181.

"Blended cement with reducted CO_2 emission – Utilizing the Fly Ash-Limestone Synergy",
Klaartje De Weerdt 2011:32, ISBN 978-82-471-2584-7 (printed version) ISBN 978-82-471-2584-4 (electronic version) ISSN 1503-8181.

"Chloride induced reinforcement corrosion in concrete" Concept of critical chloride content – methods and mechanisms.
Ueli Angst 2011:113, ISBN 978-82-471-2769-9 (printed version) ISBN 978-82-471-2763-6 (electronic version) ISSN 1503-8181.

"A thermo-electric-Mechanical study of the carbon anode and contact interface for Energy savings in the production of aluminium".
Dag Herman Andersen 2011:157, ISBN 978-82-471-2859-6 (printed version) ISBN 978-82-471-2860-2 (electronic version) ISSN 1503-8181.

"Structural Capacity of Anchorage Ties in Masonry Veneer Walls Subjected to Earthquake". The implications of Eurocode 8 and Eurocode 6 on a typical Norwegain veneer wall.
Ahmed Mohamed Yousry Hamed 2011:181, ISBN 978-82-471-2911-1 (printed version) ISBN 978-82-471-2912-8 (electronic ver.) ISSN 1503-8181.

"Work-hardening behaviour in age-hardenable Al-Zn-Mg(-Cu) alloys".
Ida Westermann , 2011:247, ISBN 978-82-471-3056-8 (printed ver.) ISBN 978-82-471-3057-5 (electronic ver.) ISSN 1503-8181.

"Behaviour and modelling of selfpiercing riveted connections using aluminium rivets".
Nguyen-Hieu Hoang, 2011:266, ISBN 978-82-471-3097-1 (printed ver.) ISBN 978-82-471-3099-5 (electronic ver.) ISSN 1503-8181.

"Fibre reinforced concrete".
Sindre Sandbakk, 2011:297, ISBN 978-82-471-3167-1 (printed ver.) ISBN 978-82-471-3168-8 (electronic ver) ISSN 1503:8181.

"Dynamic behaviour of cablesupported bridges subjected to strong natural wind".
Ole Andre Øiseth, 2011:315, ISBN 978-82-471-3209-8 (printed ver.) ISBN 978-82-471-3210-4 (electronic ver.) ISSN 1503-8181.

"Constitutive modeling of solargrade silicon materials"
Julien Cochard, 2011:307, ISBN 978-82-471-3189-3 (printed ver). ISBN 978-82-471-3190-9 (electronic ver.) ISSN 1503-8181.

"Constitutive behavior and fracture of shape memory alloys"
Jim Stian Olsen, 2012:57, ISBN 978-82-471-3382-8 (printed ver.) ISBN 978-82-471-3383-5 (electronic ver.) ISSN 1503-8181.

“Field measurements in mechanical testing using close-range photogrammetry and digital image analysis”
Egil Fagerholt, 2012:95, ISBN 978-82-471-3466-5 (printed ver.) ISBN 978-82-471-3467-2 (electronic ver.) ISSN 1503-8181.

“Towards a better under standing of the ultimate behaviour of lightweight aggregate concrete in compression and bending”,
Håvard Nedrelid, 2012:123, ISBN 978-82-471-3527-3 (printed ver.) ISBN 978-82-471-3528-0 (electronic ver.) ISSN 1503-8181.

“Numerical simulations of blood flow in the left side of the heart”
Sigrid Kaarstad Dahl, 2012:135, ISBN 978-82-471-3553-2 (printed ver.) ISBN 978-82-471-3555-6 (electronic ver.) ISSN 1503-8181.

“Moisture induced stresses in glulam”
Vanessa Angst-Nicollier, 2012:139, ISBN 978-82-471-3562-4 (printed ver.) ISBN 978-82-471-3563-1 (electronic ver.) ISSN 1503-8181.

“Biomechanical aspects of distraction osteogensis”
Valentina La Russa, 2012:250, ISBN 978-82-471-3807-6 (printed ver.) ISBN 978-82-471-3808-3 (electronic ver.) ISSN 1503-8181.

“Ductile fracture in dual-phase steel. Theoretical, experimental and numerical study”
Gaute Gruben, 2012:257, ISBN 978-82-471-3822-9 (printed ver.) ISBN 978-82-471-3823-6 (electronic ver.) ISSN 1503-8181.

“Damping in Timber Structures”
Nathalie Labonnote, 2012:263, ISBN 978-82-471-3836-6 (printed ver.) ISBN 978-82-471-3837-3 (electronic ver.) ISSN 1503-8181.

“Biomechanical modeling of fetal veins: The umbilical vein and ductus venosus bifurcation”
Paul Roger Leinan, 2012:299, ISBN 978-82-471-3915-8 (printed ver.) ISBN 978-82-471-3916-5 (electronic ver.) ISSN 1503-8181.

“Large-Deformation behaviour of thermoplastics at various stress states”
Anne Serine Ognedal, 2012:298, ISBN 978-82-471-3913-4 (printed ver.) ISBN 978-82-471-3914-1 (electronic ver.) ISSN 1503-8181.

“Hardening accelerator for fly ash blended cement”
Kien Dinh Hoang, 2012:366, ISBN 978-82-471-4063-5 (printed ver.) ISBN 978-82-471-4064-2 (electronic ver.) ISSN 1503-8181.

“From molecular structure to mechanical properties”
Jianyang Wu, 2013:186, ISBN 978-82-471-4485-5 (printed ver.) ISBN 978-82-471-4486-2 (electronic ver.) ISSN 1503-8181.

"Experimental and numerical study of hybrid concrete structures"
Linn Grepstad Nes, 2013:259, ISBN 978-82-471-4644-6 (printed ver.) ISBN 978-82-471-4645-3 (electronic ver.) ISSN 1503-8181.

"Mechanics of ultra-thin multi crystalline silicon wafers"
Saber Saffar, 2013:199, ISBN 978-82-471-4511-1 (printed ver.) ISBN 978-82-471-4513-5 (electronic ver). ISSN 1503-8181.

"Through process modelling of welded aluminium structures"
Anizahyati Alisibramulisi, 2013:325, ISBN 978-82-471-4788-7 (printed ver.) ISBN 978-82-471-4789-4 (electronic ver.) ISSN 1503-8181.

"Combined blast and fragment loading on steel plates"
Knut Gaarder Rakvåg, 2013:361, ISBN978-82-471-4872-3 (printed ver.) ISBN 978-82-4873-0 (electronic ver.). ISSN 1503-8181.

"Characterization and modelling of the anisotropic behaviour of high-strength aluminium alloy"
Marion Fourmeau, 2014:37, ISBN 978-82-326-0008-3 (printed ver.) ISBN 978-82-326-0009-0 (electronic ver.) ISSN 1503-8181.

"Behaviour of threated steel fasteners at elevated deformation rates"
Henning Fransplass, 2014:65, ISBN 978-82-326-0054-0 (printed ver.) ISBN 978-82-326-0055-7 (electronic ver.) ISSN 1503-8181.

"Sedimentation and Bleeding"
Ya Peng, 2014:89, ISBN 978-82-326-0102-8 (printed ver.) ISBN 978-82-326-0103-5 (electric ver.) ISSN 1503-8181.

"Impact against X65 offshore pipelines"
Martin Kristoffersen, 2014:362, ISBN 978-82-326-0636-8 (printed ver.) ISBN 978-82-326-0637-5 (electronic ver.) ISSN 1503-8181.

"Formability of aluminium alloy subjected to prestrain by rolling"
Dmitry Vysochinskiy, 2014:363,, ISBN 978-82-326-0638-2 (printed ver.) ISBN 978-82-326-0639-9 (electronic ver.) ISSN 1503-8181.

"Experimental and numerical study of Yielding, Work-Hardening and anisotropy in textured AA6xxx alloys using crystal plasticity models"
Mikhail Khadyko, 2015:28, ISBN 978-82-326-0724-2 (printed ver.) ISBN 978-82-326-0725-9 (electronic ver.) ISSN 1503-8181.

"Behaviour and Modelling of AA6xxx Aluminium Alloys Under a Wide Range of Temperatures and Strain Rates"
Vincent Vilamosa, 2015:63, ISBN 978-82-326-0786-0 (printed ver.) ISBN 978-82-326-0787-7 (electronic ver.) ISSN 1503-8181.

“A Probabilistic Approach in Failure Modelling of Aluminium High Pressure Die-Castings”
Octavian Knoll, 2015:137, ISBN 978-82-326-0930-7 (printed ver.) ISBN 978-82-326-0931-4 (electronic ver.) ISSN 1503-8181.

“Ice Abrasion on Marine Concrete Structures”
Egil Møen, 2015:189, ISBN 978-82-326-1034-1 (printed ver.) ISBN 978-82-326-1035-8 (electronic ver.) ISSN 1503-8181.

“Fibre Orientation in Steel-Fibre-Reinforced Concrete”
Giedrius Zirgulis, 2015:229, ISBN 978-82-326-1114-0 (printed ver.) ISBN 978-82-326-1115-7 (electronic ver.) ISSN 1503-8181.

“Effect of spatial variation and possible interference of localised corrosion on the residual capacity of a reinforced concrete beam”
Mohammad Mahdi Kioumarsi, 2015:282, ISBN 978-82-326-1220-8 (printed ver.) ISBN 978-82-1221-5 (electronic ver.) ISSN 1503-8181.

“The role of concrete resistivity in chloride-induced macro-cell corrosion”
Karla Horbostel, 2015:324, ISBN 978-82-326-1304-5 (printed ver.) ISBN 978-82-326-1305-2 (electonic ver.) ISSN 1503-8181.

“Flowable fibre-reinforced concrete for structural applications”
Elena Vidal Sarmiento, 2015-335, ISBN 978-82-326-1324-3 (printed ver.) ISBN 978-82-326-1325-0 (electronic ver.) ISSN 1503-8181.

“Development of chushed sand for concrete production with microproportioning”
Rolands Cepuritis, 2016:19, ISBN 978-82-326-1382-3 (printed ver.) ISBN 978-82-326-1383-0 (electronic ver.) ISSN 1503-8181.

“Withdrawal properties of threaded rods embedded in glued-laminated timer elements”
Haris Stamatopoulos, 2016:48, ISBN 978-82-326-1436-3 (printed ver.) ISBN 978-82-326-1437-0 (electronic ver.) ISSN 1503-8181.

“An Experimental and numerical study of thermoplastics at large deformation”
Marius Andersen, 2016:191, ISBN 978-82-326-1720-3 (printed ver.) ISBN 978-82-326-1721-0 (electronic ver.) ISSN 1503-8181.

“Modeling and Simulation of Ballistic Impact”
Jens Kristian Holmen, 2016:240, ISBN 978-82-326-1818-7 (printed ver). ISBN 978-82-326-1819-4 (electronic ver.) ISSN 1503-8181.

“Early age crack assessment of concrete structures”
Anja B. Estensen Klausen, 2016:256, ISBN 978-82-326-1850-7 (printed ver). ISBN 978-82-326-1851-4 (electronic ver.) ISSN 1503-8181.

“Uncertainty quantification and sensitivity analysis for cardiovascular models”
Vinzenz Gregor Eck, 2016:234, ISBN 978-82-326-1806-4 (printed ver.) ISBN 978-82-326-1807-1 (electronic ver.) ISSN 1503-8181.

“Dynamic behaviour of existing and new railway catenary systems under Norwegain conditions”
Petter Røe Nåvik, 2016:298, ISBN 978-82-326-1935-1 (printed ver.) ISBN 978-82-326-1934-4 (electronic ver.) ISSN 1503-8181.